

ELECTROEXCITATION OF THE GIANT RESONANCE OF ^{17}O

A

THESIS

Submitted to

THE FACULTY OF GRADUATE STUDIES

in Partial Fulfilment of the Requirements

for the Degree of

MASTER OF SCIENCE

in

THE DEPARTMENT OF PHYSICS

UNIVERSITY OF SASKATCHEWAN

by

Blaine Edgar Norum

Saskatoon, Saskatchewan

August, 1975



The author claims copyright. Use shall not be made of the material contained herein without proper acknowledgment, as indicated on the following page.

755398

001000682841

The author has agreed that the Library, University of Saskatchewan, may make this thesis freely available for inspection. Moreover, the author has agreed that permission for extensive copying of this thesis for scholarly purposes may be granted by the professor or professors who supervised the thesis work recorded herein or, in their absence, by the Head of the Department or the Dean of the College in which the thesis work was done. It is understood that due recognition will be given to the author of this thesis and to the University of Saskatchewan in any use of the material in this thesis. Copying or publication or any other use of this thesis for financial gain without approval by the University of Saskatchewan and the author's written permission is prohibited.

Requests for permission to copy or to make other use of material in this thesis in whole or in part should be addressed to:

Head of the Department of Physics
University of Saskatchewan
SASKATOON, Canada
S7N 0W0

ABSTRACT

The 11 to 30 MeV excitation region of ^{17}O has been investigated by means of inelastic electron scattering, with special emphasis placed on the giant resonance. The scattering angle employed was 75.1° , and the incident energies were 64.9, 83.3, 101.3, 113.6, and 124.0 MeV. These conditions correspond to momentum transfers in the range 0.33 to 0.77 fm^{-1} .

The data reveal a broad resonance centred at 22 - 23 MeV excitation, with strength extending down to 10 - 12 MeV excitation. Some fine structure is observed which correlates well with the positions of previously observed levels. A particle-hole model with harmonic oscillator wavefunctions and Kuo-Brown residual interaction is found to predict the strength distribution and q-dependence of the giant resonance form factor very well. However, a scale factor of 1.85 is required to achieve agreement in magnitude. A fit to the Helm model prediction for a C1 transition yields reasonable values for the skin thickness and transition radius parameters. No clear evidence is found for isospin splitting of the giant resonance. The particle-hole model predicts only a slight degree of splitting in the transverse (E1) component of the form factor, and none at all in the longitudinal (C1) component.

A smaller structure between 17.5 and 19.6 MeV excitation is reported for the first time. The Helm model for a C2 transition using parameters determined by the fit to the giant resonance form factor is found to predict the form factor for this structure extremely well.

Levels at 16.5 and 19.6 MeV excitation are also reported for the first time. The former is found to have a natural width of about 300 keV, while the latter appears to be considerably narrower.

ACKNOWLEDGEMENTS

The author wishes to thank Dr. L. Katz, former Director of the Saskatchewan Accelerator Laboratory, for providing the facilities for this work.

Special thanks are due to Dr. J. C. Bergstrom who was the supervisor of this project. The use of his computer codes for radiative corrections and radiation tail calculations is also gratefully acknowledged.

The author acknowledges his deep indebtedness to Dr. E. Tomusiak who oversaw the theoretical calculations.

The author would like to thank Drs. H. Caplan and D. Skopik for overseeing the final preparation of this thesis.

The author thanks the members of the Electron Scattering Group for their assistance during the collecting and analysis of the data. Specifically, he would like to thank Drs. J.C. Kim and R. Yen for their help in explaining the operation of the Oak Ridge-Rochester Shell Model code, and Dr. R. Hicks for the use of his computer programs.

The author would also like to thank the technical staff for their cooperation during the data taking.

The author is grateful to Dr. P. Paul for providing him with the Kuo-Brown interaction matrix elements which were used in the calculations.

The author would like to express his appreciation to Mr. H. Purdie for his skillful draughting of the diagrams contained in the thesis.

Finally, the author wishes to acknowledge the financial support of the National Research Council.

TABLE OF CONTENTS

| | Page |
|-------------|---|
| CHAPTER I | INTRODUCTION 1 |
| CHAPTER II | ELECTRON SCATTERING |
| II.1 | Introduction 4 |
| II.2 | Kinematics 5 |
| II.3 | Electron Scattering Cross-Section (First Born Approximation) 7 |
| II.4 | Radiative Corrections |
| II.4.1 | Introduction 12 |
| II.4.2 | Radiation Tail Correction 15 |
| II.4.3 | Radiative Correction 17 |
| CHAPTER III | EXPERIMENT AND DATA REDUCTION |
| III.1 | Experimental Facility 22 |
| III.2 | Data Reduction |
| III.2.1 | Introduction 26 |
| III.2.2 | Hardware Corrections 27 |
| III.2.3 | Sorting 28 |
| III.2.4 | Elastic Peak Analysis 28 |
| III.2.5 | Giant Resonance Region Analysis . 29 |
| III.2.6 | Inelastic (Discrete Levels) Region Analysis 34 |
| CHAPTER IV | NUCLEAR THEORY |

TABLE OF CONTENTS (Continued)

| | Page |
|------------|--|
| IV.1 | Introduction 36 |
| IV.2 | Electron Scattering in the Particle-Hole Model |
| IV.2.1 | Particle-Hole Model 39 |
| IV.2.2 | Calculation of Excited-State Wavefunctions 45 |
| IV.2.3 | Calculation of Form Factors 47 |
| IV.2.4 | Application to ^{17}O 49 |
| CHAPTER V | RESULTS AND CONCLUSIONS |
| V.1 | Giant Resonance Region |
| V.1.1 | Experimental Results 52 |
| V.1.2 | Comparison to Theory 59 |
| V.2 | Inelastic (Discrete Levels) Region 74 |
| V.3 | Conclusions 74 |
| APPENDIX A | TARGET-IN BACKGROUND |
| A.1 | Introduction 78 |
| A.2 | Elastic Peak Background 79 |
| A.3 | Inelastic Region Background 82 |
| APPENDIX B | QUASI-ELASTIC SCATTERING |
| B.1 | De Forest Theory 85 |

TABLE OF CONTENTS (Continued)

| | Page |
|--|------|
| APPENDIX C BOEKER-BRINK INTERACTION MATRIX ELEMENTS | 89 |
| APPENDIX D SINGLE-PARTICLE MATRIX ELEMENTS | 97 |
| APPENDIX E HELM MODEL | 101 |
| BIBLIOGRAPHY | 103 |

LIST OF TABLES

| | Page |
|-----------|---|
| Table 3.1 | Experimental Conditions 26 |
| Table 3.2 | Radiation Tail and Target-In Background Scale Factors 30 |
| Table 4.1 | Neutron Single-Particle Energies 50 |
| Table 4.2 | Parameters Used in Boeker-Brink Interaction 50 |
| Table 5.1 | Experimental and Theoretical Giant Resonance Form Factors 69 |
| Table 5.2 | Inelastic levels Between 11.5 and 17.5 MeV 76 |
| Table A.1 | Multiple Scattering Cross-Section Ratios (Filled cell/Empty cell) 83 |

LIST OF FIGURES

| | | Page |
|------------|---|------|
| Figure 2.1 | Electron Scattering Kinematics | 6 |
| Figure 2.2 | First-Order Feynman Diagram for Electron Scattering | 8 |
| Figure 2.3 | Typical Electron Scattering Spectrum | 13 |
| Figure 2.4 | Definition of Peak Limits | 14 |
| Figure 2.5 | Radiative Correction and Photon Emission Diagrams for Electron Scattering | 19 |
| Figure 3.1 | Floor Plan for the Saskatchewan Accelerator Laboratory | 23 |
| Figure 3.2 | Gas Target Cell | 24 |
| Figure 3.3 | Experimental Arrangement for Electron Scattering . . | 25 |
| Figure 3.4 | Sample ^{17}O spectrum before tail subtraction and radiative corrections | 31 |
| Figure 3.5 | Similar to 3.4, but after tail subtraction | 32 |
| Figure 3.6 | Radiative Stripping | 33 |
| Figure 5.1 | Differential form factor (squared) for the electroexcitation of ^{17}O ($E_i = 64.9$ MeV, $\theta = 75.1^\circ$). | 53 |
| Figure 5.2 | Similar to 5.1, but $E_i = 83.3$ MeV | 54 |
| Figure 5.3 | Similar to 5.1, but $E_i = 101.3$ MeV | 55 |
| Figure 5.4 | Similar to 5.1, but $E_i = 113.6$ MeV | 56 |
| Figure 5.5 | Similar to 5.1, but $E_i = 124.0$ MeV | 57 |
| Figure 5.6 | Low lying energy levels of ^{16}O | 60 |
| Figure 5.7 | Low lying energy levels of ^{17}O | 61 |

LIST OF FIGURES (Continued)

| | | Page |
|-------------|--|------|
| Figure 5.7 | Low lying energy levels of ^{17}O | 61 |
| Figure 5.8 | Theoretical differential form factor (squared) for the electroexcitation of ^{17}O calculated using the particle-hole model with Boeker-Brink residual interaction ($E_i = 124.0$ MeV). | 63 |
| Figure 5.9 | Similar to 5.8, but residual interaction is Kuo-Brown, $E_i = 64.9$ MeV | 64 |
| Figure 5.10 | Similar to 5.9, but $E_i = 83.3$ MeV | 65 |
| Figure 5.11 | Similar to 5.9, but $E_i = 101.3$ MeV | 66 |
| Figure 5.12 | Similar to 5.9, but $E_i = 113.6$ MeV | 67 |
| Figure 5.13 | Similar to 5.9, but $E_i = 124.0$ MeV | 68 |
| Figure 5.14 | Experimental and theoretical form factors (squared) for the electroexcitation of the giant resonance of ^{17}O | 71 |
| Figure 5.15 | Theoretical differential transverse form factor (squared) for the electroexcitation of ^{17}O | 72 |
| Figure 5.16 | Experimental and theoretical form factors (squared) for the electroexcitation of the 17.5-19.6 MeV structure in ^{17}O ($E_i = 113.6$ MeV) | 73 |
| Figure 5.17 | Differential form factor (squared) for the electroex- citation of the 11.5-17.5 MeV region in ^{17}O | 75 |
| Figure A.1 | Multiple Scattering from Target Cell | 78 |

LIST OF FIGURES (Continued)

| | Page |
|------------|--|
| Figure A.2 | Coordinate System for Multiple Scattering |
| | Description 80 |
| Figure A.3 | Feynman Diagrams for Processes Contributing to |
| | Hard Bremsstrahlung Background 84 |

CHAPTER I

INTRODUCTION

Historically, the first measurements to reveal the existence of the nuclear giant resonance were those of Baldwin and Klaiber (48). They measured the $^{12}\text{C}(\gamma, n)^{11}\text{C}$ and $^{63}\text{Cu}(\gamma, n)^{63}\text{Cu}$ cross-sections as a function of energy and observed broad (a few MeV) resonances at excitation energies of about 20 to 25 MeV in the spectra of both nuclei. Their work was followed up by Hirzel and Waffler (48) who verified the existence of the broad resonances. The sum rule calculations of Levinger and Bethe (50) indicated with some certainty that the observed resonances were due primarily to the electric dipole absorption of γ -rays, hence the name 'Giant Dipole Resonance'.

Considerable effort has been expended in the study of the giant resonance and other excited states of ^{16}O . The abundance of data on this nucleus makes ^{17}O a good nucleus in which to study the perturbation caused by the addition of a single nucleon to a self-conjugate system. For instance, several low-lying states in ^{17}O have been adequately explained in terms of a weak-coupling model in which the extra neutron is weakly coupled to an ^{16}O core.

The scarcity (0.037% natural abundance) and resultant high cost have discouraged those types of studies of this nucleus in which ^{17}O is used as a target. The only electron scattering experiment on ^{17}O that has been reported is that of R. Singhal (70) who measured the radius of ^{17}O to be almost identical to that of ^{16}O . Studies of several other reactions such as $^{16}\text{O}(n, \gamma)^{17}\text{O}$, $^{16}\text{O}(n, n)^{16}\text{O}$, and $^{13}\text{C}(\alpha, \alpha)^{13}\text{C}$ have established with some completeness the energy level spectrum below 10 MeV excitation.

The experimental studies of the ^{17}O giant resonance region have involved

capture or stripping reactions. Johnson et al (61) observed resonances in the $^{14}\text{C}(^3\text{He},n)^{16}\text{O}$ cross-sections corresponding to levels at 20.5 and 21.1 MeV in ^{17}O . Using the same reaction Honsaker et al (70) observed a state at 22.1 MeV. Resonances were observed in the reaction $^{14}\text{C}(^3\text{He},^4\text{He})^{13}\text{C}$ corresponding to levels at 21.7 and 22.1 MeV in ^{17}O and in the reaction $^{14}\text{C}(^3\text{He},^3\text{He})^{14}\text{C}$ corresponding to a level at 23.0 MeV (Keyser et al, 70). The state at 20.5 MeV has also been observed via the reaction $^{16}\text{O}(n,n)^{16}\text{O}$ (Boreli 70).

In the simple shell model the ^{16}O ground state corresponds to a completely filled $0p$ -shell. The accuracy of this description is attested to by the large nucleon binding energy in ^{16}O . In the same model the ^{17}O ground state corresponds to an ^{16}O core plus a valence neutron. ^{17}O thus forms a good testing ground for this model.

Several theoretical studies of the low-lying states in ^{17}O have been made (Zuker et al 68, Quesne 65, Hsieh et al 75), but very little work has been done involving the region of the giant resonance. D. Albert (69) computed electron scattering form factors and photoabsorption cross-sections using the particle-hole model for the ^{17}O giant resonance. However, in his work the excited states were constructed using only the $0d-1s$ shell while ignoring the contributions from excitations of the valence neutron to the $0f-1p$ shell. It has been shown by Harekah et al (74) that an adequate description of the ^{17}F giant resonance requires the inclusion of the $0f-1p$ shell. Similar considerations are expected to apply to ^{17}O since ^{17}F and ^{17}O are mirror nuclei.

In the work to be described here the cross-sections and form factors for the electroexcitation of ^{17}O were measured in the region from 11 to 30 MeV excitation for momentum transfers in the range 0.33 to 0.72 fm^{-1} . The giant dipole resonance was observed to peak at about 23 MeV excitation. The observed

form factors were compared to a particle-hole calculation in which the ^{17}O ground state was approximated by a closed Op shell plus a neutron in the $\text{Od}_{5/2}$ shell. Excited states were formed by promoting a Op shell nucleon to the Od-1s shell, and by promoting the $\text{Od}_{5/2}$ neutron to the Of-1p shell.

Evidence for quadrupole strength in the 17.5 to 19.6 MeV region was observed. The shape of the observed structure indicates the presence of several closely spaced levels.

Sharp peaks were observed in the region 11.5 to 17.5 MeV excitation. Two new levels (16.5, 17.1 MeV) were observed and the existence of several previously observed states was confirmed.

Chapter II contains a discussion of electron scattering. Equations and formulae relevant to this experiment are presented.

Chapter III contains a description of the experiment. The various corrections applied to the data are also discussed.

Chapter IV contains an outline of the particle-hole model as it applies to ^{17}O . The computer codes used in the calculations are discussed.

Chapter V contains a presentation of both the experimental and theoretical results.

CHAPTER II

ELECTRON SCATTERINGII.1 Introduction

High energy electron scattering has been used to study nuclear structure since the early 1950's when R. Hofstadter performed the first experiments at Stanford University. There are two main reasons why its use has gained wide acceptance.

First, the interaction between the electron and nucleus is electromagnetic. Since this interaction is well understood, it is possible to distill from the experimental results those features which are due to nuclear structure. This is especially convenient in the First Born approximation which will be discussed in Section 3. Furthermore, the comparative weakness of the electromagnetic interaction means that the presence of the electron causes only a small perturbation to the nuclear Hamiltonian. It is thus possible to make an investigation 'without disturbing the evidence'.

Second, it is possible to vary the three-momentum transfer \vec{q} while holding ω , the electron energy loss, fixed. This is to be contrasted with the case of photoabsorption, where $|\vec{q}|$ always equals the nuclear excitation (neglecting recoil). This flexibility makes it possible to measure the q -dependence of the transition matrix elements of a state and hence provide a mapping of the Fourier Transform of the associated transition charge and current densities. One can therefore, in principle at least, determine the spatial distributions of these densities. The kinematics which govern this process are outlined in Section 2.

Electron scattering is not without its drawbacks. When an electron is

scattered by a nucleus it undergoes an acceleration and consequently radiates, losing energy in the process. Therefore, knowledge of the initial and final electron energies does not uniquely determine the energy to which the nucleus was excited by that electron since the energy lost by the electron is divided among the nucleus and one or more undetected photons. This necessitates important corrections to the data which will be discussed in Section 4.

The topics in quantum electrodynamics and nuclear theory which contribute to the derivation of the electron scattering formalism have been the subjects of many books and articles. The quantum electrodynamics have been discussed extensively by such authors as Bjorken and Drell (64) and Schweber (61). The nuclear physics aspect has been discussed by many authors including Willey (63) and Lewis and Walecka (64). The general topic of electron scattering has been thoroughly dealt with in review articles by Hofstadter (56), Bishop (65), de Forest and Walecka (66), and Barber (67). An excellent survey of both the experimental and theoretical developments in electron scattering prior to 1962 is provided in a collection of reprinted articles edited by Hofstadter (63). The Proceedings of the M.I.T. Summer Study (67) gives not only the theoretical background, but also discussions of the technical aspects of electron scattering. Finally, the two-volume treatise by H. Uberall (71) is a particularly useful compendium of the subject.

II.2 Kinematics

In the laboratory frame, where the target nucleus is initially at rest, the electron scattering process can be represented graphically by Figure 2.1.

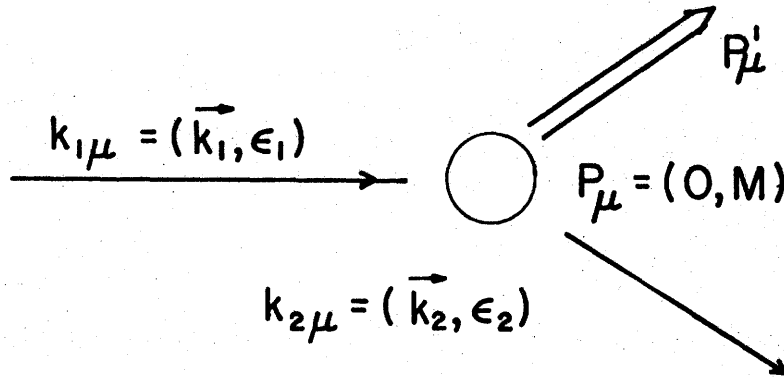


Figure 2.1 Electron Scattering Kinematics

Before proceeding to evaluate kinematic relations, it is necessary to establish some terminology. First, here and in the remainder of this thesis natural units ($\hbar = c = 1$) will be used. m_e will refer to the mass of the electron, m_N to the mass of a nucleon, and M to the mass of a nucleus. The three- and four-momentum transfers will be defined by:

$$\vec{q} = \vec{k}_2 - \vec{k}_1, \quad (2.1)$$

$$q = |\vec{q}|, \quad (2.2)$$

$$q_\mu = k_{2\mu} - k_{1\mu}. \quad (2.3)$$

The metric of the four-vector space is:

$$g_{\mu\nu} = \begin{pmatrix} 1 & 0 & 0 & 0 \\ 0 & 1 & 0 & 0 \\ 0 & 0 & 1 & 0 \\ 0 & 0 & 0 & -1 \end{pmatrix}. \quad (2.4)$$

The application of four-momentum conservation to the electron scattering process yields:

$$k_{1\mu} + P_\mu = k_{2\mu} + P'_\mu. \quad (2.5)$$

Solving Equation 2.5 under the assumption that m_e is negligibly small yields:

$$q_{\perp} q^{\mu} = q_{\perp}^2 = -4\epsilon_1 \epsilon_2 \sin^2(\theta/2) \quad (2.6)$$

and

$$\epsilon_2 = \frac{\epsilon_1 - \omega(1+\omega/2M)}{1 + (2\epsilon_1/M)\sin^2(\theta/2)} \quad (2.7)$$

where ω is the energy to which the nucleus is excited, and

$$\vec{q} \cdot \vec{q} = q^2 = \{-q_{\perp}^2/2M + \omega + \omega^2/2M\}^2 - q_{\perp}^2. \quad (2.8)$$

II.3 Electron Scattering Cross-Section (First Born Approximation)

The calculation of cross-sections for processes involving high energy electrons incident upon target nuclei has been greatly simplified by the work of R. P. Feynman (49). In his formulation the scattering matrix is expanded in a perturbation series, each term of which is represented by a diagram. The contribution of each diagram can be calculated by applying a set of simple rules.

The first of these rules states that the contribution of an n^{th} order diagram is proportional to $(z\alpha)^n$, where z is the nuclear charge and α is the fine structure constant ($\approx 1/137$). Since the electron scattering cross-section is proportional to the square of the scattering matrix, the contribution of the second-order diagrams to the cross-section differ from that of the first order diagram by a factor of about $(z\alpha)^2$.

In the First Born approximation only the first order diagram is retained. This approximation is valid when $z\alpha \ll 1$, since the largest of the neglected contributions to the cross-section is smaller than that retained by a factor $(z\alpha)^2$. In the case of ^{17}O , $(z\alpha)^2 \approx 0.0035 \ll 1$, so the First Born approxima-

tion may be employed safely. The development to follow is, therefore, to be understood in the context of this approximation.

The first-order Feynman diagram for a general electron-nucleus interaction (Fig. 2.2) shows an incident electron exchanging a single virtual ($q_\mu q^\mu \neq 0$) photon with a target nucleus. Two characteristics of the First Born approximation are thereby revealed. Firstly, the interaction consists of the exchange of a single photon. Secondly, both before and after this single scattering event the electron is moving in free space. Therefore, the initial and final wavefunctions will be plane waves.

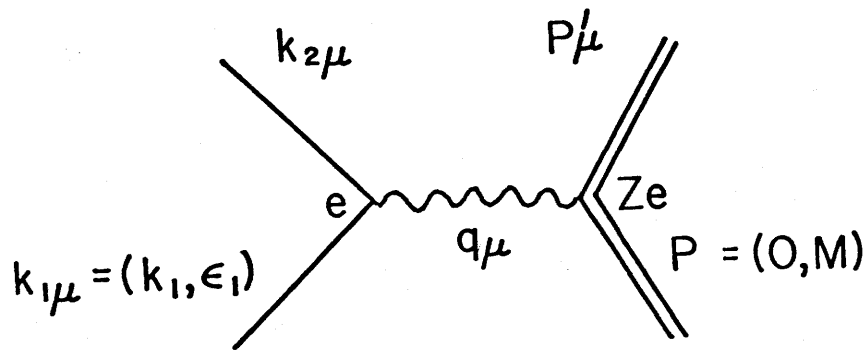


Figure 2.2 First-Order Feynman Diagram for Electron Scattering

Following the notation of de Forest and Walecka (66) application of the Feynman Rules to this diagram yields for the one photon exchange cross-section:

$$d\sigma = 2z^2 \alpha^2 \frac{dk_2}{2\epsilon_2} \frac{1}{q_\mu^4} W_{\mu\nu} \Pi^{\mu\nu} \frac{1}{[(k_1 \cdot P)^2 - m_e^2 M^2]^2} \quad (2.9)$$

where $\Pi_{\mu\nu} = -\frac{1}{2} \text{Tr} [\gamma_\mu (m - i\gamma \cdot k_1) \gamma_\nu (m - i\gamma \cdot k_2)]$

and $W_{\mu\nu} = \frac{(2\pi)^3}{z^2} V \bar{\sum}_1 \sum_1 \delta^{(4)}(P - P' - q) \langle P' | \hat{J}_\nu(0) | P' \rangle \langle P' | \hat{J}_\mu(0) | P \rangle (E).$

γ_μ is a Dirac γ -matrix, $\hat{J}_\mu(0)$ is the electromagnetic four-current operator at the space-time point $x_\mu = 0$, $|P\rangle$ and $|P'\rangle$ denote the initial and final nuclear states respectively, V is the normalization volume, E is the initial target energy and $\bar{\Sigma}$ ($\underline{\Sigma}$) indicates an average (sum) over initial (final) nuclear states.

It should be noted here that the electron dynamics are contained in $\eta_{\mu\nu}$, while the nuclear charges and currents appear in $W_{\mu\nu}$. One can therefore see that the separation of the electron dynamics from the unknown nuclear properties (which was previously cited as a major advantage of electron scattering) is particularly straightforward in this approximation.

Since the nuclear charge and current distributions are the unknown quantities being sought, the form of $W_{\mu\nu}$ is not specified. However, the restrictions of Lorentz invariance, parity conservation, and charge conservation restrict the number of forms which $W_{\mu\nu}$ can assume to (Bjorken 60, von Gehlen 60, Gourdin 61):

$$W_{\mu\nu} = W_1(q_\mu^2, q \cdot P) \left[\delta_{\mu\nu} - \frac{q_\mu q_\nu}{q_\mu^2} \right] + \frac{W_2(q_\mu^2, q \cdot P)}{M^2} \left[\frac{P_\mu}{q_\mu^2} - \frac{P \cdot q}{q_\mu^2} \frac{q_\mu}{q_\mu} \right] \left[\frac{P_\nu}{q_\mu^2} - \frac{P \cdot q}{q_\mu^2} \frac{q_\nu}{q_\mu} \right] \quad (2.10)$$

where $W_{1,2}$ are scalar functions. It has been shown (Drell and Walecka 64) that any process connected to the nucleus through a single photon exchange will depend upon the same functions $W_{1,2}(q_\mu^2, q \cdot P)$.

The electron scattering cross-section (in the lab frame, neglecting electron mass) now becomes:

$$\frac{d^2\sigma}{d\Omega_2 d\epsilon_2} = z^2 \left[\frac{4\alpha^2 \epsilon_2^2 \cos^2(\theta/2)}{q_\mu^4} \right] \left[W_2(q_\mu^2, q \cdot P) + 2W_1(q_\mu^2, q \cdot P) \tan^2(\theta/2) \right]. \quad (2.11)$$

Equation 2.11 can be simplified if one defines the Mott Cross-section (Mott 29):

$$\sigma_M = \frac{4\alpha^2 \epsilon_2^2 \cos^2(\theta/2)}{q_\perp^4} \quad (2.12)$$

which describes the scattering of ultra-relativistic fermions from a spinless point charge. It differs from the classical scattering cross-section of Rutherford only by the factor $\cos^2(\theta/2)$ which is the high energy approximation to the relativistic spin factor $[1 - v^2/c^2 \sin^2(\theta/2)]$.

Equation 2.11 can be specialized to the case of the electroexcitation of discrete nuclear states. Since both the initial and final nuclear states are of definite parity and angular momentum, it is convenient to decompose the nuclear charge and current distributions into multipole series. The details of this decomposition can be found in de Forest and Walecka (66). After much algebra the electron scattering cross-section becomes:

$$\frac{d\sigma}{d\Omega} = z^2 \sigma_M F^2(q^2, \theta) \eta \quad , \quad (2.13)$$

where F^2 is the nuclear structure factor and η is the kinematic recoil correction factor. The nuclear physics has, therefore, been isolated in the nuclear structure factor. It can be expanded in terms of charge and current multipoles to yield:

$$F^2(q^2, \theta) = \frac{4\pi}{z^2 (2J_i + 1)} \left[\frac{q_\perp^4}{q^4} \sum_{J=0}^{\infty} |\langle J_f || \hat{M}_J^C(q) || J_i \rangle|^2 + \left\{ \frac{1}{2} \frac{q_\perp^2}{q^2} + \tan^2(\theta/2) \right\} \sum_{J=1}^{\infty} \{ |\langle J_f || \hat{T}_J^{EL}(q) || J_i \rangle|^2 + |\langle J_f || \hat{T}_J^{Mag}(q) || J_i \rangle|^2 \} \right] \quad , \quad (2.14)$$

where J_i (J_f) is the initial (final) nuclear spin.

$$\hat{M}_{JM}^C(q) = \int d^3x j_J(qx) Y_J^M(\hat{x}) \hat{\rho}_N(\vec{x}) \quad (2.15)$$

is the Coulomb multipole operator, while j_J is a Spherical Bessel Function, Y_J^M is a Spherical Harmonic, and $\hat{\rho}_N$ is the nuclear charge density operator. It is to be noted that if one defines the \hat{z} -direction as being the direction of \vec{q} , then \hat{M}_{JM}^C is the $(J,M)^{th}$ term in the Fourier transform of ρ_N .

$$\begin{aligned} \hat{T}_{JM}^{El}(q) = \frac{1}{q} \int d^3x [\{ \vec{\nabla} \times j_J(qx) \vec{Y}_{JJ1}^M(\hat{x}) \} \cdot \hat{j}_N(\vec{x}) \\ + q^2 j_J(qx) \vec{Y}_{JJ1}^M(\hat{x}) \cdot \hat{\mu}_N(\hat{x})] \end{aligned} \quad (2.16)$$

is the transverse electric operator, while \hat{j}_N is the nuclear convection current density operator, $\hat{\mu}_N$ is the magnetization density operator, and \vec{Y}_{JJ1}^M is a Vector Spherical Harmonic.

$$\begin{aligned} \hat{T}_{JM}^{Mag}(q) = \int d^3x [j_J(qx) \vec{Y}_{JJ1}^M(\hat{x}) \cdot \hat{j}_N(\hat{x}) \\ + \{ \vec{\nabla} \times j_J(qx) \vec{Y}_{JJ1}^M(\hat{x}) \} \cdot \hat{\mu}_N(\hat{x})] \end{aligned} \quad (2.17)$$

is the transverse magnetic operator. The quantities $\langle || \hat{O} || \rangle$ are called the reduced transition matrix elements of the enclosed operator (\hat{O}).

One can therefore define the longitudinal and transverse form factors (F_L and F_T , respectively) by:

$$F^2(q, \theta) = |F_L(q)|^2 + \left\{ \frac{|q_{\perp}^2|}{2q^2} + \tan^2(\theta/2) \right\} |F_T(q)|^2. \quad (2.18)$$

It is significant that these form factors are functions of q alone and that the angular dependence of $F^2(q, \theta)$ is confined to the $\tan^2(\theta/2)$ factor. It is thus possible to determine separately the two form factors simply by making two or

more measurements of $F^2(q, \theta)$ at the same value of q , but at different values of θ .

The factor η which appears in Equation 2.13 is defined by:

$$\eta = [1 + (2\epsilon_1/M) \sin^2(\theta/2)]^{-1} \quad (2.19)$$

It serves to correct the scattering cross-section to take into account the recoil of the nucleus.

The generalization of Equations 2.14 and 2.18 to the case of scattering to the continuum or to a broad resonance is immediate. The cross-section becomes a differential cross-section with respect to the final electron energy as well as the angle, and the form factors become differential form factors with respect to final electron energy also.

II.4 Radiative Corrections

II.4.1 Introduction

Before proceeding to discuss the radiative corrections it would be appropriate to outline some of the basic features of the data and to introduce some pertinent terminology. A typical electron scattering spectrum is shown in Figure 2.3. It can be divided into four main sections; elastic peak, inelastic region (discrete levels), giant resonance region, and continuum. The elastic peak corresponds to electrons which scatter without exciting the nucleus. The inelastic region contains electrons which excite the nucleus to a well-defined energy. The giant resonance region is made up of electrons which excite the nucleus to a quasi-bound resonance. The continuum consists of electrons which excite one or more nucleons from the nucleus into continuum (unbound) final states.

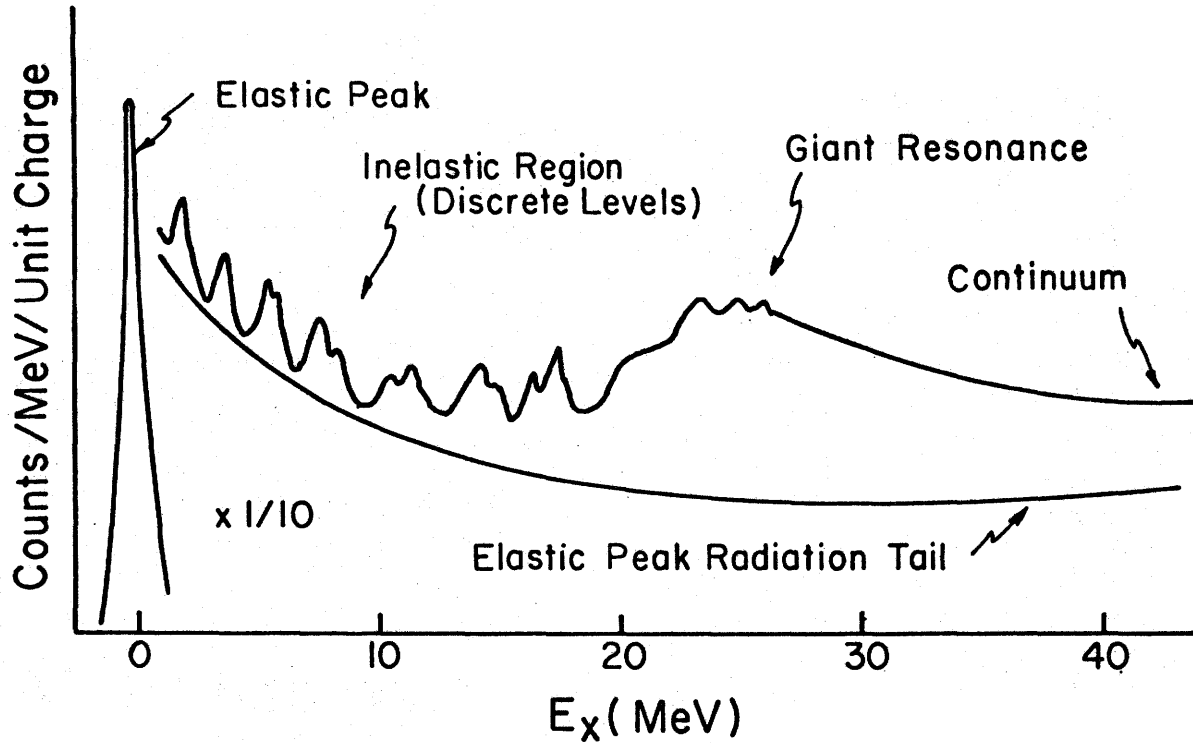


Figure 2.3 Typical Electron Scattering Spectrum

The immediate purpose of an electron scattering experiment is to measure the cross-section for one or more of the aforementioned processes, where the cross-section is defined as:

the number of scattered electrons per unit solid angle, per unit energy, per target nucleus, per unit incident beam flux.

If one assumes that this quantity varies little over the energy range ΔE and solid angle $\Delta\Omega$ then this definition becomes:

$$\left(\frac{d^2\sigma}{d\Omega d\epsilon_2} \right)_{\text{OBS}} = \frac{n_e}{\Delta\epsilon_2 \Delta\Omega N (I/e)}, \quad (2.20)$$

where N is the number of target nuclei per unit area, e is the electron charge, I is the incident charge, $\Delta\epsilon_2$ is the detector resolution, $\Delta\Omega$ is the spectrometer acceptance angle, and n_e is the number of scattered electrons detected.

It is to be noted that the observed cross-section is always a differential one with respect to final electron energy. For the excitation of a narrow level the cross-section is proportional to the area of a peak. However, the bounds of the peak are not well defined since electrons which excited this level also lost varying amounts of energy due to radiation. They therefore fall farther down in the spectrum forming a so-called 'radiation tail'. This tail constitutes an undesirable background which must be removed. One therefore defines the experimental area of a peak by integrating the number of detected electrons in an arbitrary energy range $\epsilon_0 - \Delta E$ to ϵ' (see Fig. 2.4).

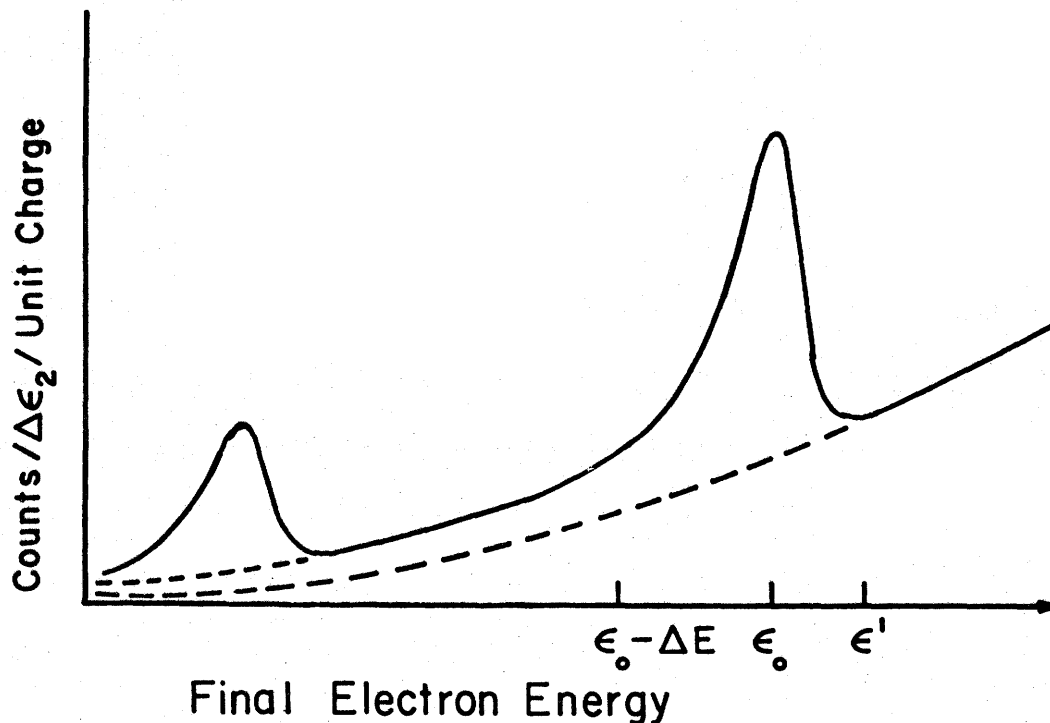


Figure 2.4 Definition of Peak Limits

The above problems are not confined to the case of discrete peaks. Even in regions where the spectrum is continuous (i.e., giant resonance region) the number of electrons detected in the energy interval (ϵ , $\epsilon+\Delta E$) is not an accurate measure of the cross-section for the excitation of the nucleus to that energy. The same processes which complicate the discrete peak interpretation also contribute here.

In order to interpret the data in the context of the First Born approximation one must determine what the observed cross-sections would be in the absence of radiative processes. Therefore, one must subtract from the experimental cross-section those counts which are due to the radiation tails of other peaks, and add to it those counts which were lost because electrons were degraded in energy and fell further down the spectrum.

The former correction, called the 'radiation tail correction', is discussed in Section 4.2, while the latter, called the 'radiative correction', is discussed in Section 4.3.

II.4.2 Radiation Tail Correction

Three processes contribute significantly to the radiation tail. They are the emission of high energy Bremsstrahlung, small angle Bremsstrahlung, and energy loss due to ionization. The largest single contribution to the tail comes from electrons which have been degraded in energy due to the emission of high energy or hard photons. This process has been discussed by many authors such as Tsai (64), Maximon and Isabelle (64), and Nguyen Ngoc and Perez y Jorba (64, 65). The details of the calculation are extremely tedious, as is the resulting cross-section $(d^2\sigma / d\Omega d\epsilon_2)_{HB}$.

Most of the hard photons are emitted roughly parallel to the path of either the incident or the scattered electron. This fact is the basis of the

peaking approximation. In this approximation one obtains for the hard Bremsstrahlung cross-section (Nguyen Ngoc et al 64):

$$\frac{d^2\sigma}{d\Omega d\epsilon_2} = \frac{\alpha}{\pi\kappa} \left[\frac{2\epsilon_1}{m_e} \sin(\theta/2) \right] - \frac{1}{2} \left[\left\{ 1 + \frac{\epsilon_2^2}{(\epsilon_1 - \omega)^2} \right\} \frac{d\sigma(\epsilon_1, \epsilon_1 - \omega)}{d\Omega} + \left\{ 1 + \frac{(\epsilon_2 + \omega)^2}{\epsilon_1^2} \right\} \frac{d\sigma(\epsilon_2 + \omega, \epsilon_2)}{d\Omega} \right] \quad (2.21)$$

where ω is the excitation energy of the peak generating the tail, $d\sigma(\epsilon_1, \epsilon_2)/d\Omega$ is the radiationless cross-section for the scattering of an electron with energy ϵ_1 so that the scattered electron has an energy ϵ_2 (i.e., the electroexcitation of a level of energy $\epsilon_1 - \epsilon_2$ - nuclear recoil energy), and

$$\kappa = \epsilon_1 - \epsilon_2 - \omega \quad .$$

The second process by which electrons lose energy and become part of the radiation tail is the emission of small angle Bremsstrahlung. This process was examined by Rossi (52). He found that the probability of an electron of incident energy ϵ_1 emitting a photon of energy E to $E+dE$ is given by:

$$\varphi_{BR}(\epsilon_1, E) = \frac{F(\epsilon_1, \nu)}{x_0 \ln(183 / z^{1/3})} \frac{d\nu}{\nu} \quad (2.22)$$

where $\nu = E / \epsilon_1$,

$$F(\epsilon_1, \nu) = [1 + (1-\nu)^2 - 2(1-\nu)/3] [5.13 - .875\gamma + .125\gamma^2 - \ln(z)/3] ,$$

and $\gamma = 100 (m_e / \epsilon_1) [\nu / (1-\nu)] z^{-1/3}$.

This form of the probability density is not completely general and one should consult either Rossi (52) or Uberall (71) before applying it.

The third way in which an electron can be degraded in energy is by colliding with atomic electrons. The probability that an electron of energy ϵ_1 loses an amount of energy E in such a collision is (Moller 32):

$$\varphi_{\text{ION}}(\epsilon_1, E) = 0.154 \frac{z}{A} \frac{1}{\epsilon_1^2} \left\{ \frac{(1-\nu)^2 + \nu^2}{\nu(1-\nu)} \right\}^2 \quad (2.23)$$

The last two effects are due to the physical size of the target and are hence called 'thick-target' effects. The cross-section for these processes $(d\sigma / d\Omega d\epsilon_2)_{\text{TT}}$ is given in terms of the above probabilities by (Nguyen Ngoc 65):

$$\begin{aligned} \left(\frac{d\sigma}{d\Omega d\epsilon_2} \right)_{\text{TT}} = & \frac{t}{2} [\varphi_{\text{BR}}(\epsilon_1, E) + \varphi_{\text{ION}}(\epsilon_1, E)] \frac{d\sigma(\epsilon_1 - E, \epsilon_2)}{d\Omega} \\ & + \frac{t}{2} [\varphi_{\text{BR}}(\epsilon_2 + E, E) + \varphi_{\text{ION}}(\epsilon_2 + E, E)] \frac{d\sigma(\epsilon_1, \epsilon_2 + E)}{d\Omega} \quad (2.24) \end{aligned}$$

wherein it is assumed that the scattering event took place in the middle of the target. It has been shown (Bergstrom 67) that this is a valid approximation if the target thickness t is small compared to the radiation length.

The total radiation tail can be calculated by combining the thick target and hard Bremsstrahlung cross-sections:

$$\left(\frac{d\sigma}{d\Omega d\epsilon_2} \right)_{\text{Tail}} = \left(\frac{d\sigma}{d\Omega d\epsilon_2} \right)_{\text{BR}} + \left(\frac{d\sigma}{d\Omega d\epsilon_2} \right)_{\text{TT}} \quad (2.25)$$

II.4.3 Radiative Correction

The major contribution here is the Schwinger Correction. It arises from the emission and reabsorption of virtual photons and the emission of low energy

unobserved real photons. Figures 2.5(a-d) show the diagrams which contribute significantly to the first-order radiative corrections to the First Born approximation (Fig. 2.2). These diagrams contain a divergence whereby the differential cross-section exhibits a logarithmic singularity as the energy of the reabsorbed photon approaches zero. However, in a real experiment one always integrates out from zero to a finite cutoff ΔE (Fig. 2.4). It was pointed out by Schwinger (49) that in so doing one is implicitly adding in contributions arising from the emission of a real photon of energy $k < \Delta E$ (Fig. 2.5 e,f). These diagrams contain a divergence which cancels the previous one yielding a finite total result. This latter divergence is called the infrared or Bethe-Heitler divergence.

In view of these effects, the area under an observed spectrum peak (integrated out to some energy cutoff ΔE) must be modified to account for those electrons which would have fallen within the peak in the absence of radiative processes, but which have actually radiated sufficient energy to fall below the peak. The effect of this correction is that the observed cross-section or peak area $(d\sigma / d\Omega)_{\text{OBS}}$, which is now a function of the cutoff (ΔE) must be multiplied by an exponential factor $[e^{\delta_S(\Delta E)}]$ in order to obtain the cross-section for the radiationless process:

$$\left(\frac{d\sigma}{d\Omega} \right)_{\text{NoRad}} = \left(\frac{d\sigma(\Delta E)}{d\Omega} \right)_{\text{OBS}} e^{\delta_S(\Delta E)} . \quad (2.26)$$

The form which δ_S takes when the peak being corrected is the elastic peak is given by Maximon (69):

$$\delta_S(\text{el}) = \frac{2\alpha}{\pi} [\{ 2\pi(\epsilon_1/\Delta E) - 13/12 \} \{ 2\pi(q^2/m_e^2) - 1 \} + 17/36]$$

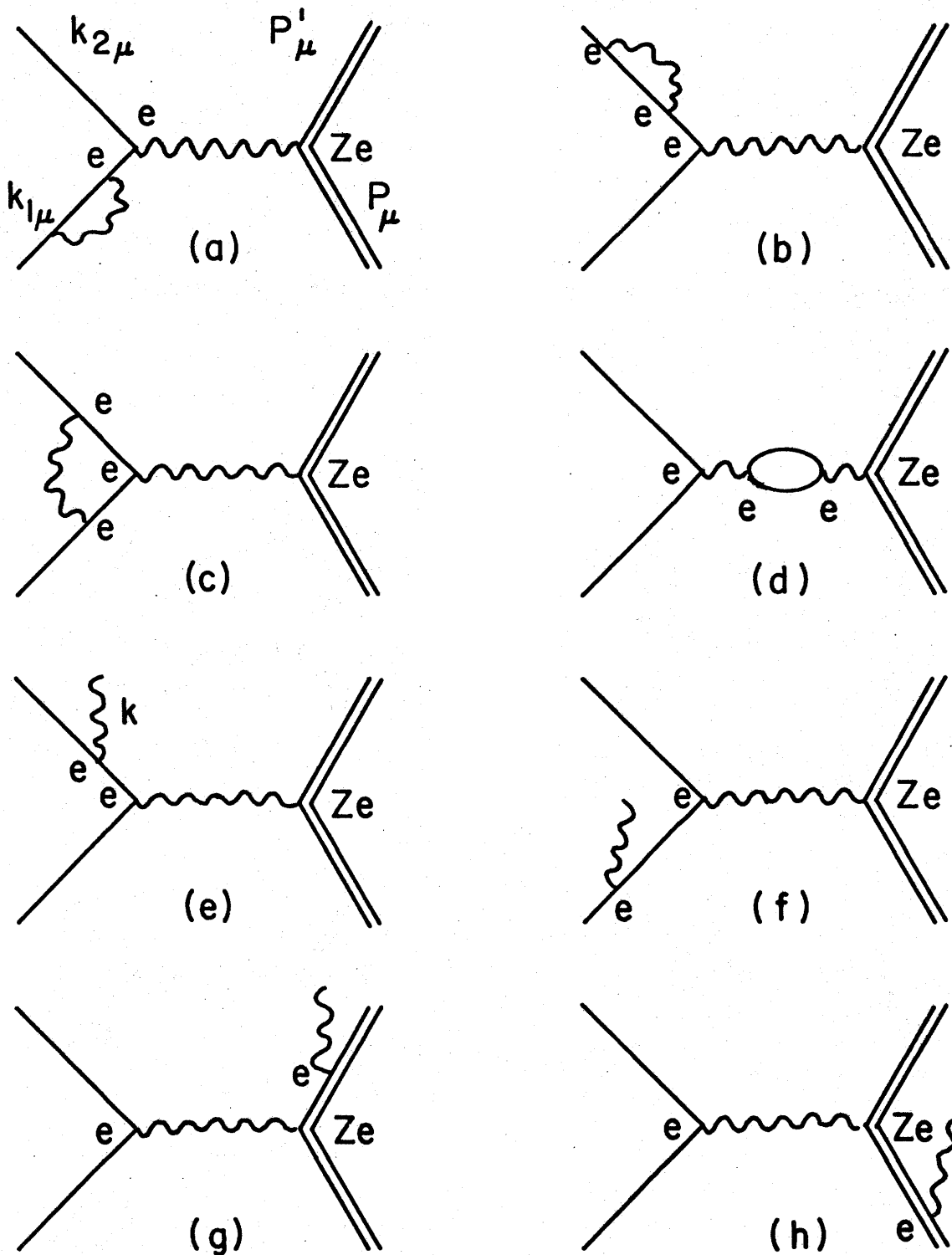


Figure 2.5 Radiative Correction and Photon Emission

Diagrams for Electron Scattering

$$+ \frac{1}{2} \left\{ \pi^2/6 - L_2(\cos^2(\theta/2)) \right\} \left. \right] ; q^2 \gg m_e^2 \quad (2.27)$$

where L_2 is the Spence function defined by:

$$L_2(x) = - \int_0^x \frac{\ln(1-y)}{y} dy \quad .$$

In the case of inelastic scattering to a nuclear level of energy ω , δ_S becomes (Meister 64):

$$\begin{aligned} \delta_S(\text{in}) = (2\alpha/\pi) \left[\left\{ \ln(\sqrt{\epsilon_1 \epsilon_2} / \Delta E) - 13/12 \right\} \left\{ \ln(q^2 / m_e^2) - 1 \right\} + 17/36 \right. \\ \left. + \frac{1}{4} \ln^2(\epsilon_1/\epsilon_2) + \frac{1}{2} \left\{ \pi^2/6 - L_2(\cos^2(\theta/2)) \right\} \right] ; q^2 \gg m_e^2 \end{aligned} \quad (2.28)$$

Another contribution to the radiative correction arises from the recoiling nucleus. The processes which are involved are shown in Figure 2.5 g,h. These processes lead to corrections of the relative order of q/M (Drell 52) and have, therefore, been ignored in this work.

Two other corrections are required due to processes resulting not from the nuclear scattering event under investigation, but from the passage of the electrons through the target matter. They are the straggling or thick-target Bremsstrahlung correction and the Landau correction.

As an electron passes through the target it repeatedly undergoes small deflections which cause soft Bremsstrahlung to be emitted. The probability that an electron of initial energy ϵ_1 passing through a thickness t of matter loses an amount of energy between E and $E+dE$ is given by (Rossi 52, Uberall 71):

$$P_{\text{RAD}}(\epsilon_1, E, t) = \frac{dE}{\epsilon_1} \frac{1}{\Gamma(t/2m_0^2)} \left\{ \ln \left(\frac{\epsilon_1}{\epsilon_1 - E} \right) \right\}^{t/x_0 \ln 2 - 1} \quad (2.29)$$

where Γ is the gamma function and x_0 is the radiation length. This process also introduces a correction factor $[e^{\delta_B(\Delta E)}]$ for which

$$\delta_B(\Delta E) = (t / x_0 \ln 2) \ln (\epsilon_1 / \Delta E) . \quad (2.30)$$

This correction is called the Bremsstrahlung correction.

Electrons passing through matter will also lose energy by colliding with atomic electrons and thereby ionizing the atoms. The probability that an electron of initial energy ϵ_1 passing through a thickness t of matter loses an amount of energy between E and $E+dE$ is given by (Landau 44, Uberall 71):

$$P_{\text{ION}}(\epsilon_1, E, t) dE = \frac{dE}{2\pi i} \int_{\sigma-i\infty}^{\sigma+i\infty} ds e^{sE} \exp[-s\xi(1-C-\ln sE')]] \quad (2.31)$$

where C is the Euler-Mascheroni Constant, and

$$\ln E' \approx \ln [(91/m_e v^2) (1-v^2/c^2)] + v^2/c^2 ,$$

and v is the initial electron speed. This gives rise to a correction factor $[1 + \delta_I(\Delta E)]$ where

$$\delta_I \approx [\lambda \{ 1 - (\ln \lambda + C - 1) / (\lambda + 1) \}]^{-1} \quad (2.32)$$

and $\lambda = (E-E_0) / \xi$, $E_0 = \xi [\ln \xi - \ln E' + 1 - C]$, $\xi = 0.154 t(\text{gm/cm}^2) z/A \text{ MeV}$.

To first order one can obtain the corrected peak area simply by multiplying the observed area by each of the three factors (Nguyen Ngoc 64):

$$\left(\frac{d\sigma}{d\Omega} \right)_{\text{NoRad}} = e^{\delta_S + \delta_B} (1 + \delta_I) \left(\frac{d\sigma(\Delta E)}{d\Omega} \right)_{\text{OBS}} . \quad (2.33)$$

CHAPTER III

EXPERIMENT AND DATA REDUCTIONIII.1 Experimental Facility

The experiment described here was performed using the electron linear accelerator of the Saskatchewan Accelerator Laboratory. A detailed description of this facility is given by Katz et al (67). However, for the sake of completeness a brief description will be given here.

The use of electron scattering as a tool for the study of atomic nuclei requires accurate knowledge of 1) the incident electron momentum, 2) the target properties, and 3) the scattered electron momentum.

The first requirement is satisfied by the beam handling system, a schematic view of which is given in Figure 3.1. The electron beam is delivered from the accelerator through a collimator (COL 1). It is then focused by a quadrupole magnet (Q1) onto horizontal and vertical slits (S1-H, S1-V) which serve to localize it in space. Then the beam is directed through two collimators to a 45° bending magnet (M1). This magnet transforms the energy distribution of the beam into an angular or spatial spread which permits a set of vertical slits (S2-H) to transmit only electrons within a chosen energy range. This energy range can be chosen as narrow as $\pm 0.05\%$ of the beam energy, but for this experiment was set at 0.2% . Magnet M2, a mirror image of M1, then directs the beam into the scattering room. Two quadrupoles (Q2, Q3) further focus the beam so that it appears on the target cell as a small spot.

The electron beam current is continuously monitored using a toroidal charge monitor located between the final focusing quadrupole (Q3) and the scatter chamber. This monitor is regularly calibrated against a Faraday Cup.

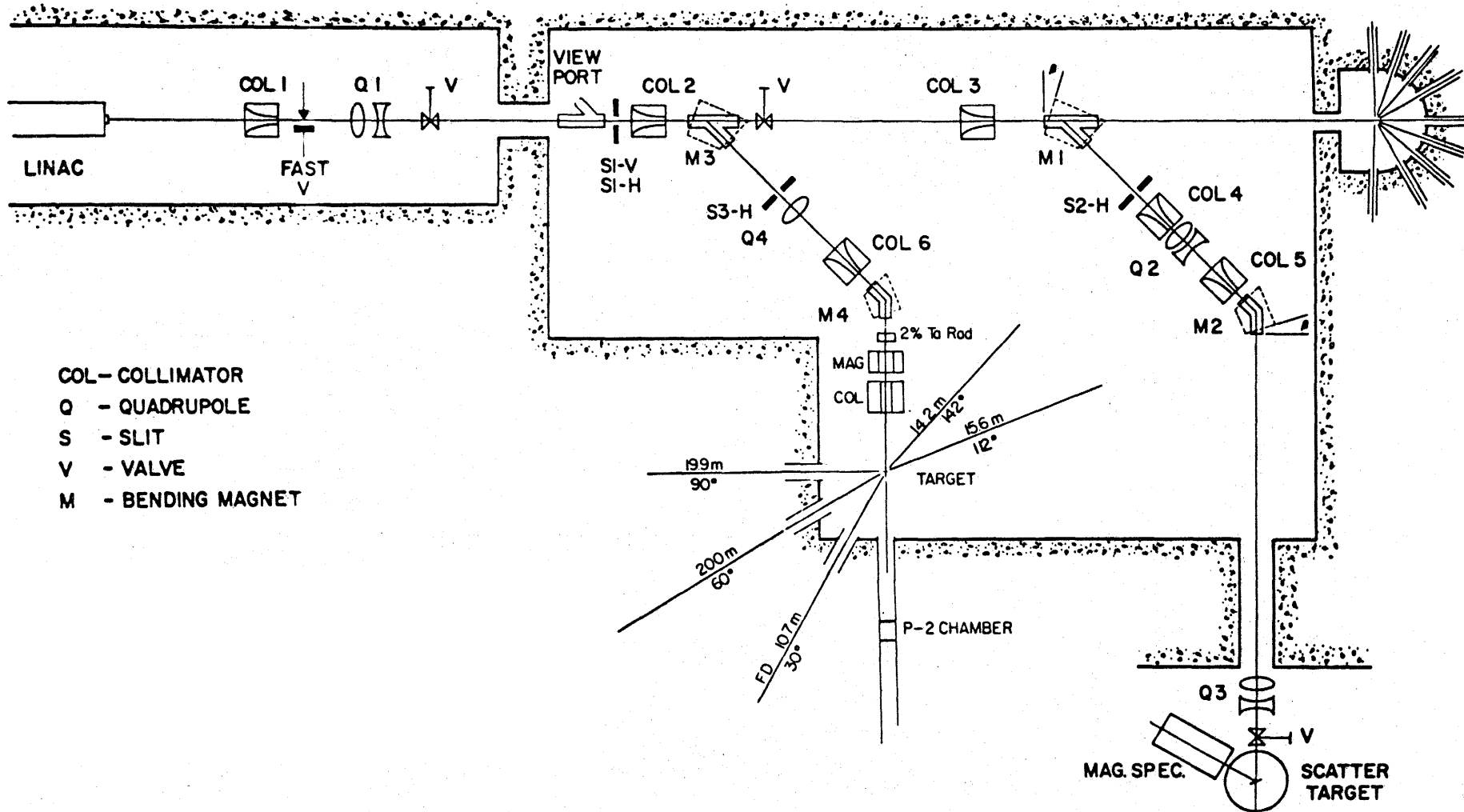


Figure 3.1 Floor Plan for the Saskatchewan Accelerator Laboratory

The target used was 96% isotopically enriched ^{17}O gas in which the main contaminant was ^{16}O . The gas was confined in a cylindrical target cell at approximately 11 atmospheres pressure (Figure 3.2). The cell is 4.5" long and 0.5" in diameter. The entrance window is constructed of 0.001" stainless steel, while the walls are of 0.002" nickel. An empty target cell, similar to the above but with a 0.002" entrance window, was also used as a target to obtain an estimate of the target-in background.

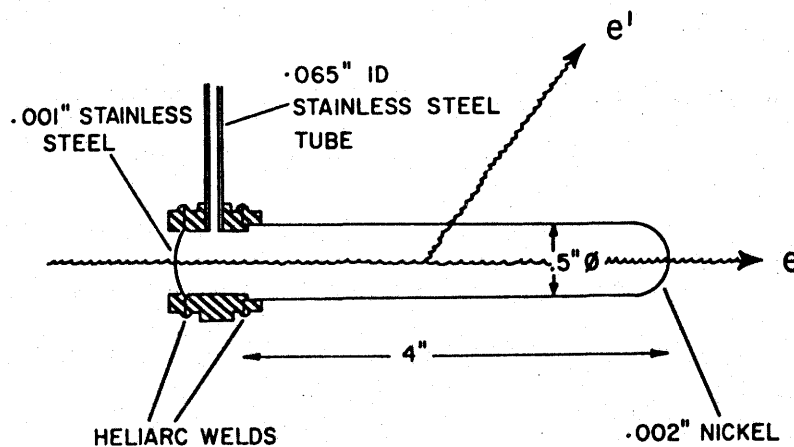


Figure 3.2 Gas Target Cell

The angular spread in the momenta of the electrons to be analyzed is defined by a lead collimator which subtends a solid angle of about 0.0038 steradians at the target centre. The energy spread of the electrons so scattered is converted into a spatial spread by a 127° , 50 cm radius, double-focusing magnetic spectrometer (Figure 3.3). The part of the energy spectrum which reaches the detectors is determined by the magnetic field produced in the spectrometer. This field is continuously monitored by a Rawson Lush Model 921 rotating coil gaussmeter which has an accuracy of about 0.1 gauss, which corresponds to an energy accuracy of about 2 keV. This gaussmeter is the core of the feedback system which maintains

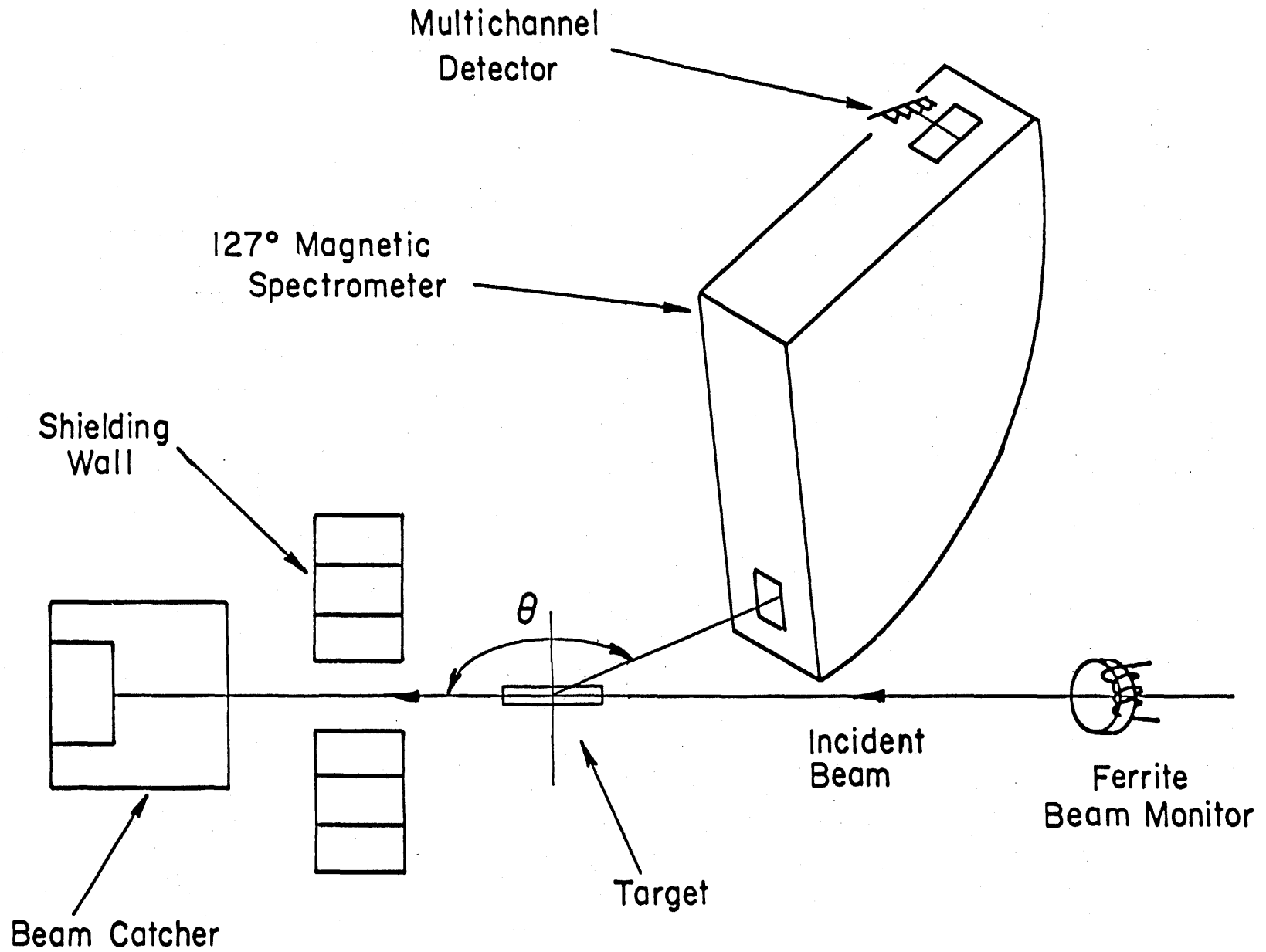


Figure 3.3 Experimental Arrangement for Electron Scattering

the field at its preset strength.

The electrons within the energy range defined by the spectrometer are more finely analyzed and counted using a multi-channel detector system (Auer et al 74). The detector array consists of twenty-four overlapping plastic scintillators arranged so as to define forty-five momentum channels. Background levels are kept low by requiring that the electrons must also be detected by two back-up detectors in order to be counted. The counts registered by these twenty-six detectors are analyzed by a combination of hardware and software programming. By varying the spectrometer field it is possible to obtain a spectrum of the scattered electron counting rate as a function of final electron energy.

III.2 Data Reduction

III.2.1 Introduction

In this work five spectra were measured. The scattering angle in each case was 75.1° . The incident energies and corresponding momentum transfers are listed in Table 3.1.

Table 3.1 Experimental Conditions

| Incident Energy | Momentum Transfer q | |
|--------------------|------------------------|------------------------|
| | Elastic Peak | 25 MeV Excitation |
| 64.9 MeV | 0.400 fm^{-1} | 0.339 fm^{-1} |
| 83.3 | 0.514 | 0.448 |
| 101.3 | 0.625 | 0.557 |
| 113.6 | 0.701 | 0.632 |
| 124.0 | 0.765 | 0.695 |

In order to extract the electroexcitation cross-sections from the data several operations are required. First, corrections to the data are required to account for the physical characteristics of the hardware used. These are discussed in Section III.2.2. Second, the data must be sorted into a useable form. This is discussed in Section III.2.3.

The remaining steps in the reduction depend upon the region of the spectrum being analyzed. The elastic peak analysis is treated in Section III.2.4, while the giant resonance region is discussed in Section III.2.5, and the inelastic (discrete levels) region is discussed in Section III.2.6.

III.2.2 Hardware Corrections

The first correction in this category is the 'dead time' correction. It accounts for the electrons which fail to be counted because of the finite speed of the detection system. That is, if two events occur so close together that the electronics have not recovered from counting the first when the second occurs then the second event will be lost. The magnitude of this correction is determined by having the system measure a given region of a spectrum under different current levels (i.e., different counting rates) and then extrapolating down to the point of zero current.

The second correction accounts for the individual characteristics of the detectors. It is determined by first having each of the forty-five channels measure the same region of a spectrum, and then scaling each channel's output by a factor which makes the scaled outputs of all momentum channels equal. These factors are called the efficiency factors.

A thorough description of the above procedures is given by Auer et al (74).

III.2.3 Sorting

The output from the detector system was sorted into histograms according to final electron energy. The widths of the energy bins in the sorts used in this work depended upon the region of the spectrum involved, and the use to which the histogram was put (i.e., fitting inelastic peaks, fitting tails, etc.).

III.2.4 Elastic Peak Analysis

The purpose of the elastic peak analysis was to obtain a normalization for the inelastic data. Since we were interested in the radiationless (Fig. 2.2) cross-section for single-scattering from ^{17}O two corrections to the elastic peak data were required.

First, the contributions due to scattering from the target cell and to multiple scattering within the cell were subtracted. The method by which this contribution was determined is discussed in Appendix A.

Second, the radiative correction (Section II.4.3) was applied using the computer code CORFAC of J. Bergstrom. The area of each elastic peak was computed for three values of ΔE (Fig. 2.4); 500, 750, 1000 keV. In principle, the corrected area should be independent of ΔE . However, in practice, because of residual background effects some variation is observed. In our case, a variation of about 0.2% was observed over the above range of ΔE . The correction factor corresponding to each ΔE was computed (Equations 2.21, 2.24, 2.26, 2.27) and applied. The three values for the corrected peak area so obtained were averaged to obtain the radiationless cross-section multiplied by a factor determined by kinematics and the physical characteristics of the target.

The calculation of the cross-section and form factor corresponding to each elastic peak was performed using the Rawitscher-Fischer phase-shift code YALERF (Rawitscher et al 61). A harmonic oscillator charge distribution was

used for the ^{17}O ground state with an oscillator parameter of 1.82 fm (Singhal et al 70, Hicks et al 75) corresponding to an r.m.s. radius of 2.70 fm.

The result of this work was a set of five factors, one for each spectrum, by which the counting rates in the inelastic and giant resonance regions could be multiplied to obtain actual cross-sections.

III.2.5 Giant Resonance Region Analysis

The analysis of the giant resonance region of the spectra proceeded in three stages. First, the radiation tail and target-in background were removed. Second, radiative corrections were made. Third, the form factors were extracted by comparing the observed giant resonance cross-sections to the elastic peak cross-sections.

The radiation tail spectra were calculated from Equations 2.21, 2.24, and 2.25 using the computer code ALLRAD of J. Bergstrom. The target-in background spectra were calculated following the method outlined in Appendix A. The sum of these two spectra fell well below the data in all five cases. It was therefore necessary to scale the calculated spectra in order to obtain physically reasonable results.

The procedure adopted for determining the scale factors was to require that the radiation tail and target-in background fit the data at about 11 MeV excitation and that they approach the data in the high excitation limit. Several schemes for scaling the two spectra were tried, each exhibiting the desired behavior. However, they gave widely differing results for the background strength in the giant resonance region. It was therefore further required that the strength left after the background was subtracted fit the de Forest theory (see Appendix B) of quasi-elastic scattering in the high excitation limit. The scaling factors required to achieve this are listed in

Table 3.2.

| Incident Energy | Radiation Tail Scale Factor | Background Scale Factor |
|-----------------|-----------------------------|-------------------------|
| 64.9 MeV | 1.48 | 1.27 |
| 83.3 | 1.50 | 1.20 |
| 101.3 | 1.57 | 1.15 |
| 113.6 | 1.70 | 1.0 |
| 124.0 | 1.70 | 1.0 |

Figure 3.4 shows a sample spectrum with the radiation tail and target-in background that were subtracted. Figure 3.5 shows the corresponding residual spectrum and the de Forest theory prediction to which it was fitted.

The next step was to make radiative corrections to the residual spectra. Since the giant resonance is composed of broad regions of strength, the peak radiative correction method applied in the case of the elastic peak cannot be directly employed. Rather, a procedure called 'stripping' is used.

The procedure of stripping involves treating each energy bin as the peak corresponding to a discrete level. One then applies the peak radiative correction to the first bin. Using the corrected value for the number of counts in that bin one then calculates the radiation tail of that bin and subtracts it from the remaining bins (Figure 3.6). Subsequent bins are treated the same way.

Since the target-in background and the elastic peak radiation tail were fitted to the data at 11 MeV excitation, the radiation tails of the lower-lying levels were assumed to be incorporated into the already subtracted tail. The

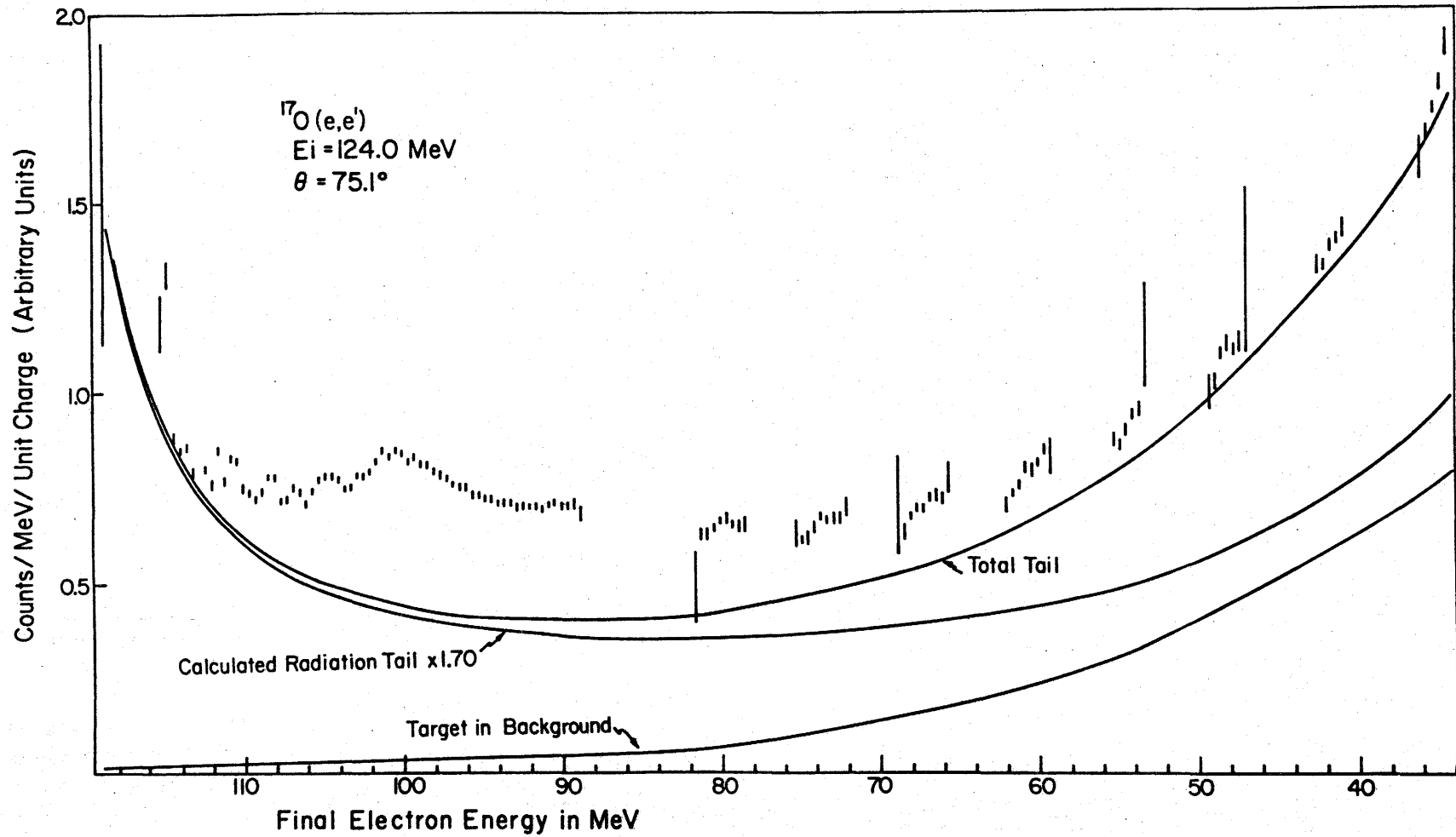


Figure 3.4 Sample ^{17}O spectrum before tail subtraction and radiative corrections. Data points are 400 keV apart. Error bars reflect counting statistics only.

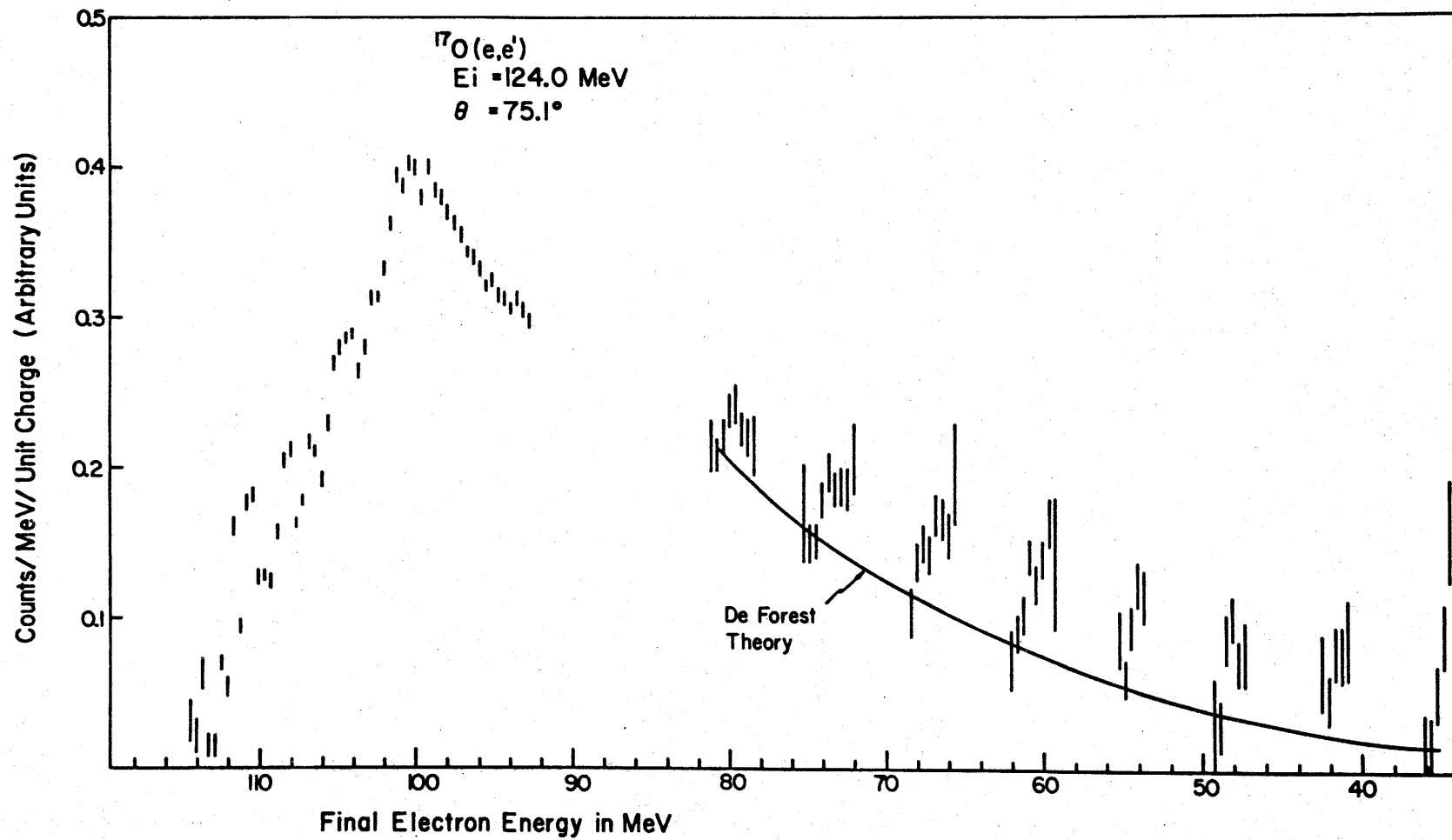


Figure 3.5 Similar to Figure 3.4, but after tail subtraction.

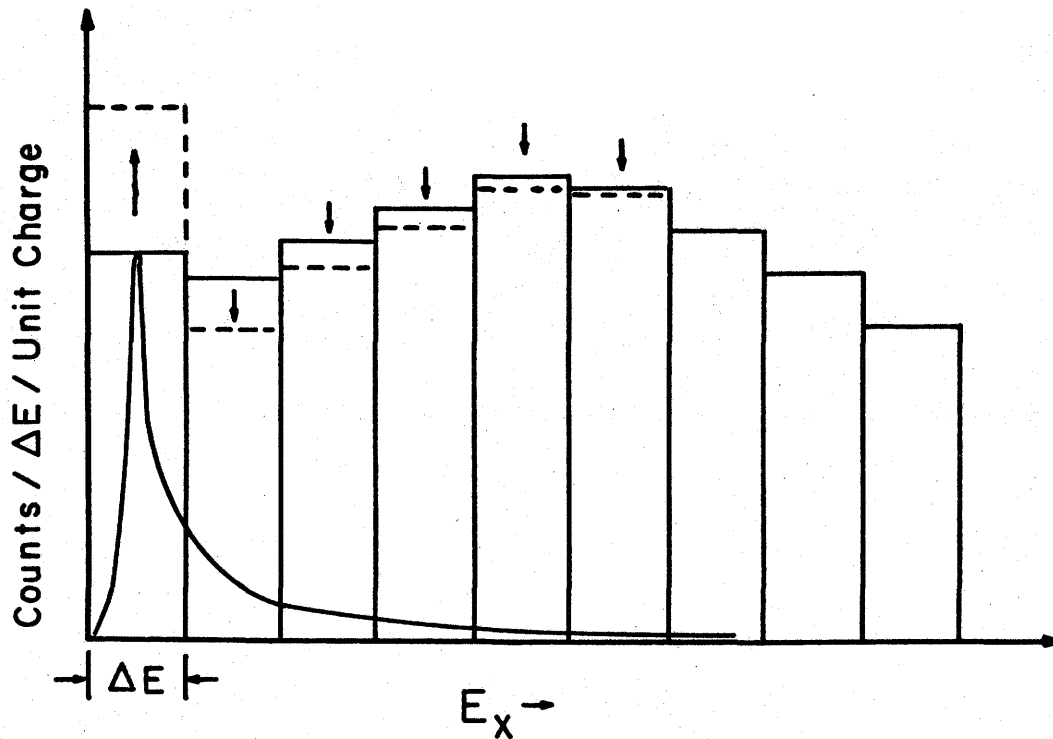


Figure 3.6 Radiative Stripping

stripping procedure was therefore begun at this point. The calculation of the radiation tails was simplified by assuming that the magnitudes of the tails were only significant (*vis à vis* peaks of the same size as the one generating the tail) near the generating peak. In view of this the tails were assumed to be the result of those processes which were corrected for by the radiative correction. It was thus possible to use the inverse of the radiative correction to calculate the radiation tail.

Given that one knows the radiationless cross-section one can calculate the contribution of that peak out to an arbitrary cutoff ΔE simply by multiplying the radiationless cross-section by $e^{-\delta} S^{-\delta} B (1 - \delta_I)$:

$$\frac{d\sigma(\Delta E)}{d\Omega} = \left(\frac{d\sigma}{d\Omega} \right)_{\text{NoRad}} \times e^{-\delta} S^{-\delta} B (1 - \delta_I) \quad (3.1)$$

Obviously, one can calculate the peak's contribution to the spectrum in the final electron energy range E_c to $E_c - \delta E_c$ simply by evaluating Equation 3.1 for E_c and $E_c - \delta E_c$ and subtracting. The dependence of the results of this procedure upon the choice of bin width ΔE was examined by performing the stripping procedure using various values of ΔE between 300 keV and 1 MeV. The observed variation in the results was between 3 (at low excitations) and 5% (high excitations).

It was not possible to unambiguously isolate the broad structure superimposed on the resonance between 17.5 and 19.6 MeV. After the aforementioned procedure had been carried out, an estimate of its area was obtained by simply approximating its lower bound by a straight line, as shown in Figures 5.1 to 5.5.

The results of the above work **are** presented and discussed in Chapter V.

III.2.6 Inelastic (Discrete Levels) Region Analysis

In the region between 11 and 17.5 MeV excitation, the spectra consist of sharp (relative to the broad giant resonance) peaks superimposed on a significant background. The background is made up of 1) the radiation tails of the elastic peak and the many inelastic level peaks lying below 11 MeV excitation, 2) the target-in background, and 3) the broad giant resonance. Unfortunately, it is not possible to calculate these contributions to the degree of accuracy required in order to determine the areas of the superimposed peaks. In view of this, the following procedure was employed. First, the total background was estimated to have the form of a quadratic polynomial. To this were added ten peaks. The five spectra were then fitted using a least-squares method.

The peaks were assumed to have a Breit-Wigner shape:

$$Y(\epsilon) = \frac{(\Gamma/2)^2}{(\Gamma/2)^2 + (\epsilon - \epsilon_0)^2}$$

where Γ is the peak's half-width, and ϵ_0 its centroid. The areas of the peaks were then calculated assuming a peak cutoff ϵ' (Fig. 2.4) of 500 keV and ΔE 's of 500, 750, and 1000 keV. The radiative correction was applied to each of the peaks in much the same manner as it was to the elastic peak. The only difference was that the Schwinger correction coefficient δ_S was calculated using Equation 2.28 as opposed to 2.27.

The results obtained are presented and discussed in Chapter V.

CHAPTER IV

NUCLEAR THEORYIV.1 Introduction

The first attempt to explain the giant resonance was made by M. Goldhaber and E. Teller (Goldhaber 48). They interpreted the resonances as resulting from a process similar to the Restrahl absorption of infrared radiation by ionic crystals. When a photon is incident upon a crystal it tends to drive the crystal into an optical mode (anions against cations) of oscillation. If the photon frequency approaches the resonant frequency for this mode of oscillation of the crystal then the photon can be absorbed and the mode excited. This phenomenon manifests itself as a dip in the transmission curve of the crystal as a function of photon frequency.

With this analogy in mind Goldhaber and Teller proposed three models. In the first model it is assumed that the force required to move a proton from its ground state is proportional to the displacement, and that the constant of proportionality is the same for all nuclei. It was felt that the model would be particularly applicable to nuclei which consist of alpha particle clusters, since in those cases the binding force felt by each nucleon is primarily due to the binding force of the alpha particle. When it failed to predict the observed energy difference between the giant resonances of ${}^4\text{He}$ and ${}^{20}\text{Ne}$, two nuclei which are well described by the alpha-particle model, the model quickly fell into obscurity.

Their second model met with substantially greater success. In it the relative positions of the nucleons on the nuclear surface are assumed fixed, forming a rigid spherical cavity which contains the remaining nuclear matter.

This matter was assumed to comprise two (neutrons, protons) interpenetrable fluids. This model, in which excitations are interpreted as disturbances in the ground state fluid distribution, predicts that the energy of the giant resonance should be proportional to $A^{-1/3}$, where A is the number of nucleons in the nucleus.

This model was extended by Steinwedel, Jensen, and Jensen (50) to accommodate general irrotational flow of the nuclear fluids, as opposed to the linear (neutrons against protons) flow of the original model. Okamoto (58) further generalized it by permitting the nucleus to have a spheroidal shape. This version of the model proved very effective in explaining the observed giant resonances of heavy, deformed nuclei such as holmium (Ambler 65). Danos (61) further extended the model by relaxing the condition that the surface of the nucleus be rigid, permitting low-energy surface vibrations. The model therefore constitutes a union of the Okamoto model and the low-energy collective model of Bohr and Mottelson (53). It proved very successful in describing the observed structure in medium mass nuclei such as ^{75}As (Fielder 65).

Goldhaber's and Teller's third model, the one with which their names are usually associated, treats both the neutrons and protons as rigid but interpenetrable spheres. In the context of this model the giant resonance is explained as an excitation in which the proton and neutron spheres oscillate out of phase. This model predicts that the energy of the giant resonance should vary as $A^{-1/6}$, which is an accurate description of the observed dependence.

The model was extended by Uberall (65) and others to yield the 'Generalized G. T. Model'. They proposed four spheres rather than two; one for the neutrons with spin 'up', one for the neutrons with spin 'down', and two analogous spheres for the protons. This permitted more and varied modes of oscillation, enabling the model to explain some of the structure in the observed

The model has proven very successful, for example, in explaining the structure of the ^{12}C and ^{16}O giant resonances.

The preceding models are all collective in nature, with groups of nucleons acting as units. Obviously, they were unable to explain the observed decay of the giant resonances by single particle emission. Attempts to reconcile the observations and theory based on statistical theory were shown by Hirzel and Waffler (47) to be ineffective, as the observed cross-sections exceeded the calculations by a factor of 10^3 .

The strong indication of single particle behavior prompted the development of the 'particle-hole' or Brown model (Brown 59). While it first appears that the two approaches are completely disjoint, this is not the case. It has been shown (Brink 57, Tomusiak 68) that when applied to closed shell nuclei described by harmonic oscillator wavefunctions, the particle-hole model generates the same transition densities as the Generalized G. T. Model. The general similarity between the predictions of the two models arises from the fact that the introduction of a residual two-body interaction into the Shell model serves to concentrate the transition strength into a small group of states. Furthermore, these states are pushed to higher excitation energies and constitute the Brown model explanation of the giant resonance.

In view of the preceding remarks about the decay of the giant resonance by particle emission, it is significant that the giant resonance in the Brown model is composed of bound states. This does not turn out to be a fatal inconsistency, however, since in the region of interest within the nucleus the bound and unbound wavefunctions are not too different.

The use of this model in the calculation of the electron scattering cross-sections and form factors is discussed in some detail in Section 2.

IV.2 Electron Scattering in the Particle-Hole Model

IV.2.1 Particle-Hole Model

The purpose of this section is to develop a theoretical description of the nucleus for the purpose of calculating the electron-nucleus interaction. This development will proceed within the framework of the nuclear shell model, the basic tenet of which is that the particles of the system move in a central potential.

The shell model was originally conceived to describe the motion of atomic electrons. In that case, the central potential is the Coulomb potential of the nucleus. Furthermore, since the nucleus is much more massive than the electrons its position is essentially fixed and thus serves as a point of reference (i.e., origin of the coordinate system).

Such is not the case in the nuclear model. The forces felt by the nucleons are not generated by some fixed central object, but are due solely to the presence of the other nucleons. In the absence of a fixed central potential, it is not at all transparent that the shell model concept is valid in the nuclear case.

The nuclear shell model is intimately related to the Hartree-Fock (H.F.) many-body theory. The main assumption of the H. F. theory is that the many-particle wavefunction can be approximated by the antisymmetrized product of single-particle wavefunctions:

$$\psi_A(\vec{r}_1, \dots, \vec{r}_A) = \frac{1}{\sqrt{A!}} \begin{vmatrix} \varphi_\alpha(\vec{r}_1) & \varphi_\alpha(\vec{r}_2) & \dots \\ \varphi_\beta(\vec{r}_1) & & \\ \vdots & & \end{vmatrix} \quad (4.1)$$

where A is the number of nucleons, ψ is the many-particle nuclear wavefunction,

the φ 's are the single-particle wavefunctions, and the subscripts denote the full set of quantum numbers characterizing that wavefunction. To obtain the H. F. equations one begins by assuming a trial wavefunction of the form (4.1). One then varies the Hamiltonian with respect to each single-particle wavefunction. Each such variation is then required to equal zero. This procedure yields a set of A coupled equations for the A single-particle wavefunctions. If one assumes that the nuclear Hamiltonian is non-relativistic and that the nucleon-nucleon interaction is a smooth two-body interaction [$V(\vec{r}_1, \vec{r}_2)$], then these equations take the form:

$$\frac{\hbar^2}{2m_N} \nabla^2 \varphi_i(\vec{r}) + \sum_{j \neq i} \int d^3r' V(\vec{r}, \vec{r}') \{ |\varphi_j(\vec{r}')|^2 \varphi_i(\vec{r}) - \varphi_j^*(\vec{r}') \varphi_j(\vec{r}) \varphi_i(\vec{r}') \} = \epsilon_i \varphi_i \quad (4.2)$$

where the ϵ_i 's are called the single particle energies. If one can now assume that the third term is small with respect to the second and can thus be neglected, then one has a Schrodinger equation for the state φ_i in a potential:

$$V^c(\vec{r}) = \sum_{j \neq i} \int d^3r' V(\vec{r}, \vec{r}') |\varphi_j(\vec{r}')|^2 \quad (4.3)$$

determined by the density distribution of the remaining particles. Having established the correspondence between the shell model and the more general H.F. theory one can now use the shell model with some degree of confidence in its validity.

In the model used in this work, V^c is assumed to be a spherically symmetric harmonic oscillator potential. There are three main reasons for this choice. First, any reasonably smooth attractive central potential can be expected to be flat at the origin and then begin to curve upwards as r increases.

This is exactly how the harmonic oscillator potential behaves. Second, the

observed spin and parity of almost every nuclear ground state are correctly predicted by the shell model using a harmonic oscillator central potential. Third, the form of the harmonic oscillator potential makes the solving of the resulting equations relatively easy.

The degeneracies in the oscillator energy levels are assumed to be removed by the action of a spin-orbit force. This model of the nuclear force is, in fact, an over simplification. It is improved by the introduction of a 'residual two-body interaction' [$V^r(\vec{r}_{ij}); \vec{r}_{ij} = \vec{r}_i - \vec{r}_j$]. This constitutes a first-order correction to the assumption that the composite potential generated by the nucleons is a central potential and is consequently treated as a perturbation on the above system. It gives rise to effects such as nucleon pairing in which two nucleons become more tightly bound to one another than they are to the rest of the nucleus.

In configuration space, one can write the Hamiltonian for the system as:

$$H = \sum_i \left[-\frac{\hbar^2}{2m_N} \nabla_i^2 + V^c(\vec{r}_i) \right] + \sum_{i < j} V^r(\vec{r}_{ij}) = H_0 + H_1 \quad (4.4)$$

where the subscript on the gradient operator (∇) indicates that it acts on \vec{r}_i , and $H_0 \varphi_i(\vec{r}) = \epsilon_i \varphi_i(\vec{r})$. The effect of the degeneracy-splitting spin-orbit force is approximately accounted for by adjusting the depth of V^c . Since the central potential was taken to be a harmonic oscillator potential, the single-particle wavefunctions take the form:

$$\varphi_i(\vec{r}) = (1 \ m_1 \ s \ m_s \ | \ j \ m_j) \chi_{m_s}^s \ \chi_{m_\tau}^\tau \ Y_1^{m_j}(\hat{r}) \ R_{nl}(r) \quad (4.5)$$

where i represents the full set of quantum numbers $(l, m_l, s, m_s, j, m_j, \tau, m_\tau, n)$, $\chi_{m_s}^s$ and $\chi_{m_\tau}^\tau$ represent the spin and isospin wavefunctions respectively, and

$$R_{nl}(r) = \sqrt{\frac{2(n-1)!}{b^3 [\Gamma(n+1+\frac{1}{2})]^3}} \left(\frac{r}{b}\right)^l \exp[-(r/b)^2/2] L_{n-1}^{l+\frac{1}{2}}(r^2/b^2),$$

$$L_p^a(z) = \frac{\Gamma(a+p+1)}{\Gamma(p+1)} \frac{e^z [z^{a+p} \exp(-z)]}{z^a},$$

b is the oscillator parameter defined by:

$$b = (1 / \hbar m_N \omega_0)^{\frac{1}{2}},$$

ω_0 is the oscillator frequency, and n is the principle quantum number, (l, m_l) are the orbital angular momentum quantum numbers (magnitude, \hat{z} -projection), $(s=\frac{1}{2}, m_s)$ are the spin quantum numbers, (j, m_j) are the total single-particle angular momentum quantum numbers, and $(\tau=\frac{1}{2}, m_\tau)$ are the isospin quantum numbers. $(\dots | \dots)$ is a Clebsch-Gordon coefficient (Edmonds 58).

The solution to the nuclear problem amounts to the construction of the eigenstates of H. These eigenfunctions will be linear combinations of the Slater determinant wavefunctions (4.1):

$$\psi_A^{\text{eig}}(\vec{r}_1, \dots, \vec{r}_A) = \sum_k C_k \psi_A^k(\vec{r}_1, \dots, \vec{r}_A) \quad (4.6)$$

where the ψ_A^k 's are called the multi-particle states.

Since the eigenfunctions of the harmonic oscillator constitute a basis for an infinite dimensional vector space, the exact eigenfunctions of H are also of infinite dimension. In order to render the problem tractable the Tamm-Dancoff approximation is employed. In this approximation it is assumed that excited states are created by promoting one particle from its ground state to a level approximately $1 \hbar \omega_0$ higher in energy. If the promoted particle comes from a closed shell then the state left vacant is said to contain a hole.

In order to ease the bookkeeping problems which arise during the construc-

tion of these states the problem is cast in the formalism of Second Quantization. Creation and annihilation operators for the single-particle states $\varphi_i(\vec{r})$ are defined as \hat{a}_i^+ and \hat{a}_i respectively. They obey the usual fermion commutation relations:

$$\{ \hat{a}_i^+, \hat{a}_j^+ \} = \{ \hat{a}_i, \hat{a}_j \} = 0 \quad (4.7)$$

$$\text{and} \quad \{ \hat{a}_i^+, \hat{a}_j \} = \delta_{ij} \quad , \quad (4.8)$$

where the subscripts denote a full set of quantum numbers. The vacuum state is defined by:

$$\hat{a}_i | 0 \rangle = 0 \quad (4.9)$$

for every state i .

The Hamiltonian components H_0 and H_1 now take the form:

$$\hat{H}_0 = \sum_{\alpha_1 \alpha_2} \langle \alpha_1 | H_0 | \alpha_2 \rangle \hat{a}_{\alpha_1}^+ \hat{a}_{\alpha_2} \quad (4.10)$$

$$\hat{H}_1 = \frac{1}{4} \sum_{\alpha_1 \alpha_2 \alpha_3 \alpha_4} \langle \alpha_1 \alpha_2 | V^r(\vec{r}_1, \vec{r}_2) | \alpha_3 \alpha_4 \rangle \hat{a}_{\alpha_2}^+ \hat{a}_{\alpha_1}^+ \hat{a}_{\alpha_3} \hat{a}_{\alpha_4} \quad (4.11)$$

Since the states being constructed are states of good angular momentum and isospin it is convenient to express the \hat{a} 's in terms of operators which are tensors in both angular momentum and spin spaces. In the case of states outside a core of filled shells, the \hat{a} 's themselves are the required tensor operators. For states within the core, the creation (annihilation) of a particle is regarded as the annihilation (creation) of a hole. We therefore express the particle creation (annihilation) operator in terms of a hole annihilation (creation) operator:

$$\hat{a}_\alpha^+ = (-1)^{j-m_j + \frac{1}{2} - m_\tau} \hat{b}_\alpha \quad (4.12)$$

$$\hat{a}_\alpha = (-1)^{j-m_j + \frac{1}{2} - m_\tau} \hat{b}_\alpha^+ \quad (4.13)$$

where the \hat{b} 's are tensor operators. Using these we can generate the two distinct types of multi-particle basis states which enter into the ^{17}O calculation, namely the 1 particle - 0 hole (1p-0h) and 2 particle - 1 hole (2p-1h) states:

$$(1p-0h): \hat{A}_\alpha^+ = \hat{a}_\alpha^+ ; \quad \alpha = (J, M_J, T, M_T) \quad (4.14)$$

$$(2p-1h): \hat{B}_\alpha^+ [\{ (j_p, j_v) j \}, j_h; JM_J; \{ (\tau_p, \tau_v) \tau \}, \tau_h; TM_T] =$$

$$\{ 1 - (-1)^{j+\tau} \delta_{pv} \}^{-\frac{1}{2}} \sum_{\substack{m_j \ m_j \ m_j \ m_j \\ m_\tau \ m_\tau \ m_\tau \ m_\tau}} \quad (-1)^{j_h - m_h + \frac{1}{2} - m_{\tau_h}}$$

$$\times (j_p \ m_j \ j_v \ m_j \ | \ j m_j) (\tau_p \ m_\tau \ \tau_v \ m_\tau \ | \ \tau m_\tau)$$

$$\times (j m_j \ j_h \ -m_{j_h} \ | \ JM_J) (\tau m_\tau \ \tau_h \ -m_{\tau_h} \ | \ TM_T) \hat{a}_p^+ \hat{a}_v^+ \hat{b}_h^+ \quad (4.15)$$

where the subscripts (p,v,h) denote the (particle promoted from the core, the valence particle, the hole).

Having formulated both the Hamiltonian and the wavefunctions in compatible and convenient forms, it only remains to diagonalize the Hamiltonian matrix and to compute the transition matrix elements between the ground and excited states.

This model is not without weaknesses. First, the model of the ground state as a closed Op shell plus a valence neutron in the $\text{O}d_{5/2}$ shell is an oversimplification. Zuker et al (68) showed that in order to fit the experimentally observed energy level spectra significant 2p-2h contributions must be

attributed to the ^{16}O ground state, and 3p-2h contributions to the ^{17}O ground state. Second, these same multi-particle - multi-hole contributions are excluded from the excited states as well through the use of the Tamm-Dancoff approximation. Third, one must appeal to experiment to obtain the single-particle energies.

IV.2.2 Calculation of Excited State Wavefunctions

The diagonalization of the Hamiltonian matrix was performed using the Oak Ridge-Rochester Shell Model code of J. B. French et al (69), which was designed to perform large scale spectroscopic computations. It consists of two parts. The first, to be discussed here, performs the diagonalization of the Hamiltonian matrix. The second, which evaluates transition matrix elements between states constructed by the first part, will be discussed later.

The formalism employed in the code is based on the multipole expansion of all operators and wavefunctions in terms of Second Quantized spherical tensors (see preceding section). The use of Second Quantization has some definite advantages. First, the particle antisymmetry is automatically accounted for. It is incorporated in the commutation relations (Equations 4.7, 4.8) which the operators obey. If the operators are manipulated in accordance with these rules, then the antisymmetrization of the resulting expressions is ensured. The second advantage stems from the factorability of the operators in this representation. A one-body operator, for example, can be expanded in terms of a linear combination of one-shell operators and therefore applied to a wide range of wavefunctions with little computational effort.

The diagonalization is carried out in a basis of good angular momentum (J) and good isospin (T). That is, angular momentum and isospin are treated as conserved quantities so each eigenvector has a definite value for each.

In electron scattering the motion of the nuclear centre of mass is determined by the kinematics. The excitation of the nucleus has no effect upon the centre of mass motion other than to increase the nuclear mass. Immediately after the interaction with the electron, the nucleus moves as a free particle. It should therefore be possible to transform to an inertial frame in which the centre of mass of the excited nucleus is at rest. In this frame the nuclear system has only $3(A-1)$ degrees of freedom where A is the number of nucleons in the nucleus. This follows from the fact that after the positions of the first $A-1$ nucleons have been specified, the position of the A^{th} is determined by the restriction on the centre of mass. Also, it is to be noted that the centre of the potential generated by these nucleons is not necessarily at rest in this frame, but is free to move.

This physical situation is to be contrasted with the shell model description of the nucleus. In this model the centre of the potential is assumed fixed and all A nucleons are free to move within the potential. Therefore, the model system has one more degree of freedom than the physical system it represents. This corresponds to the centre of mass being free to move.

This deficiency in the model gives rise to the problem of 'spurious states'. Some of the excited states predicted by the model correspond to excitations of the centre of mass of the nucleus. These states are physically unacceptable and must, if possible, be discarded.

This problem proves tractable under some conditions. If 1) the basis set of nuclear wavefunctions has a fixed J , 2) the single-particle wavefunctions are eigenstates of a spherically symmetric harmonic oscillator Hamiltonian, and 3) the basis comprises one or more complete degenerate (in absence of spin-orbit forces) sets of harmonic oscillator multi-particle states, then it

is possible to transform the basis set to one composed of two distinct subsets:

- 1) 'nonspurious states' in which each basis state has its centre of mass in a $| 0_s \rangle$ (i.e., lowest possible) state,
- 2) 'spurious states' in which each basis state has centre of mass dependence orthogonal to $| 0_s \rangle$, but has internal structure identical to that of a nonspurious state.

Several methods have been devised for finding this transformation. The one employed in the Oak Ridge-Rochester code is based on the fact that the diagonalization of any translationally invariant Hermetian operator produces orthonormal states which are eigenstates of the centre of mass Hamiltonian. The above diagonalization is performed using an arbitrary operator and from the results the nonspurious states are selected. These are used to construct a non-square transformation matrix $[U]$.

The original Hamiltonian matrix $[H]$ is also diagonalized, with its eigenstates containing both spurious and nonspurious contributions. The U transformation is then applied to H :

$$H_{ns} = U^+ H U \quad . \quad (4.16)$$

The resulting matrix $[H_{ns}]$ is now expressed in terms of the basis composed of the nonspurious states. The eigenstates of this matrix are, therefore, the desired eigenstates of the internal Hamiltonian. They can be expressed in terms of the computationally more convenient harmonic oscillator multi-particle states simply by applying the inverse of the U transformation.

IV.2.3 Calculation of Form Factors

The form factors which describe the electroexcitation of the excited states

are directly related to the reduced matrix elements (Edmonds 58) of the electromagnetic operators \hat{M}_J^{Coul} , \hat{T}_J^{el} , \hat{T}_J^{mag} between the ground and excited states (Equations 2.14 - 2.18). Since these states are linear combinations of the multi-particle basis states, the above matrix elements can be similarly expressed as linear combinations of the matrix elements of the operators between multi-particle basis states. Furthermore, since these operators are one-body operators these matrix elements are equivalent to matrix elements between single-particle states. When the single-particle wavefunctions are harmonic oscillator wavefunctions the reduced matrix elements can be written in closed form (de Forest 66). The expressions, which are rather complicated, are given in Appendix D.

The angular momentum coupling required to obtain the reduced matrix elements between the ground and excited states from the individual state matrix elements is performed by the second half of the Oak Ridge-Rochester code. It returns matrix elements, reduced with respect to both angular momentum and isospin, for both the isoscalar $\langle \begin{smallmatrix} \vdots \\ \Delta T=0 \\ \vdots \end{smallmatrix} \rangle$ and isovector $\langle \begin{smallmatrix} \vdots \\ \Delta T=1 \\ \vdots \end{smallmatrix} \rangle$ parts of the interactions. In the nuclear states J , T , and M_T are good quantum numbers. Hence, the reduction with respect to isospin must be removed by applying the Wigner-Ekhardt Theorem (Edmonds 58):

$$\begin{aligned} \langle J_f T_f M_{T_f} || \hat{O} || J_i T_i M_{T_i} \rangle = \\ (T_i M_{T_i} 00 | T_f M_{T_f}) \langle J_f T_f \begin{smallmatrix} \vdots \\ \Delta T=0 \\ \vdots \end{smallmatrix} : J_i T_i \rangle / (2T_f+1)^{\frac{1}{2}} \\ (T_i M_{T_i} 10 | T_f M_{T_f}) \langle J_f T_f \begin{smallmatrix} \vdots \\ \Delta T=1 \\ \vdots \end{smallmatrix} : J_i T_i \rangle / (2T_f+1) . \end{aligned} \quad (4.17)$$

These matrix elements are then used to compute the desired form factors.

IV.2.4 Application to ^{17}O

The model used for the ^{17}O ground state was a core consisting of filled Os and Op shells plus a valence neutron in the Od5/2 shell. Attempts were made to improve upon this approximation by allowing for 3p-2h contributions. This, however, proved impractical as the dimension of the resulting Hamiltonian matrix exceeded three hundred. While it is possible to diagonalize a matrix of this size the accumulated effects of round-off errors render the result unreliable.

The negative parity $1 \hbar \omega_0$ excited states of ^{17}O were constructed using a complete basis set. That is, all possible promotions of one particle through an energy gap of one oscillator spacing were permitted. Thus, there were contributions arising from 2p-1h states having two particles in the Od-1s shell and a hole in the Op shell, and from 1p-0h states generated by the promotion of the valence (Od5/2) neutron to the Of-1p shell.

As a check on the consistency of the results, the energy level spectrum of ^{16}O (< 15 MeV excitation) was also calculated. In this case a complete basis set of $1 \hbar \omega_0$ excitations consisting of 1p-1h states was used.

The single-particle energies for the Op and 1s-Op shells were taken (Jolly 63) from the level spectra of ^{17}O and ^{15}O . Those for the Of-1p shell were proposed by Jolly based upon the experimental results of Hardie et al (63) which predicted the Of7/2 single-particle strength to lie \approx 18 MeV. A splitting due to spin-orbit forces of about 7 MeV was assumed in order to establish the position of the Of5/2 single-particle strength. The position of the 1p3/2 shell was then assumed in order to preserve the order: Of7/2, 1p3/2, Of5/2. The single-particle energies used are listed in Table 4.1.

Two forms were used for the residual two-body interaction. The first was the Boeker-Brink interaction (Brink 67). This interaction has a simple con-

Table 4.1 Neutron Single-Particle Energies
(with respect to ^{16}O)

| Shell | Energy (MeV) |
|-------|--------------|
| 0p3/2 | -21.74 |
| 0p1/2 | -15.60 |
| 0d5/2 | -4.15 |
| 1s1/2 | -3.28 |
| 0d3/2 | 0.93 |
| 0f7/2 | 15.0 |
| 1p3/2 | 20.0 |
| 0f5/2 | 22.0 |

venient form with six free parameters:

$$V^r(r) = S_1 (1 - m_1 + m_1 P_M) e^{-\mu_1^2/r^2} + S_2 (1 - m_2 + m_2 P_M) e^{-\mu_2^2/r^2}, \quad (4.18)$$

where P_M is the Majorana exchange operator. The parameters were determined by Brink who chose various sets (μ_1, μ_2) and then fitted the other four to ^4He and to nuclear matter. The values of the parameters used were those which were found to be the best for fitting the level structure of ^{16}O . These parameters are listed in Table 4.2. The calculation of the two-body matrix elements from this potential is a straightforward but tedious task which is outlined in Appendix C.

Table 4.2 Parameters Used in Boeker-Brink Interaction

$$\begin{aligned} S_1 &= -140.6 \text{ MeV} & S_2 &= 389.5 \text{ MeV} \\ m_1 &= 0.4864 & m_2 &= -0.529 \\ \mu_1 &= 1.4 \text{ fm} & \mu_2 &= 0.7 \text{ fm} \end{aligned}$$

The second form used was the Kuo-Brown (Kuo 66) interaction. It is based upon the phenomenological two nucleon interaction of Hamada and Johnson (62) but contains several corrections. These corrections arise from the fact that the two nucleons involved in the interaction are not free, but are affected by the presence of all of the other nucleons. This form involves central, tensor, and spin-orbit contributions and because of its general form has proven to be quite realistic.

CHAPTER V

RESULTS AND CONCLUSIONSV.1 Giant Resonance RegionV.1.1 Experimental Results

The results of the data analysis are presented in Figures 5.1 to 5.5 as differential form factors. The differential form factor is defined by:

$$| F |^2 = \frac{z^2}{\sigma_M} \frac{d^2\sigma}{d\Omega d\epsilon_2} \quad (5.1)$$

and σ_M is the Mott cross-section given by Equation 2.12. The data points are separated by 100 keV and the error bars reflect counting statistics only.

Examination of the gross structures in these figures reveals two prominent features. First, there is the definite peaking of the cross-section at approximately 22 - 23 MeV. It is not clear that one can assign a width to this structure since it lies atop a broad quasi-elastic continuum (see Appendix B). Furthermore, it is somewhat unrealistic to regard the two contributions as distinct as they actually correspond to different approximations for calculating the same process which are valid in different regions.

The second gross feature to be noted is the large amount of strength extending down as far as 10 MeV excitation. Several sharp peaks are superimposed upon this strength, but the underlying strength itself shows no sign of finer structure.

Comparing these data to electron scattering data taken on ^{16}O by Hotta et al (74) one notices at least two significant differences. First, the ^{16}O resonance is narrower, rising sharply at 21 MeV and falling abruptly at 26 MeV excitation.

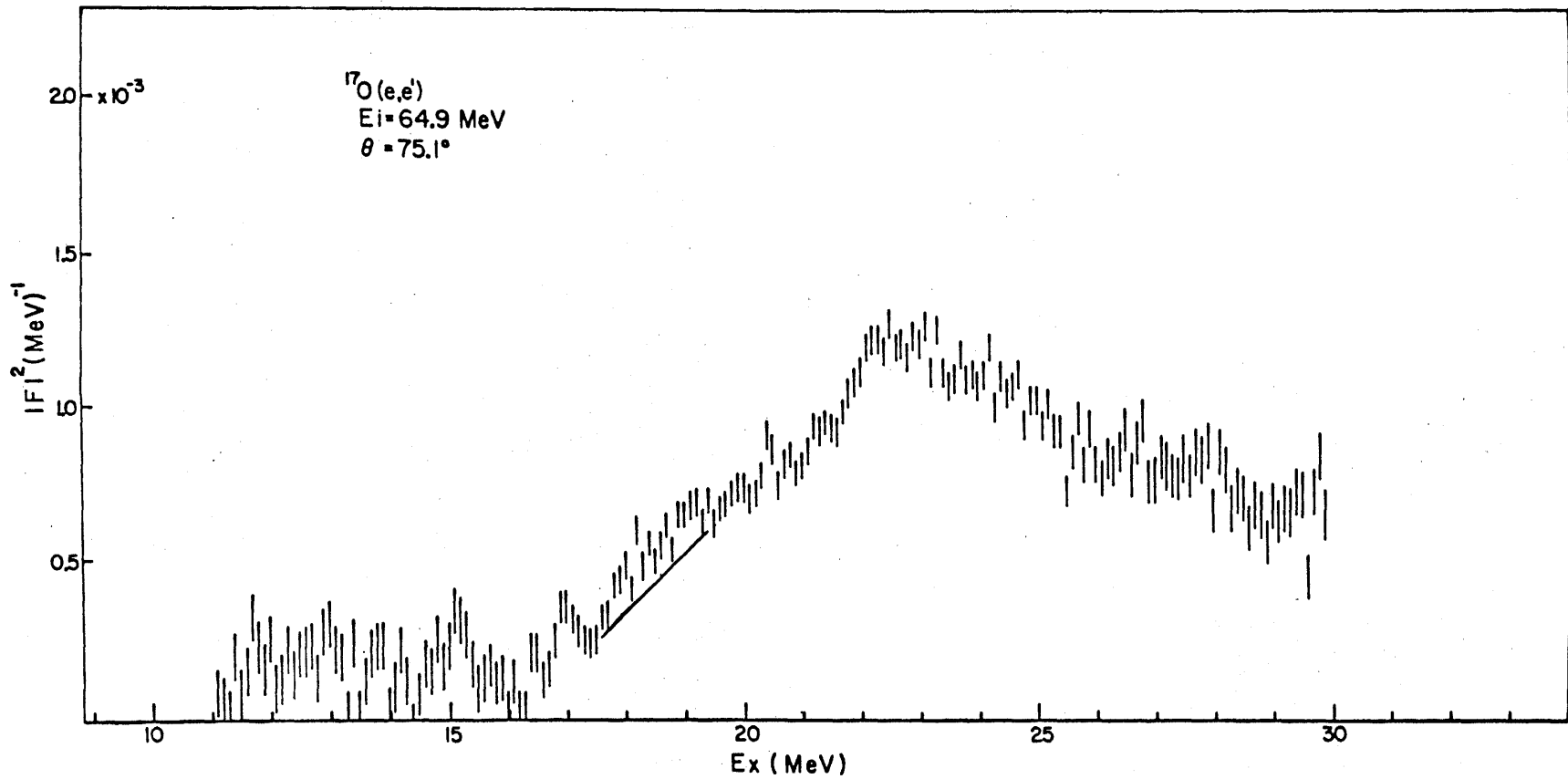


Figure 5.1 Differential form factor (squared) for the electroexcitation of ^{17}O . Tail subtraction and radiative corrections applied as described in text. Error bars reflect counting statistics.

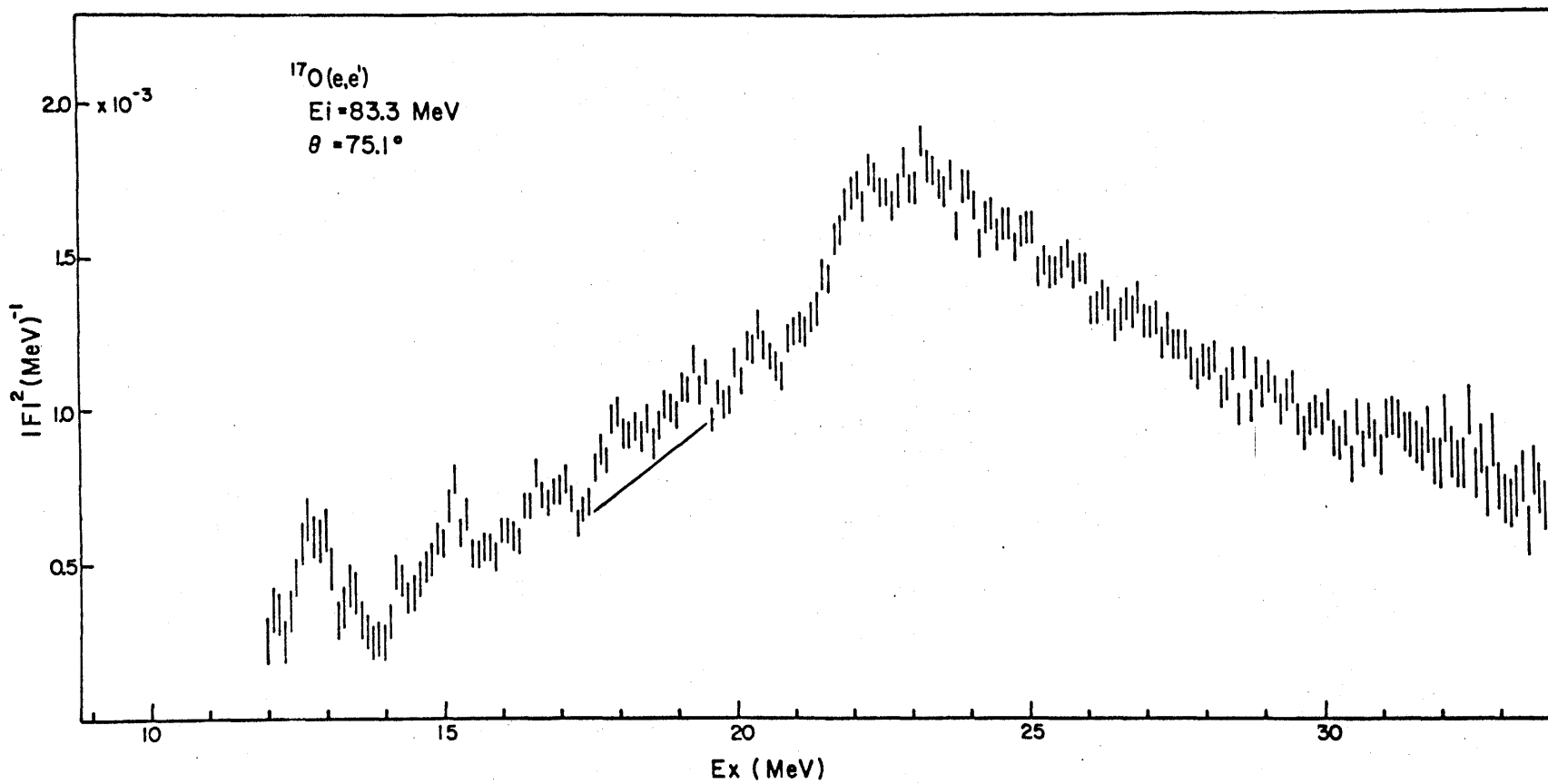


Figure 5.2 Differential form factor (squared) for the electroexcitation of ^{17}O .

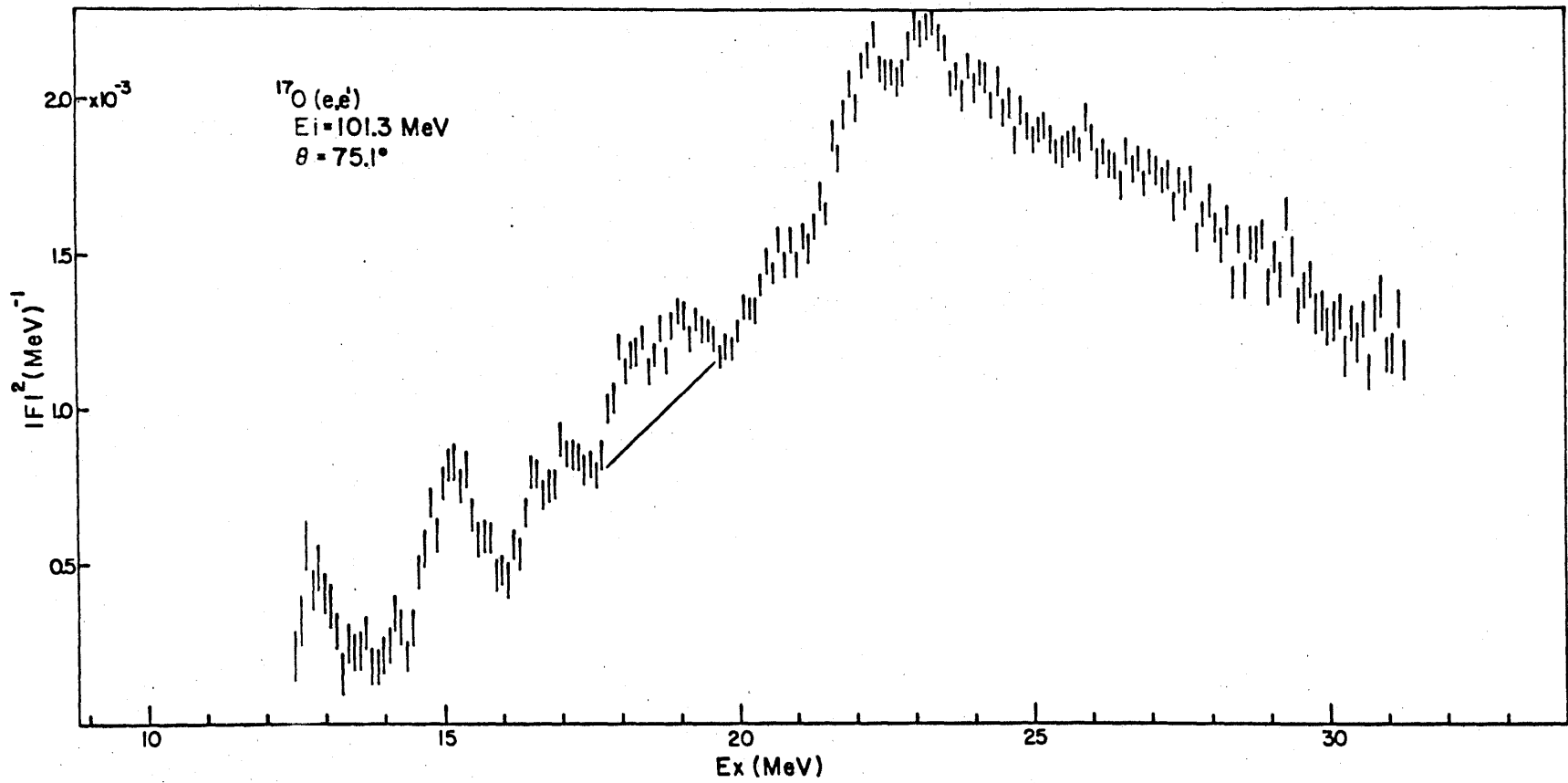


Figure 5.3 Differential form factor (squared) for the electroexcitation of ^{17}O .

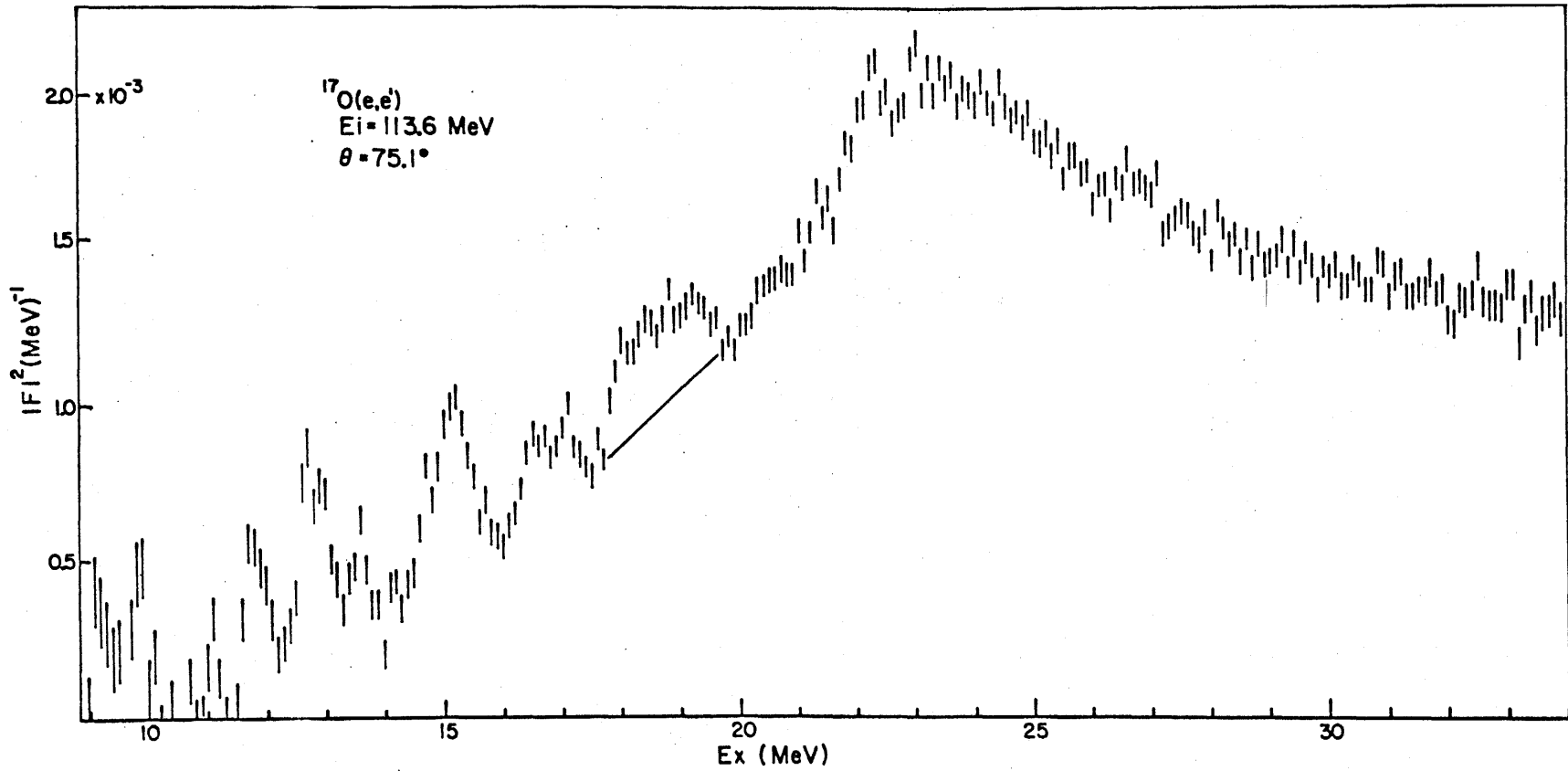


Figure 5.4. Differential form factor (squared) for the electroexcitation of ^{17}O .

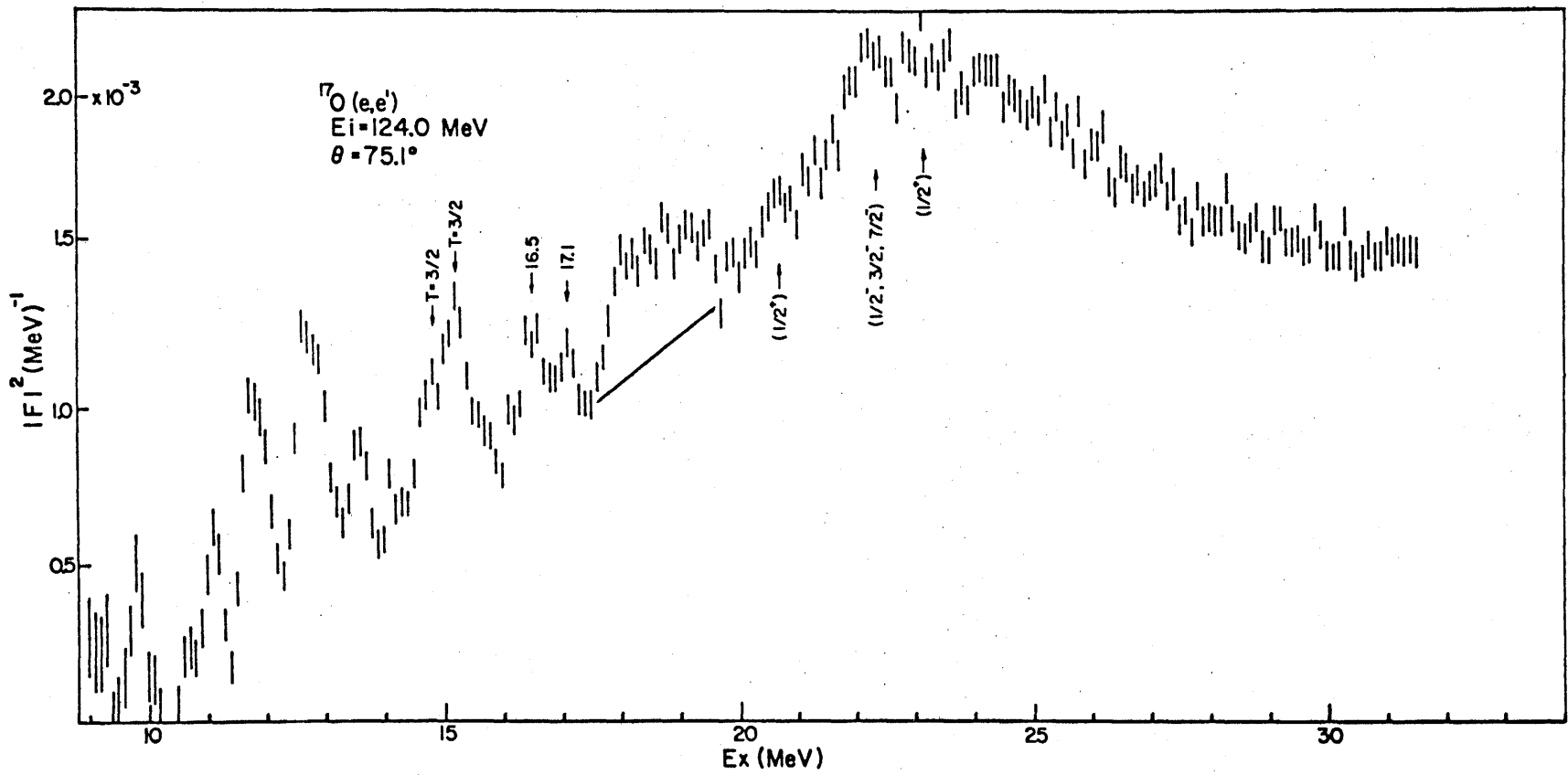


Figure 5.5 Differential form factor (squared) for the electroexcitation of ^{17}O .

Second, the ^{16}O giant resonance is composed of three distinct peaks (22, 23, 24 MeV), whereas the ^{17}O resonance is less structured and is broader in energy.

That the structures tend to be more sharply defined in ^{16}O than in ^{17}O is not unexpected in spite of the similarities between the two nuclei. The ^{16}O ground state has angular momentum $J=0$ whereas ^{17}O has a $J=5/2$ ground state. Therefore, an $L=2$ operator, for instance, can only excite ^{16}O to $J=2$ states whereas the same operator can excite $J=1/2, 3/2, 5/2, 7/2, 9/2$ states in ^{17}O .

Three small peaks were also observed above 20 MeV excitation. The first appears at 20.5 MeV, and corresponds to the $J^\pi = 1/2^+$ state reported by Johnson et al (61). As in the case of the main resonance it is difficult to assign a width to this peak. However, it would appear that the width of the state is not less than about 300 keV.

The second bump occurs at about 22 MeV, while the third occurs at 23 MeV excitation. Two peaks were observed in the reactions $^{14}\text{C}(^3\text{He},n)^{16}\text{O}$ and $^{14}\text{C}(^3\text{He},\gamma)^{17}\text{O}$ near 22 MeV (21.7, 22.1) by Keyser et al (71). They also observed a level at 23.0 MeV. They assigned to these levels widths of 750 keV, which would explain why we were unable to resolve the 21.7 and 22.1 MeV levels.

These three levels have been assigned the following spins and parities by the same authors:

$$\begin{array}{ll} 21.7 \text{ MeV} & - 5/2^+ , \\ 22.1 & - 7/2^- , \\ 23.0 & - 1/2^+ . \end{array}$$

Work by T. Mo et al (72) involving the reactions $^{14}\text{N}(\tau,\alpha)^{13}\text{N}$ and $^{14}\text{N}(\tau,\gamma)^{17}\text{F}$ showed a similar triplet of levels in the ^{17}F spectrum:

$$\begin{array}{ll} 19.4 \text{ MeV} & - 5/2^+ , \\ 20.3 & - 7/2^- , \end{array}$$

21.0 MeV - $1/2^+$.

It was also observed that each level in ^{17}O has the same decay scheme as the corresponding level in ^{17}F . This would tend to indicate that these levels are mirror levels. Unfortunately, the information on the states in the 18 - 20 MeV region of ^{17}F is not sufficient to identify a possible mirror state for the 20.5 MeV, $J=1/2^+$ level in ^{17}O .

In the region 17.5 to 19.6 MeV excitation in ^{17}O is found a broad structure which has not been previously observed. It rises very sharply from the bulk of the resonance, especially in Figure 5.5. Its almost rectangular shape indicates that it is not a single resonance but is composed of several relatively narrow peaks. No similar broad structure is found in ^{16}O , but a sharp, strong (C2,E2) (see Appendix D), level is observed at 18.5 MeV (Hotta 74).

V.1.2 Comparison to Theory

The first test of the particle-hole calculation (Chapter IV) was the calculation of the low-lying negative parity states of ^{16}O and ^{17}O . The results of this test are presented in Figures 5.6 and 5.7. In spite of the simplicity of the model, comparison with experiment is favourable. The Boeker-Brink matrix elements give the better fit to the ^{16}O spectrum, but this is not surprising since this nucleus was used as the standard in choosing the parameters for the potential. In the ^{17}O spectrum, however, the Kuo-Brown matrix elements provide the best results. In particular, they do a much better job in predicting the observed level density in the 7 to 10 MeV range.

The next step was to calculate theoretical spectra for comparison to the electron scattering data. The calculation was first performed using the Boeker-Brink matrix elements. It was assumed, as a first approximation, that the transitions were of purely C1 character. Since the particle-hole model

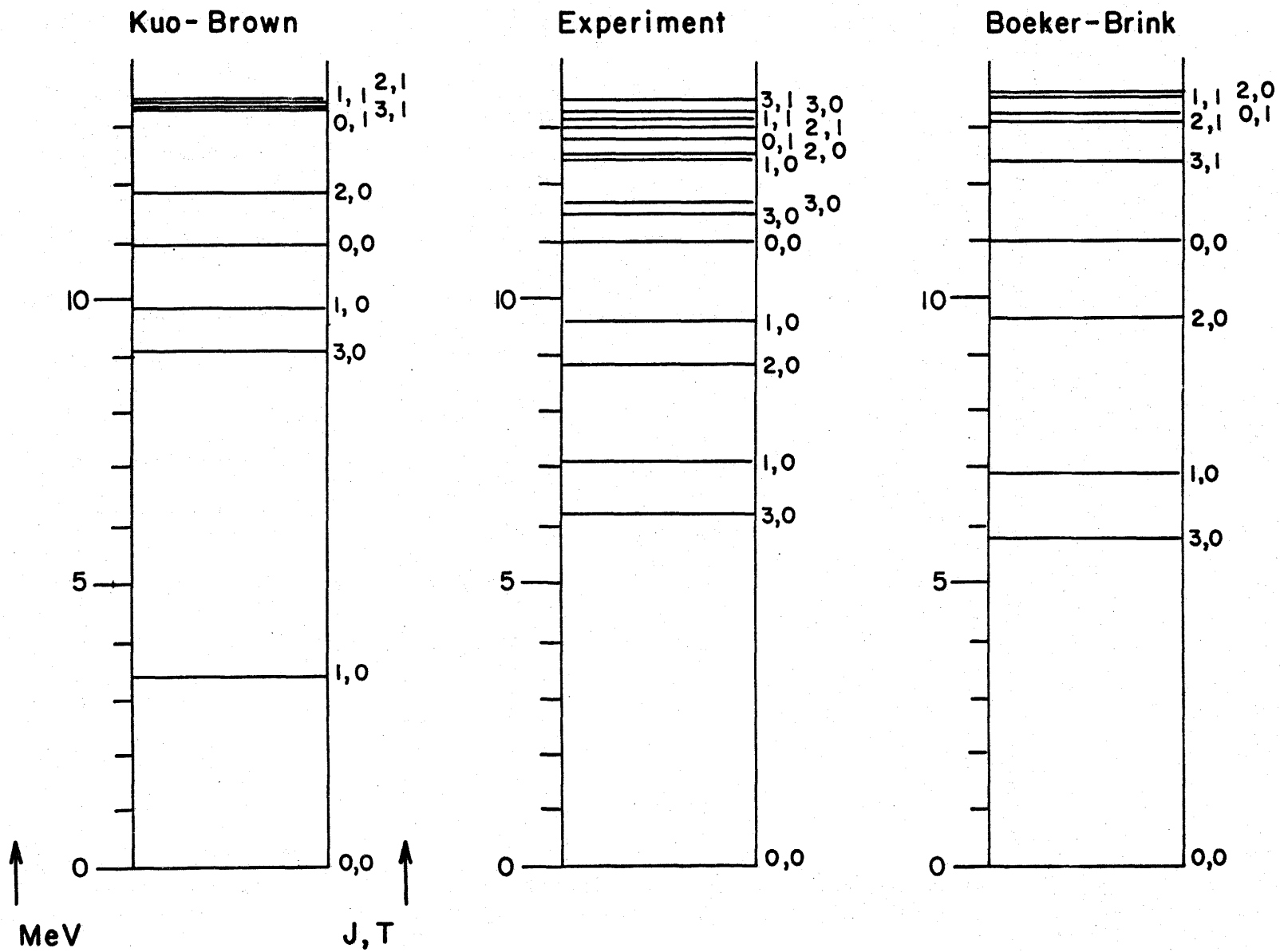


Figure 5.6 Low lying energy levels of ^{16}O .

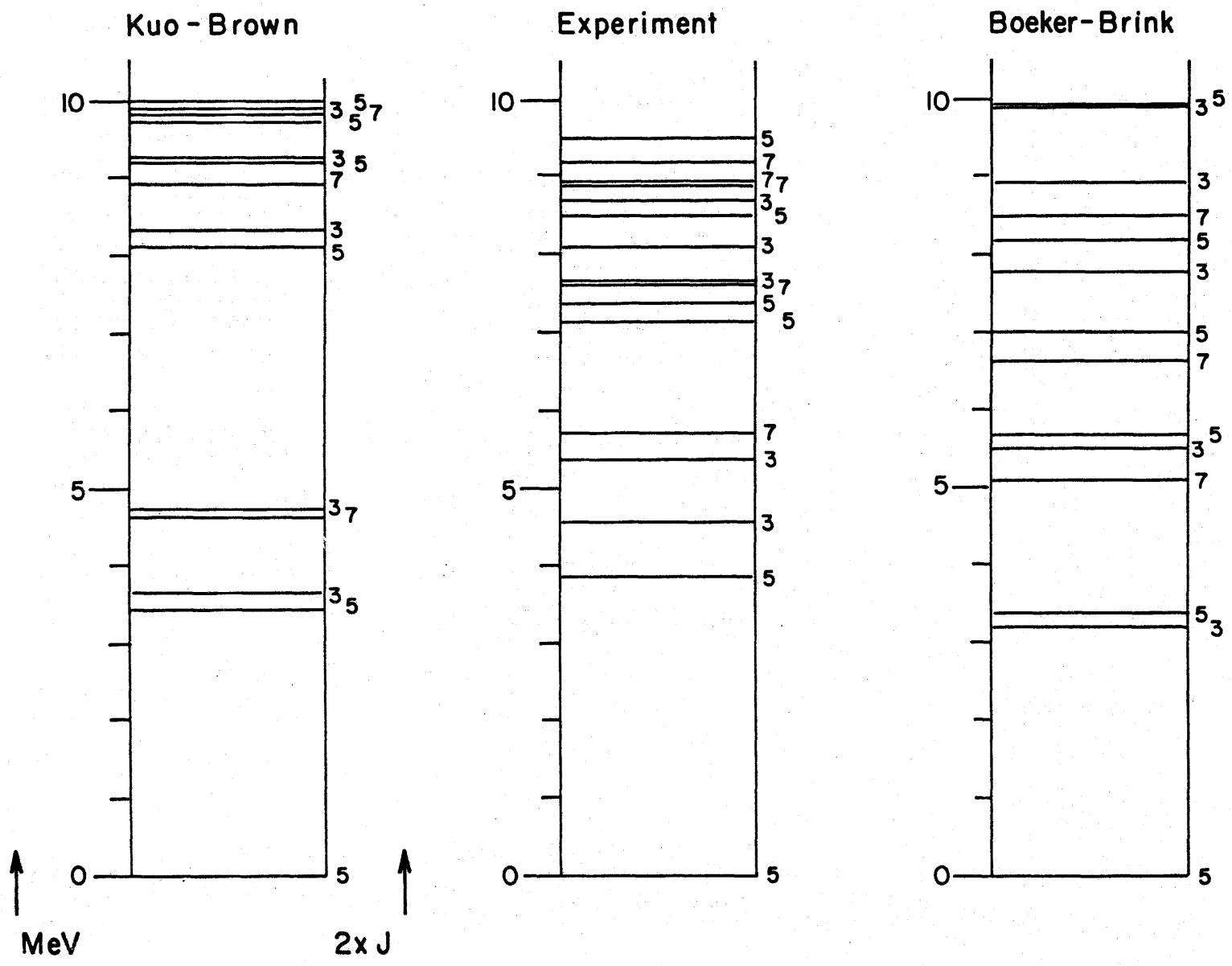


Figure 5.7 Low lying energy levels of ^{17}O

predicts discrete states whereas the giant resonance is actually very broad, the theoretical form factors were integrated over 1 MeV intervals and are presented as differential form factors with respect to excitation energy. The result of this work is shown in Figure 5.8. The obvious failure to even predict the energy of the giant resonance using the Boeker-Brink matrix elements led to the use of the Kuo-Brown matrix elements.

Using the Kuo-Brown matrix elements, five spectra were calculated. In this case the transverse E1 contribution was included. The results of this work appear in Figures 5.9 to 5.13.

These results are immediately seen to be a vast improvement over those obtained using the Boeker-Brink matrix elements. Not only do the dominant peaks fall at the experimentally observed levels, but the significant strength observed to both sides of the centroid of the ^{17}O giant resonance is also predicted.

To obtain a more quantitative measure of the theoretical predictions, the theoretical and experimental spectra were integrated over the energy ranges 20 - 25, 25 - 30, and 20 - 30 MeV and the results compared (see Table 5.1). The theoretical predictions were found to be low in every case so the ratios between the theoretical and experimental integrated form factors were taken.

Two features of the data presented in Table 5.1 are particularly interesting. First, the consistency of the ratios with changing q shows that the q -dependence of the resonance is correctly predicted by the particle-hole model. Second, the similarity between the ratios for the 20 - 25 and 25 - 30 MeV ranges shows that the strength distribution is also accurately predicted.

The consistency of the ratios suggested that the theoretical predictions be scaled and then compared to experiment. This was done and the results are pre-

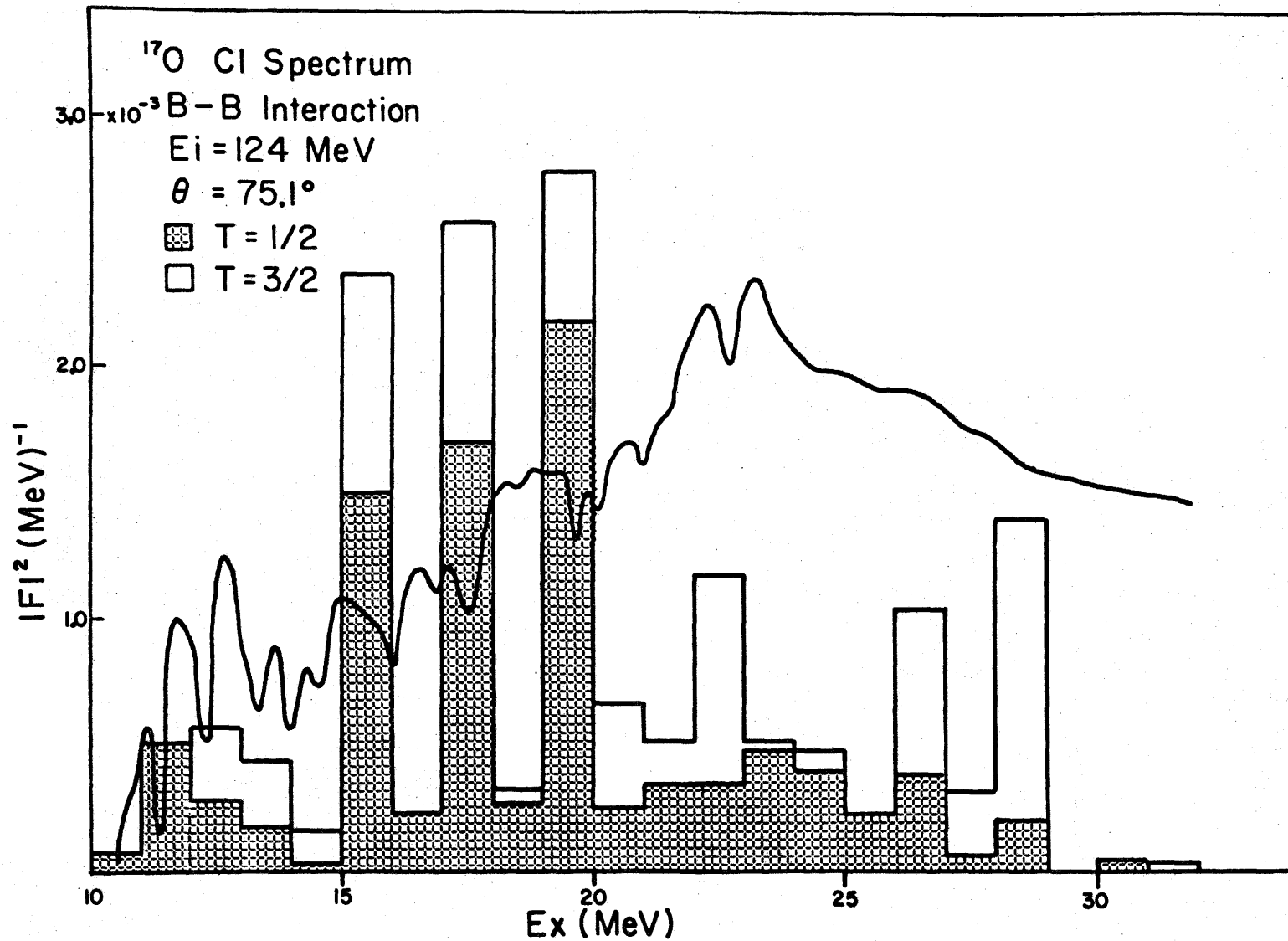


Figure 5.8 Theoretical differential form factor (squared) for the electroexcitation of ¹⁷O calculated using the particle-hole model with Boeker-Brink residual interaction.

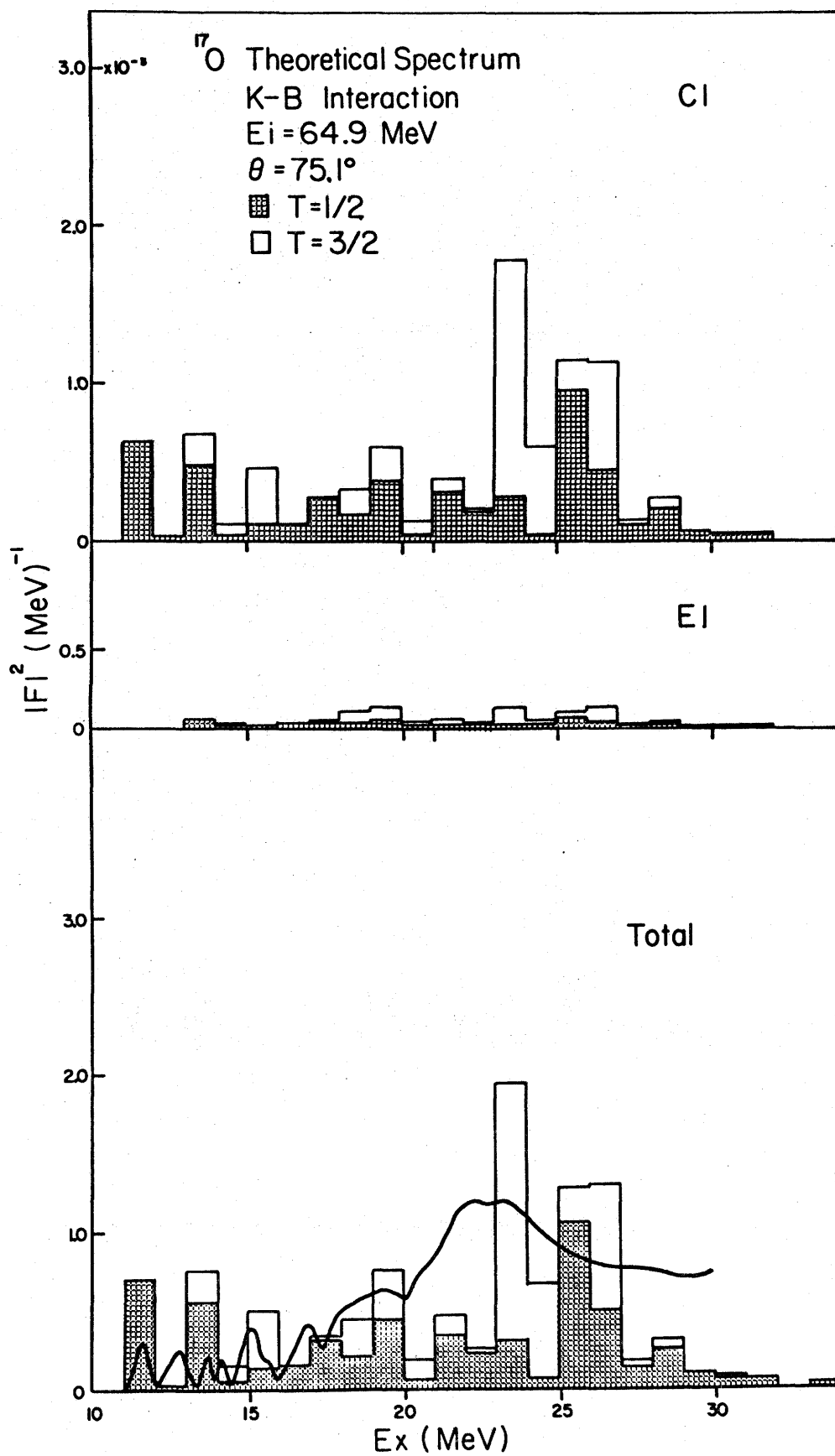


Figure 5.9 Theoretical differential form factor (squared) for the electroexcitation of ^{17}O calculated using the particle-hole model with Kuo-Brown residual interaction.

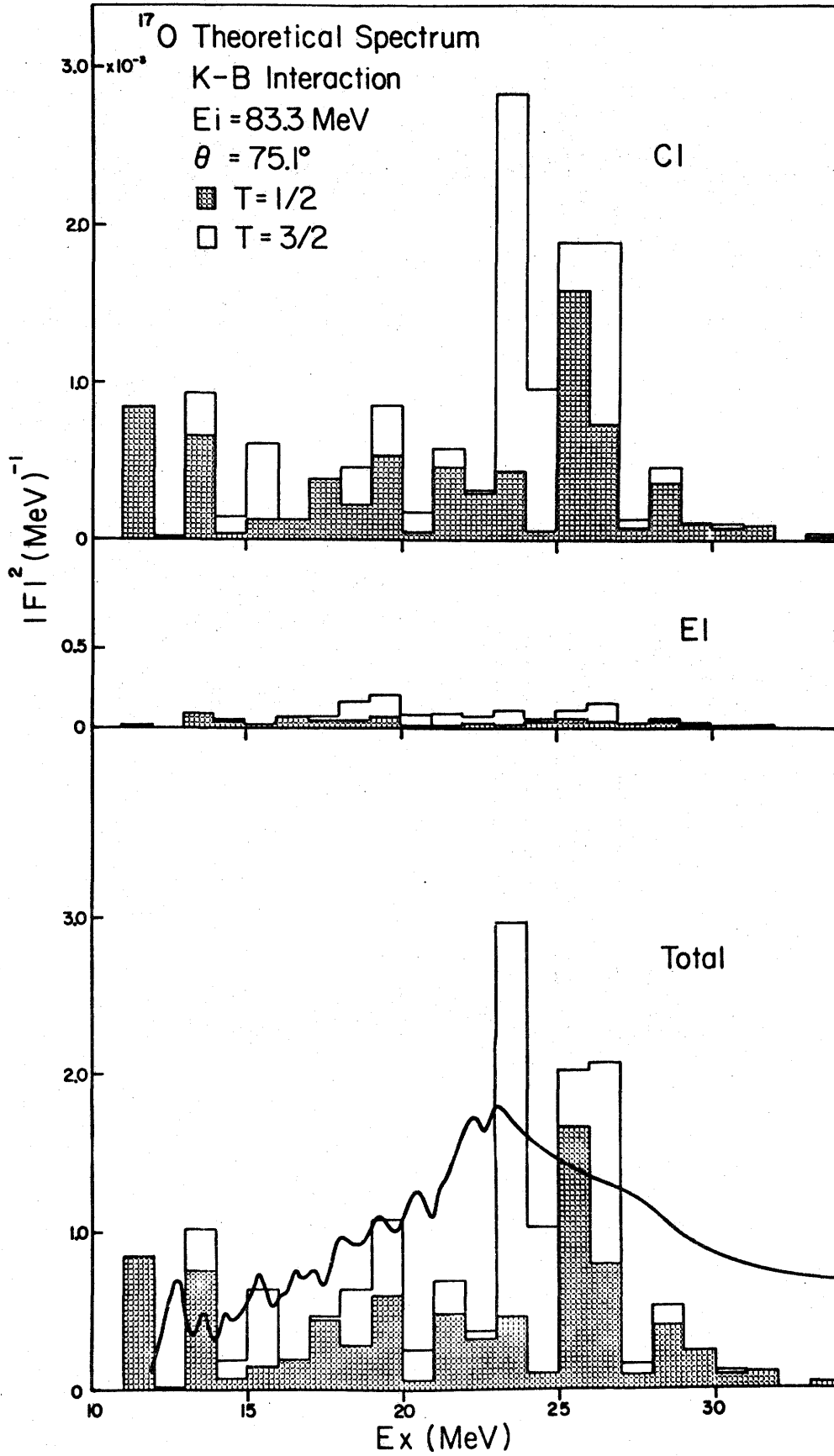


Figure 5.10 Theoretical differential form factor (squared) for the electroexcitation of ¹⁷O.

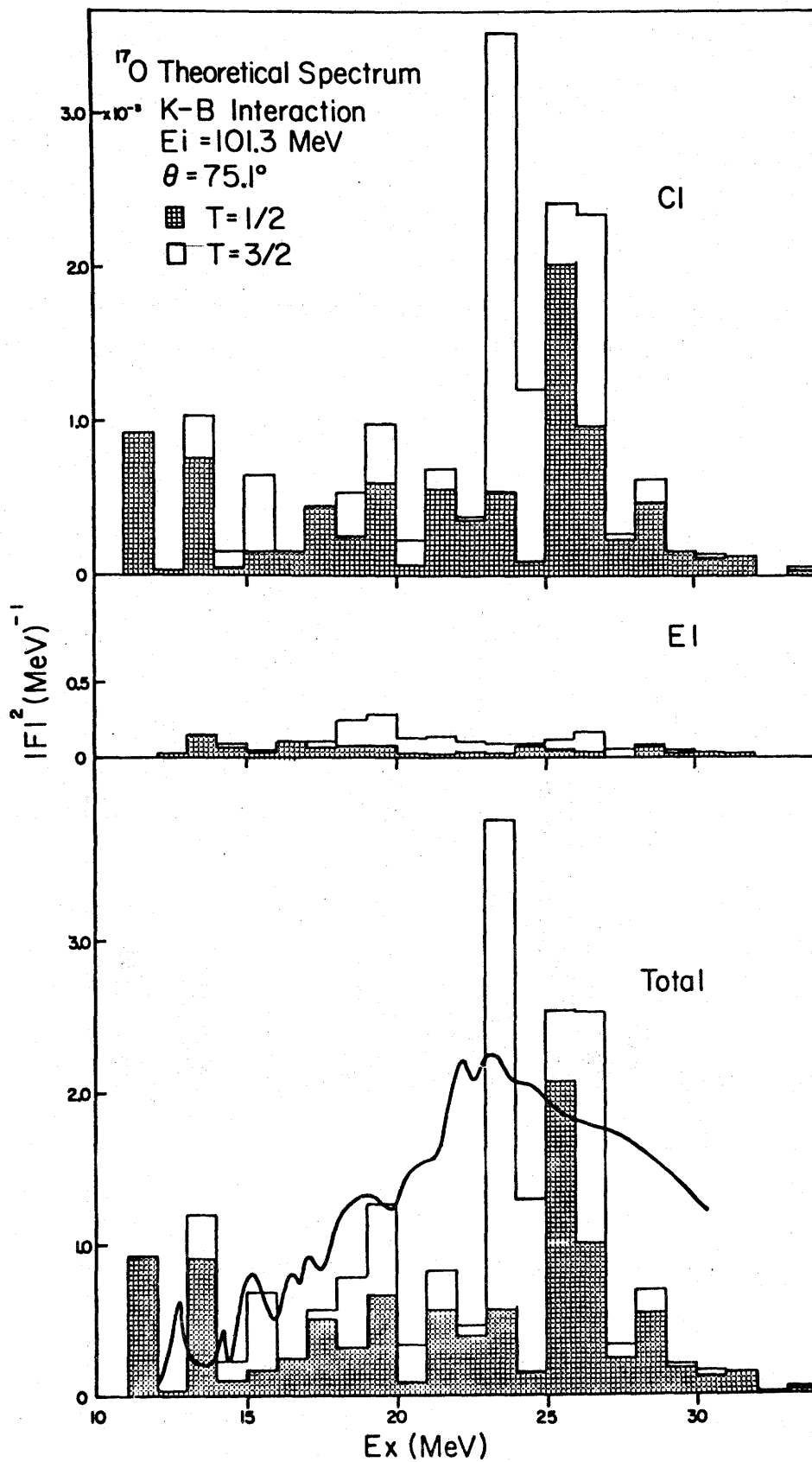


Figure 5.11 Theoretical differential form factor (squared) for the electroexcitation of ^{17}O .

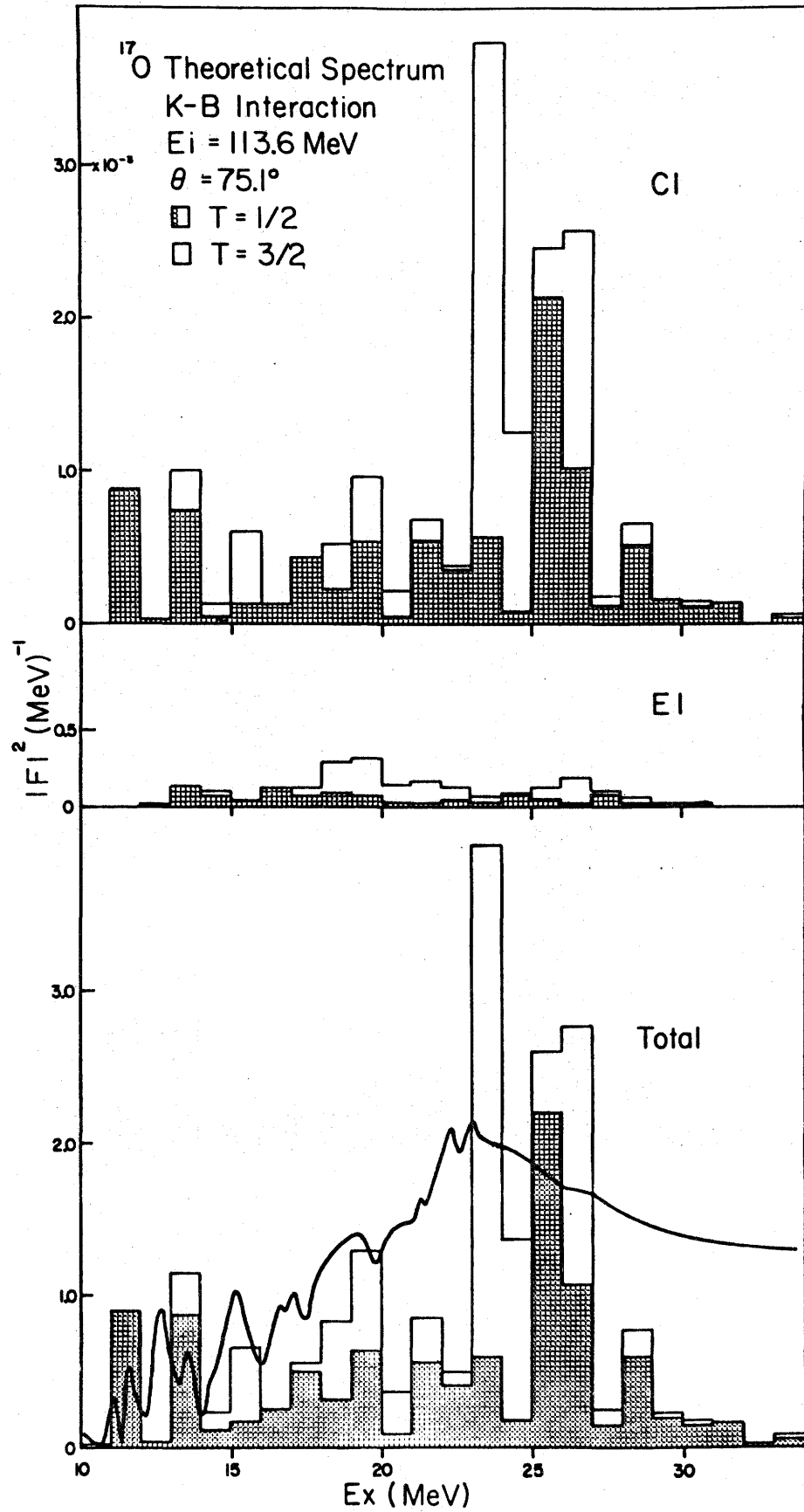


Figure 5.12 Theoretical differential form factor (squared) for the electroexcitation of ¹⁷O.

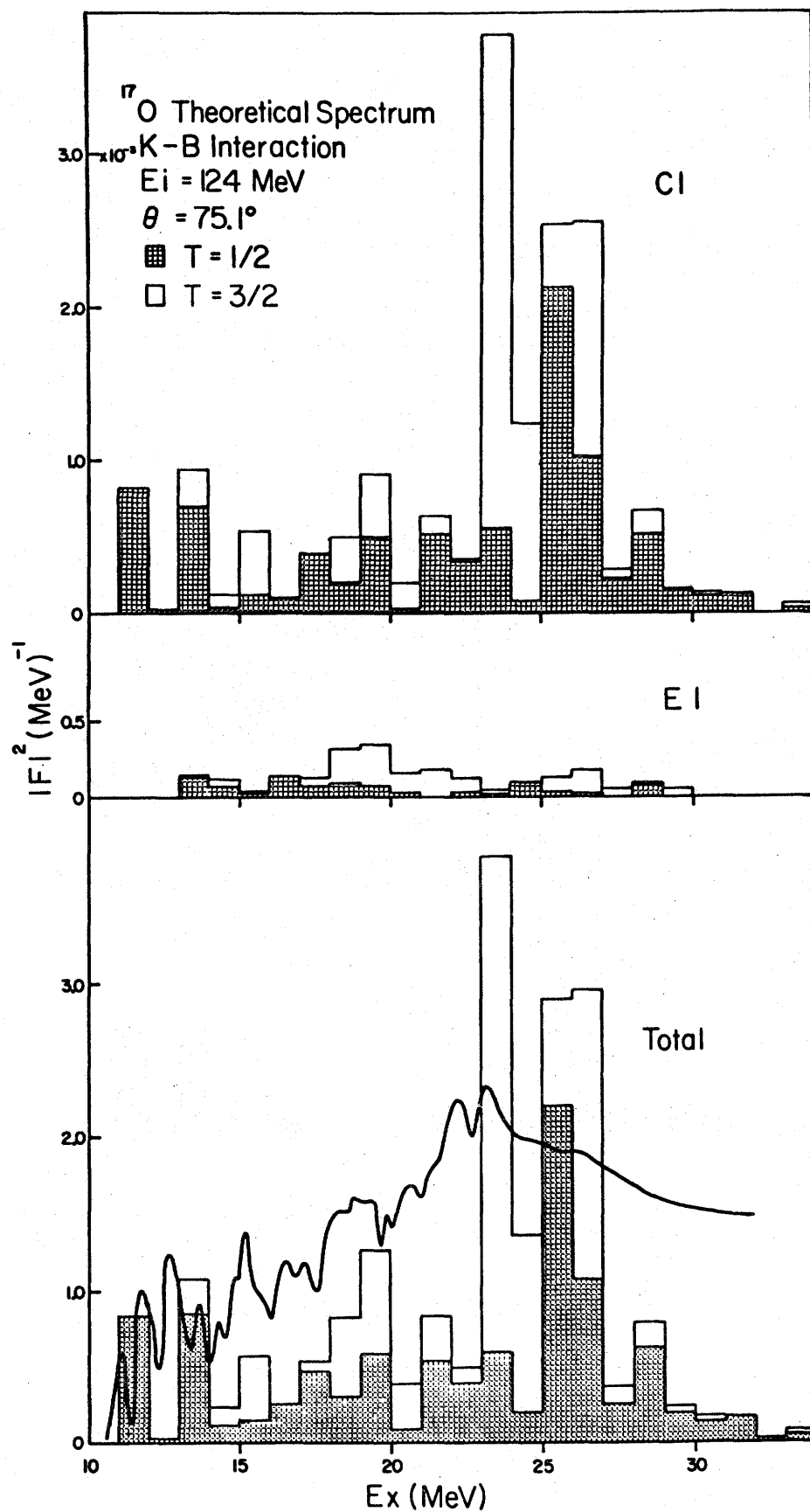


Figure 5.13 Theoretical differential form factor (squared) for the electroexcitation of ^{17}O .

Table 5.1 Experimental and Theoretical Form Factors

E = Exp't, T = Theory, R = T/E = Ratio

| <u>E_{inc} (MeV)</u> | | <u>20 - 25 MeV</u> | <u>25 - 30 MeV</u> | <u>20 - 30 MeV</u> |
|------------------------------|-------|--------------------|--------------------|--------------------|
| 64.9 | T | 0.348 E-2 | 0.311 E-2 | 0.659 E-2 |
| | E | 0.612 E-2 | 0.590 E-2 | 1.202 E-2 |
| | R | 0.570 | 0.527 | 0.549 |
| 83.3 | T | 0.532 E-2 | 0.492 E-2 | 1.024 E-2 |
| | E | 1.06 E-2 | 0.98 E-2 | 2.04 E-2 |
| | R | 0.502 | 0.502 | 0.502 |
| 101.3 | T | 0.651 E-2 | 0.627 E-2 | 1.28 E-2 |
| | E | 1.22 E-2 | 1.16 E-2 | 2.38 E-2 |
| | R | 0.534 | 0.540 | 0.537 |
| 113.6 | T | 0.684 E-2 | 0.667 E-2 | 1.35 E-2 |
| | E | 1.25 E-2 | 1.17 E-2 | 2.42 E-2 |
| | R | 0.547 | 0.570 | 0.558 |
| 124.0 | T | 0.680 E-2 | 0.683 E-2 | 1.36 E-2 |
| | E | 1.29 E-2 | 1.19 E-2 | 2.48 E-2 |
| | R | 0.536 | 0.574 | 0.550 |
| | < R > | 0.536 | 0.543 | 0.539 |

sented in Figure 5.14. In this figure the error bars on the data points reflect both the counting statistics and the uncertainty in the tail subtraction. The latter was determined by trying various tails and examining their effects upon the resulting form factors.

When dealing with a nucleus having non-zero ground state isospin the question of isospin splitting of the giant resonance arises. Our results give no indication of isospin splitting as predicted by Easlea (61). Since the reaction $^{16}\text{O}(n,n)^{16}\text{O}$ excites only $T=\frac{1}{2}$ resonances in ^{17}O it would be interesting to compare the distribution of strength observed in this reaction to that observed in electron scattering. However, the only work on neutron scattering to the giant resonance region of ^{17}O (Boreli 70) covers only the region below 21 MeV excitation.

The particle-hole model calculation which was successful in explaining the giant resonance data gave little indication of this effect. Only in the transverse component (Figure 5.15) did any evidence of significant inhomogeneities in the distribution of $T=1/2$ and $T=3/2$ strength occur. Even there, the splitting was slight, very similar to that predicted by D. Albert (69), who performed a similar but more restricted calculation.

In order to determine the multipolarity of the transition giving rise to the structure between 17.5 and 19.6 MeV the Helm model (see Appendix E) was used. First, the giant resonance data were fitted using the Helm model prediction of the C1 form factor (Figure 5.14). The parameters used were:

$$g = 1.0 \text{ fm}$$

$$r_t = 2.78 \text{ fm}$$

These parameters were then used to calculate the best-fit C1 and C2 form factors for the 17.5 to 19.6 MeV structure. (see Figure 5.16). Here again, the error bars reflect both counting statistics and estimated tail uncertainty.

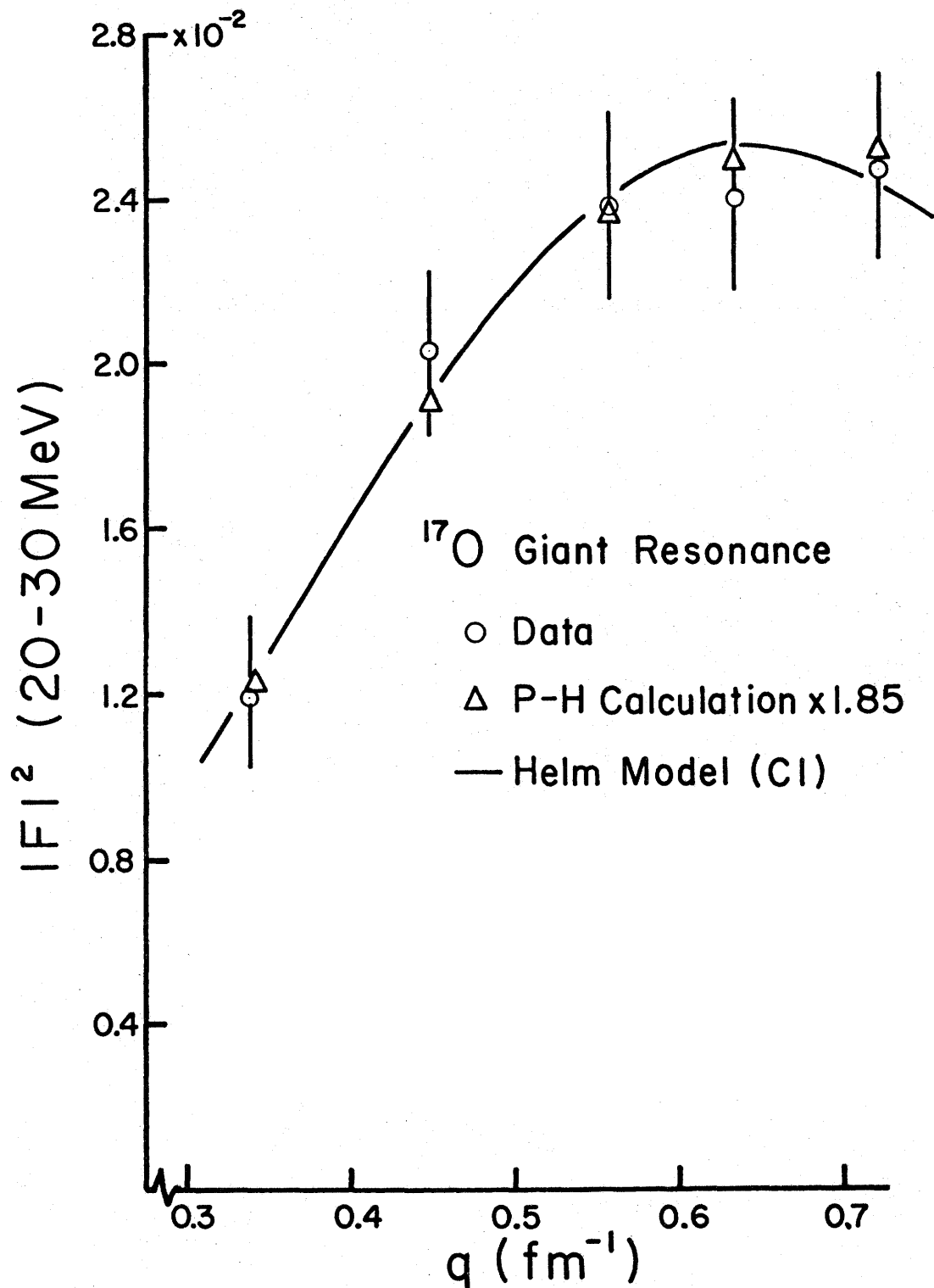


Figure 5.14 Experimental and theoretical form factors (squared) for the electro-excitation of the giant resonance of ^{17}O .

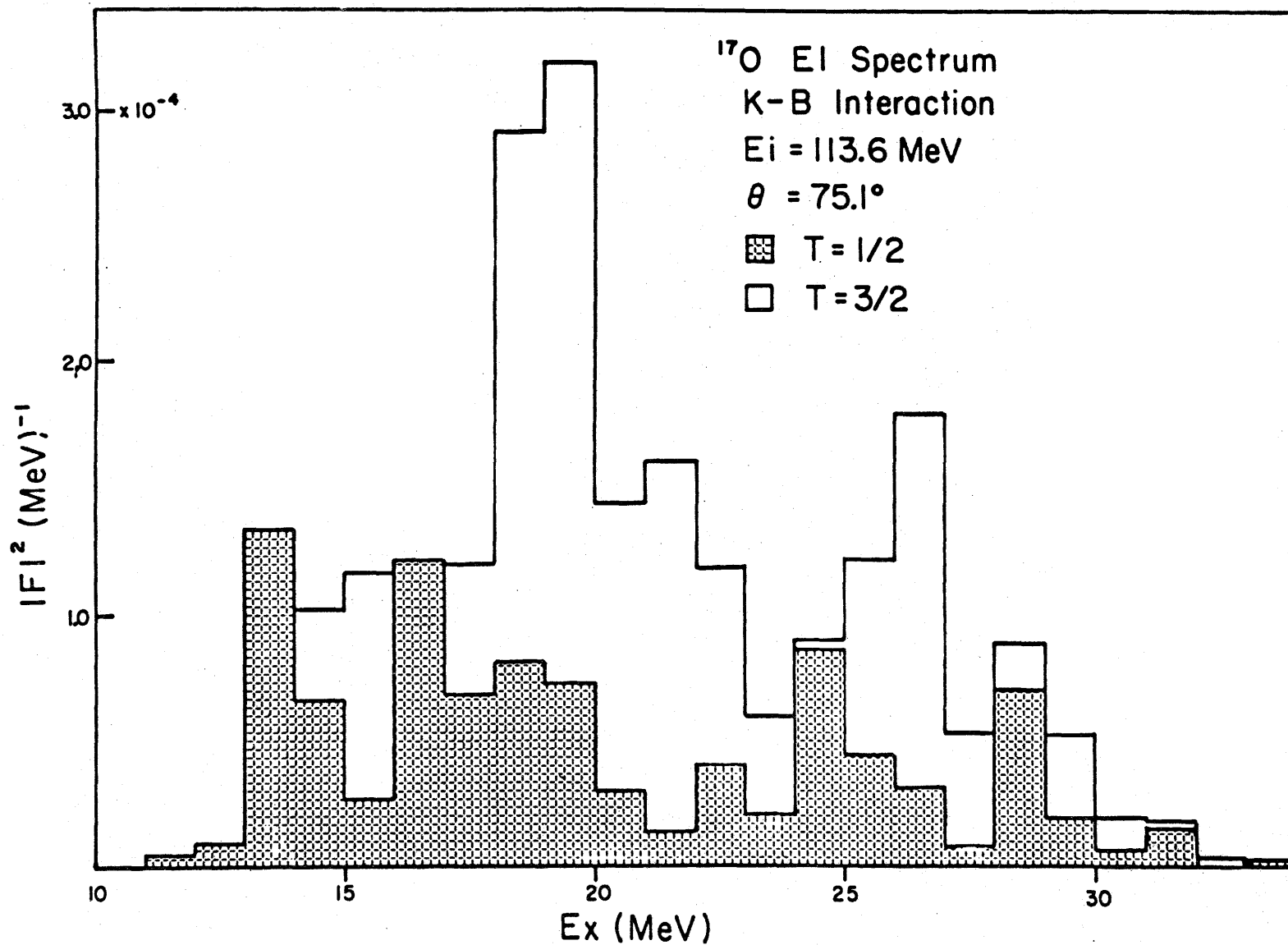


Figure 5.15 Theoretical differential transverse form factor (squared) for the electroexcitation of ^{17}O .

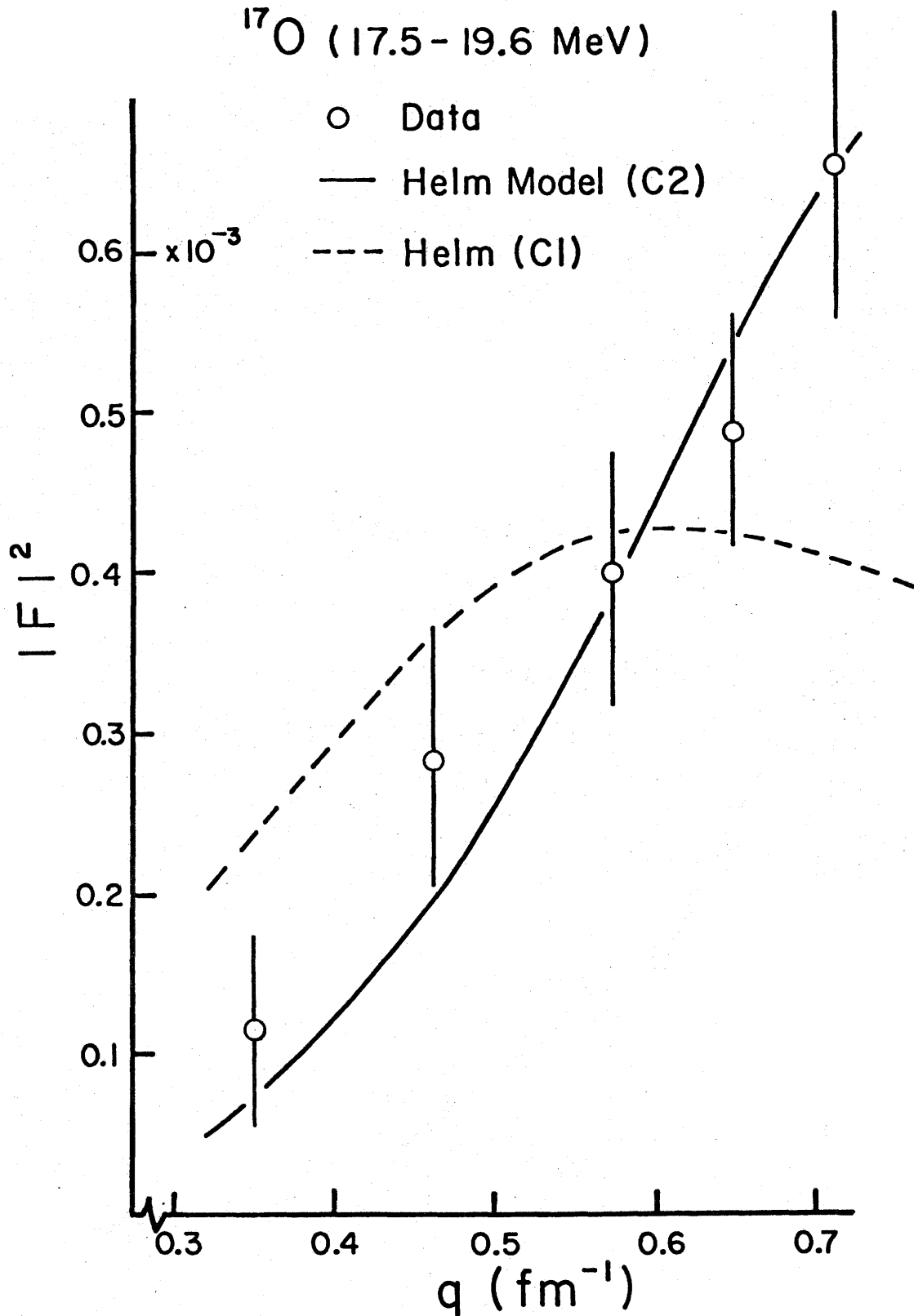


Figure 5.16 Experimental and theoretical form factors (squared) for the electro-excitation of the 17.5-19.6 MeV structure in ^{17}O .

The obviously good fit to the data by the C2 form factor provides a strong indication that the structure is predominantly excited by this mode. The presence in ^{16}O of a C2,E2 - excited state at 18.5 MeV suggests that the 17.5 - 19.6 MeV structure in ^{17}O may be composed of levels built upon the ^{16}O level. That is, the states in ^{17}O may consist of the valence ($0d_{5/2}$) neutron coupled to the ^{16}O core.

V.2 Inelastic (Discrete Levels) Region

Ten separate peaks were discerned between 11.5 and 17.5 MeV excitation. The spectrum with the best fit to these peaks is shown in Figure 5.17. Two of the spectra ($E_i = 64.9, 83.3$ MeV) were of significantly poorer quality. The narrow range of q ($\approx 0.55 - 0.71$) spanned by good data precluded any meaningful attempts to determine the multipolarity of the transitions to these levels. These data will, therefore, be presented with few comments (see Table 5.2).

The uncertainty in the widths attributed to these peaks is very hard to estimate. The significant role played by the positioning of the subtracted tail introduces a large probability of error since this was done in a somewhat arbitrary fashion (see Section III.2.6). The tail positioning, however, has only a minimal effect upon the peak positions. Hence, their determination is significantly more reliable.

Two of the more interesting peaks are the ones at 16.5 and 17.1 MeV. These fall in a region which has hitherto been unexplored. These data therefore furnish the first evidence for the existence of excited states in this region.

V.3 Conclusions

Cross-sections for the electroexcitation of ^{17}O to energies of 11 to 30

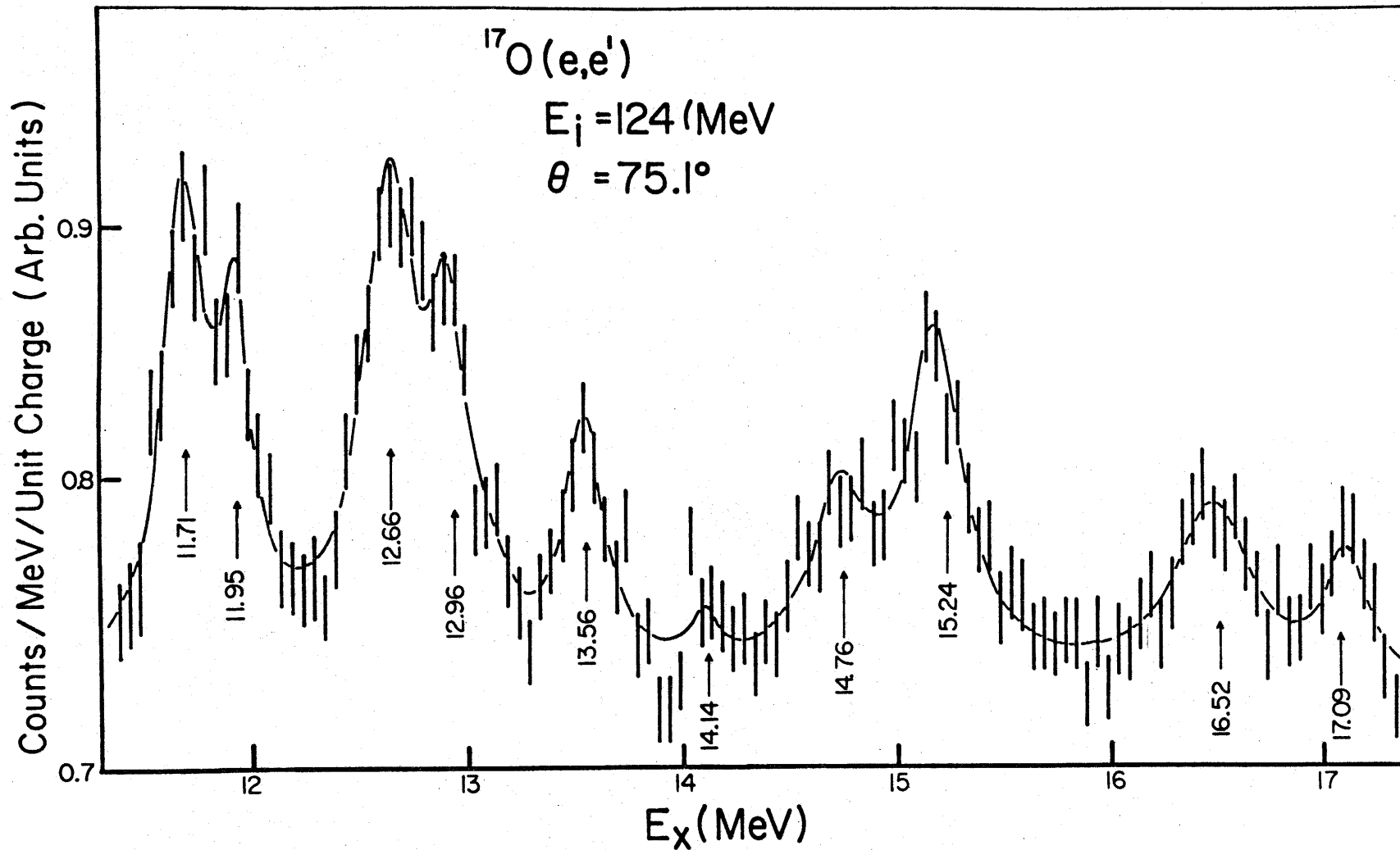


Figure 5.17 Differential form factor (squared) for the electroexcitation of the 11.5-17.5 MeV region in ^{17}O . Data points are 50 keV apart. Error bars reflect counting statistics only.

Table 5.2 Inelastic Levels Between 11.5 and 17.5 MeV

| Known* | | This Experiment | |
|------------------|----------------------------------|------------------|----------------------------------|
| <u>Ex (MeV)</u> | <u>Γ (keV)</u> | <u>Ex (MeV)</u> | <u>Γ (keV)</u> |
| 11.75 \pm 0.01 | 40 \pm 25 | 11.71 \pm 0.05 | Narrow |
| 11.95 | 270 | 11.95 \pm 0.05 | \approx 250 |
| 12.67 \pm 0.02 | \approx 75 | 12.66 \pm 0.05 | \approx 90 |
| 12.92 \pm 0.02 | | | |
| 12.95 \pm 0.01 | >150 | 12.96 \pm 0.05 | \approx 200 |
| 12.99 \pm 0.01 | | | |
| 13.61 \pm 0.02 | 250 \pm 100 | 13.56 \pm 0.05 | \approx 150 |
| 14.22 \pm 0.01 | | 14.14 \pm 0.10 | \approx 100 |
| 14.80 | | 14.76 \pm 0.10 | >300 |
| 15.10 \pm 0.01 | | 15.24 \pm 0.10 | \approx 200 |
| | | 16.52 \pm 0.05 | \approx 300 |
| | | 17.09 \pm 0.05 | Narrow |

* from Ajzenberg-Selove (71)

MeV have been measured for values of q ranging from 0.34 to 0.73 fm^{-1} . The scattering angle was maintained at 75.1° while incident electron energies of 64.9, 83.3, 101.3, 113.6, and 124.0 were used.

Particular attention was paid to the giant resonance region (20-30 MeV). The resonance was observed to be very broad, peaking at about 22 - 23 MeV excitation. Smaller peaks observed at 20.5, 22, and 23 MeV corresponded well to previously reported levels.

The transition strength ($C1, E1$) to the giant resonance was calculated using the particle-hole model with Boeker-Brink and Kuo-Brown residual interactions. The Tamm-Dancoff approximation was employed with both 2p-1h and 1p-0h states allowed. The complete $0d-1s$ and $0f-1p$ shells were used. The Boeker-Brink potential failed to predict even the correct energy of the resonance while the Kuo-Brown interaction successfully predicted the energy of the resonance, the q -dependence of the giant resonance form factors, and the distribution of strength throughout the 20 to 30 MeV range. A scale factor of 1.85 was required to bring the theory into agreement with the magnitude of the experimental strength. No evidence was found for isospin splitting of the $^{17}_0$ giant resonance.

A broad (2 MeV) structure centred at 18.5 MeV is reported for the first time. Its q -dependence was found to be that of a $C2$ transition as described by the Helm model. It is tempting to interpret it as resulting from the coupling of the $^{17}_0$ valence neutron to the 18.5 MeV $J^\pi = 2^+$ state in $^{16}_0$.

Several sharp peaks were observed in the region from 11.5 MeV to 17.5 MeV excitation (11.71, 11.95, 12.66, 12.96, 13.56, 14.14, 14.76, 15.24, 16.52, and 17.09 MeV). The first eight of these correlate well with known states. We report for the first time the existence of the last two (16.52, 17.09 MeV).

APPENDIX A

TARGET-IN BACKGROUNDA.1 Introduction

The presence of the target cell in the electron beam line means that large-angle scattering events other than single scattering from the enclosed gas may occur. The simplest of these is a double scatter from 1) either the entrance window or the enclosed gas and 2) the cell wall (Figure A.1).

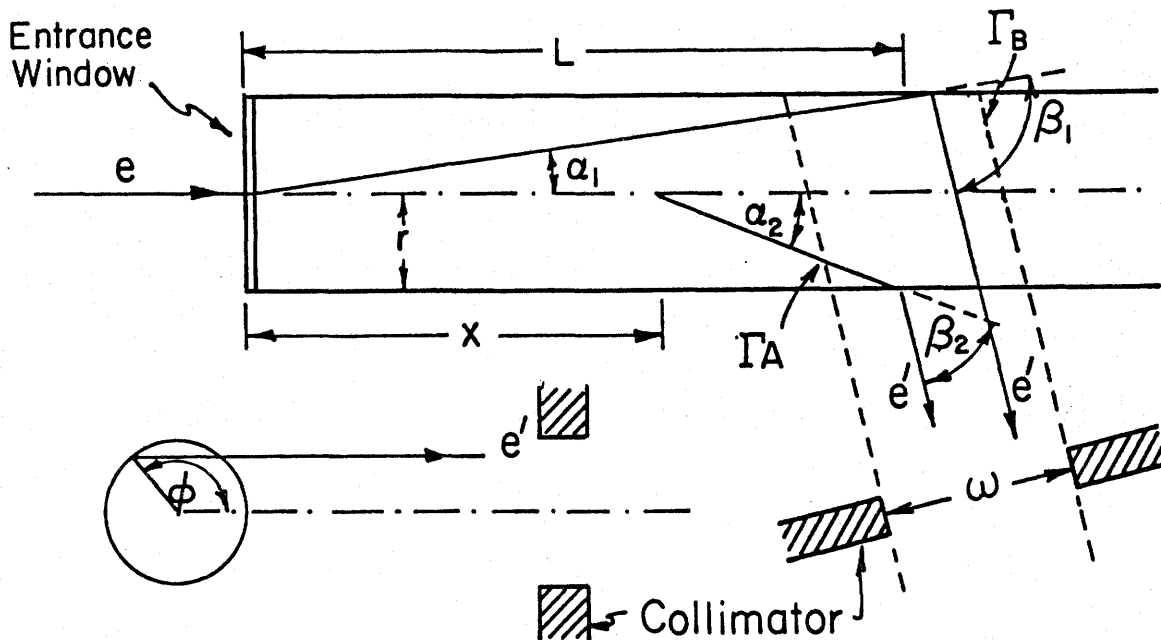


Figure A.1 Multiple Scattering from Target Cell

The contribution from the window-wall scattering events were determined by measuring spectra for an empty target cell under beam conditions similar to those under which the ^{17}O data were taken. The only difference between the empty target cell and the one used to contain the ^{17}O gas was that the entrance

window of the empty cell was twice as thick (0.002" vs. 0.001") as that of the one used to contain the gas. The spectra measured using the empty cell were not completely continuous. The spectra of the elastic peak regions were, but in the inelastic region the cross-section was measured at 4 to 5 MeV intervals and the continuous spectra obtained by fitting a polynomial:

$$Y(x) = a / x^2 + b / x + c + d x + e x^2 \quad (\text{A.1})$$

to the data.

Unfortunately, the contribution from gas-wall scattering events could not be similarly isolated. This contribution to the ^{17}O data had, therefore, to be calculated. The following procedure was adopted. First, for each set of beam conditions the window-wall scattering cross-section was computed. Then, a similar calculation was performed for a gas-filled cell (window-wall plus gas-wall scattering). The ratio between the two was then used to scale the empty cell spectrum to obtain the corresponding full-cell background spectrum.

A.2 Elastic Peak Background

Consider first the empty-cell scattering. A convenient coordinate system, centred at the point of the first scattering event with the \hat{z} -axis defined by the beam line and the \hat{x} -axis defined by the plane formed by the beam line and collimator centre, is shown in Figure A.2.

Since the acceptance angle of the spectrometer is small it was assumed that the point of scattering from the wall must lie within the rectangular column defined by the spectrometer axis and the collimator (see Figure A.1). The lines on the target cell surface which bound this region are given by:

$$\Gamma_A: \alpha_A(\varphi) = \cot^{-1} [\cos \varphi \cot \theta + L_A / r] ; L_A = L - \omega/2\sin\theta \quad (\text{A.2})$$

$$\Gamma_B: \alpha_B(\varphi) = \cot^{-1} [\cos \varphi \cot \theta + L_B / r] ; L_B = L + \omega/2\sin\theta \quad (\text{A.3})$$

where the symbols are defined in Figures A.1 and A.2.

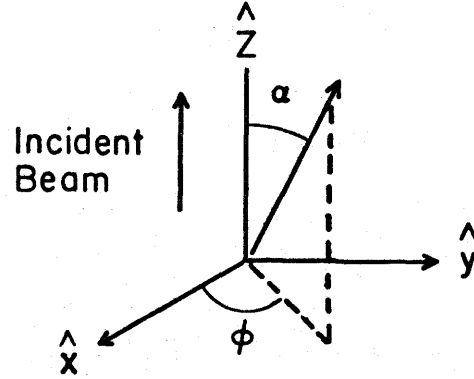


Figure A.2 Coordinate System for Multiple Scattering Description

Since the vertical extent of the collimator exceeds the diameter of the cell, the cross-section for the elastic scattering of electrons by the window onto that part of the wall that is 'seen' by the collimator is given by:

$$d\sigma_w \propto \int_{\varphi=0}^{2\pi} \int_{\alpha=\alpha_A(\varphi)}^{\alpha_B(\varphi)} z^2 \sigma_M |F_{ew}(q_\alpha)|^2 \sin \alpha \, d\alpha \, d\varphi \quad (\text{A.4})$$

where σ_M is the Mott cross-section (Equation 2.12), $|F_{ew}(q_\alpha)|^2$ is the elastic form factor for the window material, and q_α is the momentum transfer. Given the direction (α, φ) in which the electron is initially scattered, one can determine the angle at which it must be scattered during the second event:

$$\beta = \cos^{-1} [\sin \theta \cos \varphi \sin \alpha + \cos \alpha \cos \theta] \quad (\text{A.5})$$

The cross-section for the multiple scattering event thus becomes:

$$\sigma_{ew-sw} \propto \Delta\Omega \left(\frac{z_{ew} \alpha}{2\epsilon_1} \frac{z_{sw} \alpha}{2\epsilon_1} \right)^2 \int_{\varphi=0}^{2\pi} \int_{\alpha=\alpha_A(\varphi)}^{\alpha_B(\varphi)} A(\varphi) \frac{\cos^2(\alpha/2) \cos^2(\beta/2)}{\sin^4(\alpha/2) \sin^4(\beta/2)} |F_{ew}(q_\alpha)|^2 |F_{sw}(q_\beta)|^2 d\alpha d\varphi \quad (A.6)$$

where $\Delta\Omega$ is the spectrometer acceptance angle and the subscripts ew (sw) denote the entrance window (side wall).

The procedure for calculating the cross-section for gas-wall scattering follows immediately. In this case the range of α depends upon not only φ , but also x , where x is the distance from the entrance window of the point of first scatter. This dependence upon x appears in Equations A.2 and A.3 wherein:

$$L \rightarrow L - x$$

The cross-section thus becomes a cross-section with respect to x , and must be integrated from $x=0$ to $x=L-w/2\sin\theta$. The latter limit is the edge of the column defined by the collimator and spectrometer axis.

The integration cannot be carried to the latter limit exactly. As the point of first scatter approaches it the probability of the second scatter being to the required angle β may exceed 1. The point at which this first occurs was taken as the limit to the integration.

The cross-section for gas-wall scattering therefore becomes:

$$\sigma_{g-sw} \propto \Delta\Omega \left(\frac{z_g \alpha}{2\epsilon_1} \frac{z_{sw} \alpha}{2\epsilon_1} \right)^2 \int_{\varphi=0}^{2\pi} \int_{x=0}^{L-w/2\sin\theta-\zeta} \int_{\alpha=\alpha_A(\varphi,x)}^{\alpha_B(\varphi,x)} A(\varphi,x) \frac{\cos^2(\alpha/2) \cos^2(\beta/2)}{\sin^4(\alpha/2) \sin^4(\beta/2)} |F_g(q_\alpha)|^2 |F_{sw}(q_\beta)|^2 d\alpha d\varphi dx \quad (A.7)$$

where ζ denotes the amount by which the range of the x integration is shortened.

To obtain the elastic form factors for the entrance window and the wall, Fermi distributions of their nuclear charge densities were assumed. An approximate expression for the elastic form factor of a Fermi distribution is given by Verdie (68):

$$F(q) = \int_x \left[y^2 \frac{\sin x \cosh y}{\sinh^2 y} - \frac{x y \cos x}{\sinh y} \right] [1 + (\pi/s)^2]^{-1} \quad (\text{A.8})$$

where $x = qc$, $y = \pi qz$, $z = t/4 \ln 3$, $s = c/z$, c is the radius parameter, and t is the skin thickness parameter.

The elastic form factor of ^{17}O was assumed to equal that of ^{16}O (Singhal 70) and was calculated using a harmonic oscillator charge distribution with an oscillator parameter $b = 1.82$.

The ratios obtained between the cross-sections for the filled-cell multiple scattering and those for the empty-cell scattering are listed on the first line of Table A.1.

A.3 Inelastic Region Background

This problem was treated analogously to the case of the elastic peak region with one important exception. Since it is not immediately obvious that the radiation tail for scattering from an empty cell should have the same shape as that for scattering from a filled one, cross-sections for both the filled and empty cell cases were calculated for various final electron energies.

Two processes were assumed to contribute significantly. In the first, the electron scatters non-radiatively during the first event and radiatively during

Table A.1 Multiple Scattering Cross-Section Ratios
(Filled cell / Empty cell)

| Ex (MeV) | ϵ_1 (MeV) \rightarrow | 64.9 | 83.3 | 101.3 | 113.6 | 124.0 |
|----------|----------------------------------|------|------|-------|-------|-------|
| 0 | | 1.21 | 1.27 | 1.38 | 1.52 | 1.70 |
| 10 | | 1.19 | 1.27 | 1.38 | 1.52 | 1.70 |
| 15 | | 1.18 | | | | |
| 20 | | 1.18 | 1.26 | 1.38 | | |
| 25 | | 1.17 | | | | |
| 30 | | 1.17 | 1.26 | 1.37 | | |
| 40 | | | 1.26 | 1.37 | 1.50 | |

the second event. In the second process, the opposite occurs. Only hard Bremsstrahlung emission was considered. The cross-section for scattering to a final electron state of energy ϵ_2 is given, in the Peaking approximation, by:

$$\frac{d^2\sigma}{d\Omega d\epsilon_2} = \frac{\alpha}{\pi(\epsilon_0 - \epsilon_1)} \left[\left\{ \left(1 + \frac{\epsilon_1'^2}{\epsilon_1^2} \right) \ln \left(\frac{2\epsilon_1}{m_e} - \frac{\epsilon_1'}{\epsilon_1} \right) \frac{d\sigma(\epsilon_1')}{d\Omega} \left(\frac{\epsilon_0}{\epsilon_1} \frac{\epsilon_1'}{\epsilon_2} \right) + \left\{ \left(1 + \frac{\epsilon_2^2}{\epsilon_0^2} \right) \ln \left(\frac{2\epsilon_2}{m_e} - \frac{\epsilon_2}{\epsilon_0} \right) \frac{d\sigma(\epsilon_1)}{d\Omega} \right\} \right] \quad (\text{A.9})$$

where $d\sigma(\epsilon)/d\Omega$ is the cross-section for radiationless elastic scattering of electrons with energy ϵ , and the energies ϵ_0 , ϵ_1 , ϵ_2 , and ϵ_1' are defined in Figure A.3.

The ratios between the cross-sections for multiple scattering from the filled cell and that for scattering from the empty cell are listed in Table A.1.

Since the ratios for each spectrum remained constant, independent of excitation energy, the (fitted) empty cell spectra were simply scaled by a constant factor.

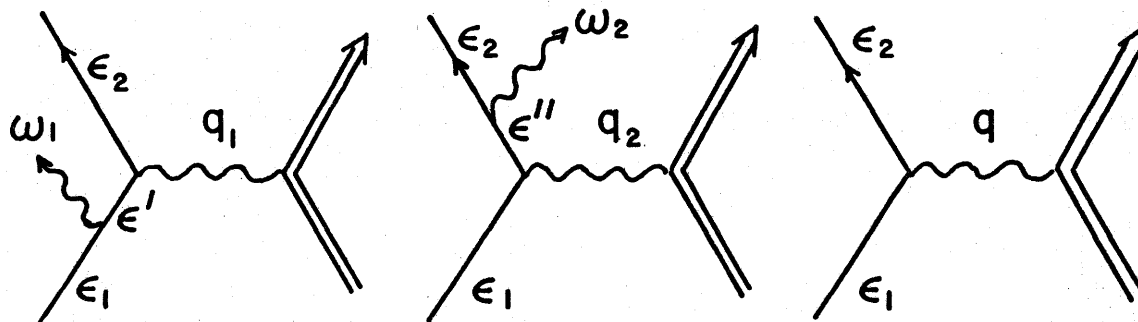


Figure A.3 Feynman Diagrams for Processes Contributing to Hard Bremsstrahlung Background

APPENDIX B

QUASI-ELASTIC SCATTERINGB.1 de Forest Theory

The bound state excitations predicted by the particle-hole model occur at excitation energies of less than 40 MeV. There is, however, considerable strength in the scattered electron spectrum at higher excitation energies, beyond that due to the radiation tail.

This strength was originally explained as arising from the electrons scattering elastically from one nucleon in the nucleus. The nucleon involved recoils with sufficient energy to put it into an unbound state with respect to the rest of the nucleus. The resulting theoretical scattered electron spectrum is smooth, with one broad peak. Experimentally, the peak is observed, indicating that the concept has some merit. However, the observed peak occurs at a higher excitation energy than predicted. This suggests that the theory should be modified to account for the effects of nuclear structure.

In deForest's model of this process (de Forest 69) the independent particle description of the nucleus is used. Only Pauli correlations are considered so that in the Born Approximation only one nucleon is excited. The final state of that nucleon is taken to be a plane wave. Two nuclear structure effects are included in this model. One is the binding energy of the excited nucleon. The other is the energy dependence of the nuclear potential. Since this dependence is not well understood, de Forest chose the form of the dependence to be linear.

Since this process involves a continuum, as opposed to a discrete, final state, the cross-section is a differential cross-section with respect to scat-

tered electron energy:

$$\frac{d^2\sigma}{d\Omega d\epsilon_2} = \sigma_M |f(q^2)|^2 m_N \left[\frac{q_L^4}{q^4} N^c(q,\omega) + \left\{ \frac{|q_L|^2}{2q^2} + \tan^2(\theta/2) \right\} N^t(q,\omega) \right] \quad (\text{B.1})$$

where $f(q^2)$ is the nucleon charge form factor, ω is the excitation energy, and $N^c(q,\omega)$ and $N^t(q,\omega)$ are the longitudinal and transverse differential form factors respectively. Since a nucleon from any shell can be excited by this process, the above form factors represent the summation of the form factors for the emission of a particle from any non-empty shell:

$$N^{c,t} = N_{Os}^{c,t} + N_{Op}^{c,t} + \dots \quad (\text{B.2})$$

Explicit calculations of $N_{Os}^{c,t}$ and $N_{Op}^{c,t}$ were carried out by de Forest, under the assumption that each shell was completely filled. The results for the longitudinal form factors are:

$$N_{Os}^c = \left\{ 1 - \frac{q^2(2\mu_p - 1)}{4m_N^2} \right\} \frac{2b}{q\sqrt{\pi}} \left\{ (e^{-b^2 p_-^2}) - (e^{-b^2 p_+^2}) \right\} P^2 \quad (\text{B.3})$$

and

$$N_{Op}^c = \left\{ 1 - \frac{q^2(2\mu_p - 1)}{4m_N^2} \right\} \frac{4b}{q\sqrt{\pi}} \left\{ (1+b^2 p_-^2) (e^{-b^2 p_-^2}) - (1+b^2 p_+^2) (e^{-b^2 p_+^2}) \right\} P^2 \quad (\text{B.4})$$

where b is the oscillator parameter, $p_{\pm} = p_0 \pm q$, with

$$p_0 = \sqrt{\frac{2m_N}{m_N b^2} \frac{C}{m_N b^2} + \omega \frac{E_0 - C/m_N b^2}{E_0 + S.E.}},$$

$$C = \begin{cases} \frac{1}{2} & \text{for the Os shell} \\ 1 & \text{for the Op shell} \end{cases} ,$$

$$P^2 = \frac{E_0 - C/m_N b^2}{E_0 + \text{S.E.}} ,$$

μ_p is the magnetic moment of the proton, S.E. is the separation energy for a nucleon, and E_0 is a free parameter taken to be about 100 MeV.

Due to the assumed lack of spin dependence of the wavefunctions, there is no interference between the magnetic moment and current contributions to the transverse form factors:

$$N^t = N^\mu + N^j \quad (\text{B.5})$$

For the case of filled Os and Op shells we have:

$$N_{s,p}^\mu = \frac{(\mu_p + \mu_n)^2}{1 - \frac{q^2(2\mu_p - 1)}{4m_N^2}} \frac{q^2}{2m_N^2} N_{s,p}^c \quad (\text{B.6})$$

$$N_{Os}^j = \frac{4b}{q\sqrt{\pi}} \frac{p_0^2}{m_N^2} \alpha [(1-\alpha) (e^{-b^2 p_-^2}) + (1+\alpha) (e^{-b^2 p_+^2})] P^2 \quad (\text{B.7})$$

$$N_{Op}^j = \frac{8b}{q\sqrt{\pi}} \frac{p_0^2}{m_N^2} \alpha [\{ (2-3\alpha) + (1-\alpha) b^2 p_-^2 \} (e^{-b^2 p_-^2}) + \{ (2+3\alpha) + (1+\alpha) b^2 p_+^2 \} (e^{-b^2 p_+^2})] P^2 \quad (\text{B.8})$$

where $\alpha = (2b^2 p_0 q)^{-1}$.

To apply the de Forest theory to ¹⁷O one must either compute the contri-

bution from the $0d_{5/2}$ neutron or justify omitting it, thereby treating ^{17}O as equivalent to ^{16}O . In this work the latter course was deemed the most reasonable, for reasons discussed below.

The de Forest theory was used only to predict the asymptotic behavior of the scattered electron spectra as the excitation energy became large (> 50 MeV). Therefore, only those processes which would contribute significantly in this range ~~needed~~ to be included. The contribution to the scattered electron spectrum due to the ejection of a nucleon from a particular shell forms a broad peak centred a few MeV above the nucleon's emission threshold. The peak has a rapidly dying tail on the high excitation side. It follows that the spectrum in the high excitation region should be primarily due to the tails of the higher energy peaks.

The neutron emission threshold in ^{17}O lies at 4.14 MeV excitation (Ajzenberg-Selove 71), whereas that for a proton lies at 13.8 MeV. From this one may conclude that the threshold for emission of a nucleon from the $0d_{5/2}$ shell is about 4 MeV while that for the emission of a $0p$ shell nucleon is of the order of 14 MeV. The threshold for the emission of a $0s$ shell nucleon would undoubtedly be much higher. This indicates that the $0p$ and $0s$ shell nucleons should play a dominant role. Furthermore, there are eight $0p$ and four $0s$ shell nucleons as opposed to only one nucleon in the $0d_{5/2}$ shell, lending additional credence to the belief that the latter shell may be omitted.

In view of the above considerations it was felt that to omit the contribution of the $0d_{5/2}$ neutron would not deal a fatal blow to the accuracy of the calculation.

APPENDIX C

BOEKER-BRINK INTERACTION MATRIX ELEMENTS

The matrix elements of a two-body interaction are defined by:

$$\text{M.E.} = {}_a \langle \alpha_1 \alpha_2; JM_J TM_T | \hat{V}(1,2) | \alpha_3 \alpha_4; J'M_J T'M_T \rangle_a$$

where $\alpha_i = (n_i, l_i, j_i)$, \hat{V} is the two-body interaction operator, and the subscript a denotes antisymmetrization in accordance with the Pauli Principle.

The first step in the evaluation of the two-body matrix elements is the construction of the orthonormal, antisymmetrized two-body wavefunctions in terms of the single-particle wavefunctions:

$$\varphi_{\alpha}^{m_j m_\tau}(\vec{r}) = \sum_{m_s} (l m_l s m_s | j m_j) \chi_{m_s}^s \chi_{m_\tau}^\tau R_{nl}(r) Y_{l1}^{m_l}(\hat{r})$$

(see Section IV.2.1). The bare (i.e., not antisymmetrized) two-body wavefunction is given by:

$$\begin{aligned} \psi_{\alpha_1 \alpha_2}^{JM_J TM_T}(\vec{r}_1, \vec{r}_2) &= \sum_{\substack{m_{j1} m_{\tau 1} \\ m_{j2} m_{\tau 2}}} (j_1 m_{j1} j_2 m_{j2} | J M_J) (\tau_1 m_{\tau 1} \tau_2 m_{\tau 2} | T M_T) \\ &\quad \times \varphi_{\alpha_1}^{m_{j1} m_{\tau 1}}(\vec{r}_1) \varphi_{\alpha_2}^{m_{j2} m_{\tau 2}}(\vec{r}_2) \\ &= \langle \vec{r}_1, \vec{r}_2 | \alpha_1 \alpha_2; JM_J TM_T \rangle \end{aligned} \quad (\text{C.1})$$

Inverting the positions of the particles yields:

$$\begin{aligned} \psi_{\alpha_1 \alpha_2}^{JM_J TM_T}(\vec{r}_2, \vec{r}_1) &= \langle \vec{r}_2, \vec{r}_1 | \alpha_1 \alpha_2; JM_J TM_T \rangle \\ &= (-1)^{j_1 + j_2 - J + 1 - T} \langle \vec{r}_1, \vec{r}_2 | \alpha_2 \alpha_1; JM_J TM_T \rangle \end{aligned} \quad (\text{C.2})$$

Subtracting (C.2) from (C.1) yields the antisymmetrized wavefunction:

$$\begin{aligned}
 | \alpha_1, \alpha_2; JM_J TM_T \rangle_a = N [& | \alpha_1, \alpha_2; JM_J TM_T \rangle \\
 & + (-1)^{j_1 + j_2 - J + 1 - T} | \alpha_2, \alpha_1; JM_J TM_T \rangle] \quad (C.3)
 \end{aligned}$$

where N is an undetermined normalization constant.

The single-particle wavefunctions are orthonormal by construction. Similarly, the unitary properties of the Clebsch-Gordon coefficients ensure that the bare two-particle wavefunctions are also orthonormal. Thus, the antisymmetrized wavefunctions (C.3) are orthogonal, but their normalization depends upon N.

Squaring the wavefunction and equating to zero yields:

$$1 = |N|^2 [1 - (-1)^{J+T} \delta_{\alpha_1 \alpha_2}] \times 2. \quad (C.4)$$

This defines N to within an arbitrary phase which will be taken to be +1:

$$N = [2 \{1 - (-1)^{J+T} \delta_{\alpha_1 \alpha_2}\}]^{-\frac{1}{2}}. \quad (C.5)$$

The required matrix elements may now be written:

$$\begin{aligned}
 \text{M.E.} = N_b N_k [& \langle \alpha_1, \alpha_2; JM_J TM_T | + (-1)^{j_1 + j_2 - J - T} \langle \alpha_2, \alpha_1; JM_J TM_T |] \hat{V} \\
 & [\langle \alpha_3, \alpha_4; JM'_J TM'_T | + (-1)^{j_1 + j_2 - J - T} \langle \alpha_4, \alpha_3; JM'_J TM'_T |] \quad (C.6)
 \end{aligned}$$

where $N_b(N_k)$ is the normalization constant for the bra (ket). Since \hat{V} is a scalar in configuration, spin, and isospin spaces, $J=J'$, $M_J=M'_J$, $T=T'$, and $M_T=M'_T$. Also, since it does not depend upon T, M_J , or M_T , these labels may be suppressed with no loss of generality. The M.E. can thus be written:

$$\begin{aligned}
\text{M.E.} = N_b N_k [& \langle 1,2;J|\hat{V}|3,4;J \rangle + (-1)^{j_1+j_2+j_3+j_4} \langle 2,1;J|\hat{V}|4,3;J \rangle \\
& + (-1)^{j_1+j_2-J-T} \langle 1,2;J|\hat{V}|4,3;J \rangle \\
& + (-1)^{j_3+j_4-J-T} \langle 2,1;J|\hat{V}|3,4;J \rangle] \quad (\text{C.7})
\end{aligned}$$

where the α labels have been dropped, and only their subscripts retained. This expression may be simplified as follows:

$$\begin{aligned}
& \langle 2,1;J|\hat{V}|4,3;J \rangle \\
& = \int d^3 r_1 \int d^3 r_2 \langle 2,1;J|\vec{r}_1, \vec{r}_2 \rangle V(|\vec{r}_1 - \vec{r}_2|) \langle \vec{r}_1, \vec{r}_2|4,3;J \rangle .
\end{aligned} \quad (\text{C.8})$$

Since \hat{V} is symmetric under interchange of arguments, we can apply the symmetry relation of Equation C.2 to get:

$$\langle 2,1;J|\hat{V}|4,3;J \rangle = (-1)^{j_1+j_2+j_3+j_4} \langle 1,2;J|\hat{V}|3,4;J \rangle \quad (\text{C.9})$$

Similarly:

$$\langle 2,1;J|\hat{V}|3,4;J \rangle = (-1)^{j_1+j_2+j_3+j_4} \langle 1,2;J|\hat{V}|4,3;J \rangle \quad (\text{C.10})$$

Equation (C.7) therefore becomes:

$$\text{M.E.} = 2N_b N_k [\langle 1,2;J|\hat{V}|3,4;J \rangle + (-1)^{j_1+j_2-J-T} \langle 1,2;J|\hat{V}|4,3;J \rangle] \quad (\text{C.11})$$

Two characteristics of the Boeker-Brink interaction must be noted before proceeding. First, the operator acts upon only the spatial parts of the wave-

functions. The spin and isospin dependence of the matrix elements is contained in the geometric factors. Second, the interaction is a function of only the relative separation of the two particles. That is, it does not depend upon the position of either point with respect to an external point.

The first characteristic is exploited by converting from j-j to L-S coupling. This is achieved using the LS-jj Transformation Brackets (Kennedy 55) which are related to the more common Wigner 9-J symbol (Edmonds 58) by:

$$A \begin{pmatrix} l_1 & s_1 & j_1 \\ l_2 & s_2 & j_2 \\ L & S & J \end{pmatrix} = \sqrt{(2L+1)(2S+1)(2j_1+1)(2j_2+1)} \begin{Bmatrix} l_1 & s_1 & j_1 \\ l_2 & s_2 & j_2 \\ L & S & J \end{Bmatrix} \quad (C.12)$$

The bare two-body wavefunctions thus become:

$$|1,2;J\rangle = \sum_{L,S} A \begin{pmatrix} l_1 & s_1 & j_1 \\ l_2 & s_2 & j_2 \\ L & S & J \end{pmatrix} |n_1 n_2, \{(l_1 l_2)L, (s_1 s_2)S\}; J\rangle \quad (C.13)$$

and $\langle 1,2;J | \hat{V} | 3,4;J \rangle =$

$$\sum_{L,S} A \begin{pmatrix} l_1 & s_1 & j_1 \\ l_2 & s_2 & j_2 \\ L & S & J \end{pmatrix} A \begin{pmatrix} l_3 & s_3 & j_3 \\ l_4 & s_4 & j_4 \\ L & S & J \end{pmatrix} \times \langle n_1 n_2, (l_1 l_2)L; J | \hat{V} | n_3 n_4, (l_3 l_4)L; J \rangle \quad (C.14)$$

The second characteristic is utilized by applying the Moshinsky Transformation (Moshinsky 67) to the wavefunctions. In coordinate space this corresponds to the replacement:

$$(\vec{r}_1, \vec{r}_2) \rightarrow (\vec{r}, \vec{R}) = \left(\frac{\vec{r}_1 - \vec{r}_2}{\sqrt{2}}, \frac{\vec{r}_1 + \vec{r}_2}{\sqrt{2}} \right). \quad (C.15)$$

In this system, the two-body wavefunction formed by the coupling of two single-particle harmonic oscillator wavefunctions is expressed in terms of the coupling of 'relative state' wavefunctions and 'centre of mass' wavefunctions. The beauty of the technique is that the relative and centre of mass wavefunctions are also harmonic oscillator wavefunctions with the same oscillator parameter as the single-particle wavefunctions.

The bare wavefunction thus becomes:

$$|1,2;J\rangle = \sum_{L,S} A \begin{pmatrix} l_1 & s_1 & j_1 \\ l_2 & s_2 & j_2 \\ L & S & J \end{pmatrix} \sum_{\substack{N,\zeta \\ n,l}} \langle n1,N\zeta;L | n_1 l_1, n_2 l_2;L \rangle |nN,(l\zeta)L;J\rangle \quad (\text{C.16})$$

where N, ζ refer to the centre of mass wavefunction, and n, l refer to the relative state wavefunction, and:

$$(-1)^{l_1+l_2} = (-1)^{l+\zeta}, \quad (\text{C.17})$$

since the parity of the state is independent of the representation. The matrix element between bare wavefunctions becomes:

$$\begin{aligned} \langle 1,2;J | \hat{V} | 3,4;J \rangle &= \sum_{L,S} A \begin{pmatrix} l_1 & s_1 & j_1 \\ l_2 & s_2 & j_2 \\ L & S & J \end{pmatrix} A \begin{pmatrix} l_3 & s_3 & j_3 \\ l_4 & s_4 & j_4 \\ L & S & J \end{pmatrix} \\ &\times \sum_{\substack{N,\zeta \\ n,l}} \sum_{\substack{N',\zeta' \\ n',l'}} \langle n1,N\zeta;L | n_1 l_1, n_2 l_2;L \rangle \langle n'1',N'\zeta';L | n_3 l_3, n_4 l_4;L \rangle \\ &\times \langle nN,(l\zeta)L;J | \hat{V} | n'N',(l'\zeta')L;J \rangle \quad (\text{C.18}) \end{aligned}$$

Since \hat{V} is a function of the relative coordinate alone it cannot affect the centre of mass wavefunction. Therefore, $N = N'$ and $\zeta = \zeta'$. Now, only the

(n,l) and (n',l') labels need be retained. Since \hat{V} is a scalar operator in configuration space it cannot connect states of different relative angular momentum. Therefore, $l = l'$. Incorporating these simplifications yields the following form for the matrix element between two antisymmetrized wavefunctions:

$$\begin{aligned}
a\langle 1,2;J,T|\hat{V}|3,4;J,T\rangle_a &= \sum_{L,S} A \begin{pmatrix} l_1 & s_1 & j_1 \\ l_2 & s_2 & j_2 \\ L & S & J \end{pmatrix} A \begin{pmatrix} l_3 & s_3 & j_3 \\ l_4 & s_4 & j_4 \\ L & S & J \end{pmatrix} \\
&\times \sum_{\substack{N,\zeta \\ n,n',l}} \langle n l, N\zeta; L | n_1 l_1, n_2 l_2; L \rangle \langle n' l, N\zeta; L | n_3 l_3, n_4 l_4; L \rangle \langle n l | \hat{V} | n' l \rangle \\
&+ (-1)^{j_3+j_4-J-T} \sum_{L,S} A \begin{pmatrix} l_1 & s_1 & j_1 \\ l_2 & s_2 & j_2 \\ L & S & J \end{pmatrix} A \begin{pmatrix} l_4 & s_4 & j_4 \\ l_3 & s_3 & j_3 \\ L & S & J \end{pmatrix} \\
&\times \sum_{\substack{N,\zeta \\ n,n',l}} \langle n l, N\zeta; L | n_1 l_1, n_2 l_2; L \rangle \langle n' l, N\zeta; L | n_4 l_4, n_3 l_3; L \rangle \langle n l | \hat{V} | n' l \rangle
\end{aligned} \tag{C.19}$$

Using the symmetry properties of the Moshinsky Brackets:

$$\langle n l, N\zeta; L | n_1 l_1, n_2 l_2; L \rangle = (-1)^{\zeta-L} \langle n l, N\zeta; L | n_2 l_2, n_1 l_1; L \rangle \tag{C.20}$$

and those of the LS-jj Transformation Brackets:

$$A \begin{pmatrix} l_1 & s_1 & j_1 \\ l_2 & s_2 & j_2 \\ L & S & J \end{pmatrix} = (-1)^{l_1+l_2+L+s_1+s_2+S+j_1+j_2+J} A \begin{pmatrix} l_2 & s_2 & j_2 \\ l_1 & s_1 & j_1 \\ L & S & J \end{pmatrix} \tag{C.21}$$

Equation C.19 can be rewritten as:

$$a \langle 1,2;JT | \hat{V} | 3,4;JT \rangle = \sum_{L,S} A \begin{pmatrix} l_1 & s_1 & j_1 \\ l_2 & s_2 & j_2 \\ L & S & J \end{pmatrix} A \begin{pmatrix} l_3 & s_3 & j_3 \\ l_4 & s_4 & j_4 \\ L & S & J \end{pmatrix} \sum_{N,\zeta} [1 - (-1)^{l+S+T}] \sum_{n,n',l} N, \zeta, n, n', l$$

$$\times \langle n'l, N\zeta; L | n_1 l_1, n_2 l_2; L \rangle \langle n'l, N'\zeta; L | n_3 l_3, n_4 l_4; L \rangle \langle n'l | \hat{V} | n'l \rangle .$$

(C.22)

The only step remaining is the calculation of the 'relative matrix elements':

$$\text{RME} = \langle n'l | \hat{V} | n'l \rangle$$

$$= \langle n'l | [S_1 (1 - m_1 + m_1 \hat{P}_M) e^{-2r^2/\mu_1^2} + S_2 (1 - m_2 + m_2 \hat{P}_M) e^{-2r^2/\mu_2^2}] | n'l \rangle .$$

(C.23)

The action of the Majorana exchange operator on a state of relative angular momentum l is:

$$\hat{P}_M | n'l \rangle = (-1)^l | n'l \rangle . \quad (\text{C.24})$$

$$\begin{aligned} \text{Thus: } \text{RME} &= S_1 \langle n'l | e^{-2r^2/\mu_1^2} | n'l \rangle + S_2 \langle n'l | e^{-2r^2/\mu_2^2} | n'l \rangle ; \text{ if } (-1)^l = 1 \\ &= S_1 (1 - 2m_1) \langle n'l | e^{-2r^2/\mu_1^2} | n'l \rangle + S_2 (1 - 2m_2) \langle n'l | e^{-2r^2/\mu_2^2} | n'l \rangle ; \end{aligned}$$

$$\text{if } (-1)^l = -1$$

(C.25)

It has been shown (Moshinsky 58) that matrix elements of the form $\langle n'l | v(r) | n'l \rangle$ can be expanded in terms of the Talmi integrals (Talmi 52):

$$\langle n'l | v(r) | n'l' \rangle = \sum_p B(n'l, n'l'; p) I_p, \quad (C.26)$$

where

$$I_p = \frac{2}{\Gamma(p+3/2)} \int_0^\infty x^{2p} e^{-x^2} v(x) x^2 dx \quad ; \quad x = r/b,$$

b is the oscillator parameter and $B(n'l, n'l'; p)$ is a Moshinsky B-coefficient.

In the case in question, the Talmi integrals can be evaluated in closed form:

$$\begin{aligned} I_p &= \frac{2}{\Gamma(p+3/2)} \int_0^\infty e^{-x^2} e^{-2x^2 b^2/\mu^2} x^{2p+2} dx \\ &= \left(1 + \frac{2b^2}{\mu^2} \right)^{-(p+3/2)}. \end{aligned} \quad (C.27)$$

Therefore:

$$\begin{aligned} \langle n'l | \hat{V} | n'l' \rangle &= \sum_p B(n'l, n'l'; p) \left[S_1 \left(\frac{1+2b^2}{\mu_1^2} \right)^{-(p+3/2)} + S_2 \left(\frac{1+2b^2}{\mu_2^2} \right)^{-(p+3/2)} \right]; \\ &\quad \text{if } (-1)^l = 1, \\ &= \sum_p B(n'l, n'l'; p) \left[S_1 (1-2m_1) \left(\frac{1+2b^2}{\mu_1^2} \right)^{-(p+3/2)} \right. \\ &\quad \left. + S_2 (1-2m_2) \left(\frac{1+2b^2}{\mu_2^2} \right)^{-(p+3/2)} \right]; \text{ if } (-1)^l = -1. \end{aligned} \quad (C.28)$$

The two-body matrix elements were computed using Equations C.22, C.27 and C.28.

APPENDIX D

SINGLE-PARTICLE MATRIX ELEMENTS

The charge, current and magnetization densities are taken to be those of a point particle:

$$\hat{\rho}_N(\vec{x}) = \delta(\vec{r}_i - \vec{x}) \hat{e}_i, \quad (\text{D.1})$$

$$\hat{j}_N(\vec{x}) = \delta(\vec{r}_i - \vec{x}) \hat{e}_i \frac{(-i)}{m_N} \nabla_i, \quad (\text{D.2})$$

$$\hat{\mu}_N(\vec{x}) = \delta(\vec{r}_i - \vec{x}) \hat{\mu}_i \frac{\vec{\sigma}(i)}{2m_N}, \quad (\text{D.3})$$

where $\hat{e}_i = \frac{1}{2} + \hat{\tau}_3(i)/2$ is the charge operator for the i^{th} particle, $\hat{\mu}_i = (\mu_p + \mu_n)/2 + (\mu_p - \mu_n)/2 \hat{\tau}_3(i)$ is the magnetic moment operator for the i^{th} particle, and $\vec{\sigma}(i)$ is the spin of the i^{th} particle.

The operators \hat{M} and $\hat{\vec{M}}$ are defined by:

$$\hat{M}_J^M(\vec{x}) = j_J(qx) Y_J^M(\hat{x}) \quad (\text{D.4})$$

$$\hat{\vec{M}}_{JL}^M(\vec{x}) = j_J(qx) \vec{Y}_{JL1}^M(\hat{x}) \quad (\text{D.5})$$

where j_J is a spherical Bessel function, Y_J^M is a spherical harmonic, and \vec{Y}_{JL1}^M is a vector spherical harmonic. In terms of these operators, $\hat{M}_{JM}^C(q)$, $\hat{T}_{JM}^{EL}(q)$, and $\hat{T}_{JM}^{\text{Mag}}(q)$ take the forms:

$$\hat{M}_{JM}^C(q) = \hat{e}_i \hat{M}_J^M(\vec{r}_i), \quad (\text{D.6})$$

$$\hat{T}_{JM}^{EL}(q) = \frac{q}{m_N} \left[\left\{ -\sqrt{\frac{J}{2J+1}} \hat{\vec{M}}_{JJ+1}^M(\vec{r}_i) + \sqrt{\frac{J+1}{2J+1}} \hat{\vec{M}}_{JJ-1}^M(\vec{r}_i) \right\} \cdot \hat{e}_i \nabla_i \right] \frac{1}{q}$$

$$+ \hat{M}_{JJ}^M(\vec{r}_i) \cdot \hat{\mu}_i \vec{\sigma}(i) \quad (D.7)$$

$$\hat{T}_{JM}^{\text{Mag}}(q) = \frac{iq}{m_N} \left[\left\{ -\frac{j}{\sqrt{2J+1}} \hat{M}_{JJ+1}^M(\vec{r}_i) + \frac{J+1}{\sqrt{2J+1}} \hat{M}_{JJ-1}^M(\vec{r}_i) \right\} \cdot \frac{\hat{\mu}_i}{2} \vec{\sigma}(i) \right. \\ \left. + \hat{M}_{JJ}^M(\vec{r}_i) \cdot \frac{\hat{e}_i}{2} \nabla_i \right] \quad (D.8)$$

To obtain the desired reduced matrix elements of the \hat{M}_{JM}^C , \hat{T}_{JM}^{El} , and $\hat{T}_{JM}^{\text{Mag}}$ operators the RME's of the operators on the right hand sides of the above equations are evaluated:

$$\langle n'(1'\frac{1}{2})j' || \hat{M}_J(\vec{r}) || n(1\frac{1}{2})j \rangle = \\ (-1)^{j+J-\frac{1}{2}} \sqrt{\frac{(2l'+1)(2l+1)(2L+1)(2j'+1)(2j+1)(2J+1)}{4\pi}} \\ \times \begin{Bmatrix} 1' & j' & \frac{1}{2} \\ j & 1 & J \end{Bmatrix} \begin{pmatrix} 1' & J & 1 \\ 0 & 0 & 0 \end{pmatrix} \langle n'1' | j_J(qr) | n1 \rangle \quad (D.9)$$

$$\langle n'(1'\frac{1}{2})j' || \hat{M}_{JL}(\vec{r}) \cdot \vec{\sigma} || n(1\frac{1}{2})j \rangle = \\ (-1)^{l'} \sqrt{\frac{6(2l'+1)(2l+1)(2L+1)(2j'+1)(2j+1)(2J+1)}{4\pi}} \\ \times \begin{Bmatrix} 1' & 1 & L \\ \frac{1}{2} & \frac{1}{2} & 1 \\ j' & j & J \end{Bmatrix} \begin{pmatrix} 1' & L & 1 \\ 0 & 0 & 0 \end{pmatrix} \langle n'1' | j_L(qr) | n1 \rangle \quad (D.10)$$

$$\langle n'(1'\frac{1}{2})j' || \hat{M}_{JL}(\vec{r}) \cdot \nabla || n(1\frac{1}{2})j \rangle =$$

$$\begin{aligned}
& (-1)^{l'+j-\frac{1}{2}} \sqrt{\frac{(2l'+1)(2l+1)(2L+1)(2j'+1)(2j+1)(2J+1)}{4\pi}} \\
& \times \left\{ \begin{matrix} l' & j' & \frac{1}{2} \\ j & l & J \end{matrix} \right\} \left[\left\{ \begin{matrix} L & 1 & J \\ 1 & l' & l+1 \end{matrix} \right\} \frac{\begin{pmatrix} l' & L & l+1 \\ 0 & 0 & 0 \end{pmatrix}}{\begin{pmatrix} 1+1 & 1 & 1 \\ 0 & 0 & 0 \end{pmatrix}} \frac{l+1}{2l+1} \right. \\
& \times \langle n'l' | j_L(qr) \left(\frac{d}{dr} - \frac{1}{r} \right) | nl \rangle \\
& \left. + \left\{ \begin{matrix} L & 1 & J \\ 1 & l' & l-1 \end{matrix} \right\} \frac{\begin{pmatrix} l' & L & l-1 \\ 0 & 0 & 0 \end{pmatrix}}{\begin{pmatrix} 1-1 & 1 & 1 \\ 0 & 0 & 0 \end{pmatrix}} \frac{1}{2l+1} \langle n'l' | j_L(qr) \left(\frac{d}{dr} + \frac{l+1}{r} \right) | nl \rangle \right] \quad (D.11)
\end{aligned}$$

where $\langle n'l' | j_L(qr) | nl \rangle = \int_0^\infty R_{n'l'}^*(r) j_L(qr) R_{nl}(r) r^2 dr$,

$(:::)$ is a 3-j symbol, $\{:::\}$ is a 6-j symbol, and $\{:::\}$ is a 9-j symbol.

The remaining symbols have been previously defined.

The radial matrix elements $\langle n'l' | f(r) | nl \rangle$ in Equation B.11 can be reduced using the following recursion relations:

$$\left(\frac{d}{dr} + \frac{l+1}{r} \right) R_{nl} = \frac{1}{b} (l+n-\frac{1}{2})^{\frac{1}{2}} R_{nl-1} + \frac{\sqrt{n}}{b} R_{n+1, l-1} \quad (D.12)$$

$$\left(\frac{d}{dr} - \frac{l}{r} \right) R_{nl} = \left(\frac{d}{dr} + \frac{l+1}{r} \right) R_{nl} - \sqrt{\frac{n+l-\frac{1}{2}}{n-1}} \frac{1}{r} R_{n-1, l} \quad (D.13)$$

$$\frac{1}{r} R_{nl} = \frac{-R_{n-1, l+1}}{b(n-1)^{\frac{1}{2}}} + \sqrt{\frac{n+l-\frac{1}{2}}{n-1}} \frac{1}{r} R_{n-1, l} \quad (D.14)$$

$$\frac{1}{r} R_{11} = \frac{R_{1L-1}}{b(1+\frac{1}{2})^{\frac{1}{2}}} \quad (\text{D.15})$$

The radial matrix elements of the Bessel functions can be evaluated analytically in terms of confluent hypergeometric (F) and gamma (Γ) functions.

These matrix elements are used to construct the partial form factors:

$$|F^{\text{CL}}|^2 = \frac{4\pi}{z^2 (2J_i+1)} \frac{q_{\mu}^4}{q^4} |\langle J_f | \hat{M}_L^{\text{C}}(q) | J_i \rangle|^2 \quad (\text{D.16})$$

and

$$|F^{\text{EL,ML}}|^2 = \frac{4\pi}{z^2 (2J_i+1)} |\langle J_f | \hat{T}_L^{\text{EL,Mag}}(q) | J_i \rangle|^2 \quad (\text{D.17})$$

which contribute to the total form factor:

$$\begin{aligned} F^2 &= |F_L|^2 + \left\{ \frac{q^2}{2q_{\mu}^2} + \tan^2(\theta/2) \right\} |F_T|^2 \\ &= \sum_{L=0}^{\infty} |F^{\text{CL}}|^2 + \left\{ \frac{q^2}{2q^2} + \tan^2(\theta/2) \right\} \sum_{L=1}^{\infty} [|F^{\text{EL}}|^2 + |F^{\text{ML}}|^2] \quad (\text{D.18}) \end{aligned}$$

A level whose total form factor F^2 is dominated by the contribution from $|F^{\text{CL}}|^2$ ($|F^{\text{EL}}, F^{\text{ML}}|^2$) is called a CL (EL,ML) level.

APPENDIX E

HELM MODEL

In the Helm model (Helm 56, Rosen 67) the transition charge density $\rho_t(\vec{r})$ for a Coulomb excitation is assumed to be concentrated on a shell about the nuclear radius. It takes the form of a δ -function smeared out by a convolution:

$$\rho_t(\vec{r}) = \int \rho_0(\vec{r}-\vec{r}') \rho_1(\vec{r}') d^3r' \quad (\text{E.1})$$

where the charged shell ρ_0 is given by:

$$\rho_0(\vec{r}) = z \delta(r-R) \quad (\text{E.2})$$

and R is the nuclear radius. The smearing function is assumed to take the form:

$$\rho_1(\vec{r}) = (2\pi g^2)^{-3/2} e^{-r^2/2g^2} \quad (\text{E.3})$$

where g is a measure of the surface thickness. The Fourier transform of ρ_t is therefore:

$$\begin{aligned} F(\vec{q}) &= \int d^3r e^{i\vec{q}\cdot\vec{r}} \rho_t(\vec{r}) \\ &= z e^{i\vec{q}\cdot\vec{R}} e^{-g^2 q^2/2} \end{aligned} \quad (\text{E.4})$$

The Coulomb matrix element is therefore given by:

$$\begin{aligned} \hat{M}_{LM}(q) &= \frac{1}{4\pi i^L} \int F(\vec{q}) Y_{LM}(\hat{q}) d\hat{q} \\ &= z e^{-g^2 q^2/2} j_L(qR) Y_{LM}(\hat{q}) \end{aligned} \quad (\text{E.5})$$

where j_L is a spherical Bessel function and Y_{LM} is a spherical harmonic.

This gives for the reduced matrix element:

$$\langle J_f || M_J^C(q) || J_i \rangle = (2J_i + 1)^{-\frac{1}{2}} \beta_{L i J_f}^{J_i J_f} e^{-g^2 q^2 / 2} j_L(qR) \quad (\text{E.6})$$

where $\beta_{L i J_f}^{J_i J_f}$ is a scale factor determined by experiment.

BIBLIOGRAPHY

- Ajzenberg-Selove, F., Nucl. Phys. A166 (1971) 1.
- Albert, D., Thesis, Catholic University of America, Washington, D.C., 1969.
- Ambler, E., Fuller, E., and Marshak, P., Phys. Rev. 138 (1965) B117.
- Auer, I., Caplan, H., Hough, J., Bergstrom, J., Kline, F., Hicks, R.,
Nucl. Instr. and Meth. 125 (1975) 257.
- Baldwin, G. and Klaiber, G., Phys. Rev. 73 (1948) 1156.
- Barber, W. in M.I.T. 1967 Summer Study, M.I.T. Rep. TID-24667, p.212, Lab. for
Nucl. Sci., M.I.T., Cambridge, Mass., U.S.A., 1967.
- Bergstrom, J., in M.I.T. 1967 Summer Study, M.I.T. Rep. TID-24667, p. 251,
Lab. for Nucl. Sci., M.I.T., Cambridge, Mass., U.S.A., 1967.
- Bishop, G., Phys. Lett. 17 (1965) 311.
- Bjorken, J., 1960, Unpublished.
- Bjorken, J. and Drell, S., Relativistic Quantum Mechanics, McGraw-Hill Book Co.,
N.Y.), 1964.
- Bohr, A. and Mottelson, B., Kgl. Dan. Vidensk. Selsk. Mat.-Fys. Medd. 27, No. 16
(1953).
- Boreli, Fizika (Yugoslavia) 2 (1970) 97.
- Brink, D., Nucl. Phys. 4 (1957) 215.
- Brink, D. and Boeker, E., Nucl. Phys. A91 (1967) 1.
- Brody, T. and Moshinsky, M., Tables of Transformation Brackets, Gordon and Breach
Science Publishers, N. Y., 1967.
- Brown, G. and Bolsterli, M., Phys. Rev. Lett. 3 (1959) 472.
- Danos, M., University of Maryland Technical Report 221 (1961), Unpublished.
- de Forest, T., Nucl. Phys. A132 (1969) 305.

- de Forest, T. and Walecka, J., Advan. Phys. 15 (1966) 1.
- Drell, S., Phys. Rev. 87 (1952) 753.
- Drell, S. and Walecka, J., Ann. Phys. 28 (1964) 18.
- Easlea, B., Phys. Lett. 1 (1962) 163.
- Edmonds, A., Angular Momentum in Quantum Mechanics, Princeton University Press, 1958.
- Feynman, R., Phys. Rev. 76 (1949) 749.
- Fielder, D., Le Tourneux, J., Min, K., and Whitehead, W., Phys. Rev. Lett. 15, (1965) 33.
- French, J., Halbert, C., McGrory, J., Wong, S., Advan. in Nucl. Sci., Vol. 3 (1969) 193.
- Gourdin, M., Nuovo Cim. 21 (1961) 1094.
- Goldhaber, M. and Teller, E., Phys. Rev. 74 (1948) 1046.
- Harakeh, M., Paul, P., and Gorodetzky, Ph., Phys. Rev. C, Voll. 11, No. 3 (1975) 1008.
- Hardie, G., Dangle, R., Oppliger, L., Phys. Rev., Vol. 129, No. 1 (1963) 353.
- Helm, R., Phys. Rev. 104 (1956) 1466.
- Hicks, R., et al., to be published.
- Hofstadter, R., Rev. Mod. Phys. 28 (1956) 214.
- Hofstadter, R., Edit., Nuclear and Nucleon Structure, W.A. Benjamin, Inc., N.Y., 1963.
- Hotta, A., Itoh, K., and Saito, T., Phys. Rev. Lett. 33 (1974) 790.
- Hsieh, S., Knopfle, K., Mairle, G., Wagner, J., Nucl. Phys. A243 (1975) 380.
- Johnson, W., Weber, T., and Mullin, C., Phys. Rev. 119 (1960) 1270.
- Jolly, H., Phys. Lett. 5 (1963) 289.
- Katz, L., Beer, G., McArthur, D., and Caplan, H., Can. J. Phys. 45 (1967) 3721.

- Kennedy, J. and Cliff, M., A.E.C.L. Rep. CRT-609, 1955.
- Keyser, Blue, Ramirez, and Weller, Bull. Am. Phys. Soc. 15 (1970) 1685.
- Keyser, R., Blue, R. and Weller, H., Phys. Lett. 34B (1971) 602.
- Kuo, T., and Brown, G., Nucl. Phys. 85 (1966) 40.
- Landau, L., J. Phys. U.S.S.R. 8 (1944) 201.
- Levinger, J. and Bethe, H., Phys. Rev. 78 (1950) 115.
- Lewis, F. and Walecka, J., Phys. Rev. B133 (1964) 849.
- Maximon, L. and Isabelle, D., Phys. Rev. B133 (1964) 1344.
- Meister, N. and Griffy, T., Phys. Rev. B133 (1964) 1032.
- M.I.T. 1967 Summer Study, M.I.T. Rep. TID-24667, Lab. for Nucl. Sci.,
M.I.T., Cambridge, Mass., U.S.A., 1967.
- Moller, C., Ann. Phys. (Leipzig) 14 (1932) 531.
- Moshinsky, M., Nucl. Phys. 8 (1958) 19.
- Mott, N., Proc. Roy. Soc. A124 (1929) 425.
- Nguyen Ngoc, H. and Perez y Jorba, J., Phys. Rev. B136 (1964) 1036.
- Okamoto, K., Phys. Rev. 110 (1958) 143.
- Quesne, C., Nucl. Phys. 76 (1965) 268.
- Rawitscher, G. and Fischer, C., Phys. Rev. 122 (1961) 1330.
- Rossi, B., High Energy Particles, Prentice-Hall, Englewood Cliffs, N.J.,
U.S.A., 1952.
- Rosen, M., Raphael, R., and Uberall, H., Phys. Rev. 163 (1967) 927.
- Schweber, S., An Introduction to Relativistic Quantum Field Theory,
Harper, N.Y., 1961.
- Schwinger, J., Phys. Rev. 75 (1949) 898.
- Singhal, R., Moreira, J., and Caplan, H., Phys. Rev. Lett. 24 (1970) 73.
- Steinwedel, H., Jensen, J., and Jensen, P., Phys. Rev. 79 (1950) 1019.

- Talmi, I., *Helv. Phys. Acta.* 25 (1952) 185.
- Tomusiak, E., *Am. J. Phys.* 36 (1968) 1096.
- Tsai, Y., *Proc. Int. Conf. Nucl. Struct., Stanford Univ., June 1963*, p. 221,
Stanford Univ. Press, Stanford, Calif., U.S.A., 1964.
- Uberall, H., *Phys. Rev.* B137 (1965) 502.
- Uberall, H., *Electron Scattering from Complex Nuclei* (2 Vol.), Academic Press,
N.Y., 1971.
- Verdie, Thesis, M.I.T., 1968.
- von Gehlen, R., *Phys. Rev.* 118 (1960) 1455.
- Willey, R., *Nucl. Phys.* 40 (1963) 529.
- Zuker, A., Buck, B., and McGrory, J., *Phys. Rev. Lett.* 21 (1968) 39.